

NATIONAL TECHNICAL UNIVERSITY OF ATHENS
School of Naval Architecture and Marine Engineering
Shipbuilding Technology Laboratory



DIPLOMA THESIS

Numerical Simulation of Electrochemical Behavior for Naval Steel
Microstructure Exploiting Experimental Polarization Data

Konstantinos Kouzoumis

Supervisor: Prof. Dimitris I. Pantelis

Examination committee:

Prof. N. Tsouvalis

Prof. D. I. Pantelis

Prof. D. Manolakos

Athens, October 2016

ABSTRACT

The aim of the present Diploma Thesis is the simulation of the electrochemical behavior for naval steel microstructure with the exploitation of experimental polarization data. For the model development the simulation of the microstructure was also required as an input parameter. In particular the electrochemical behavior of AH36 steel, which consists of a-phase ferrite and pearlitic micro – constituent, in NaCl 3.5% environments was simulated, concerning the polarization curves obtained by potentiostatic method. The prediction of electrochemical behavior of this alloy was simulated taking into account the electrochemical behavior of its constituting different microstructures: ferrite a-phase and pearlite micro-constituent.

For this reason, electrochemical experiments, potentiostatic polarization, was conducted on AH36 ferritic-pearlitic steel alloy, Ferrite specimen and Pearlite specimen, where ferrite and pearlite are the constituting metallographic phases of AH36. The Tafel curves obtained from the electrochemical experiments performed, show that Ferrite presents lower values for E_{corr} than Pearlite, indicating that ferrite exhibits higher tendency for corrosion. This difference implies that it would be possible for a galvanic couple to be formed at the microstructural level. More specifically, in ferrite – pearlite steel alloys exposed to corrosion, the ferrite grains could act as anodes providing electrons towards the pearlitic regions (acting as cathodes). Hence, this behavior could be simulated according to the amount of each phase within the alloy's microstructure.

For the simulation of the ferritic-pearlitic microstructure of AH36 steel, the Voronoi tessellation approach was employed. The ferrite and the pearlite amounts on the model's application regarding the microstructure deviates by 0.36% from the actual microstructure, which is considered adequately acceptable. The modeled and the experimental polarization curves for AH36 ferritic-pearlitic steel appear to be similar. The same conclusion is deduced for the E_{corr} , i_{corr} electrochemical parameters concerning the modeled and the experimental curves. The prediction regarding the metal's dissolution from the developed model, shows that the electrolyte has penetrated against the metal's domain. This denotes that the metallic regions have dissolved permitting the solution to invade. The agreement between the model's polarization curves and the experimental ones, along with the agreement in the obtained parameters E_{corr} , i_{corr} prove that the assumption of the electrochemical behavior of AH36 ferritic-pearlitic steel being defined by the electrochemical behavior of its constituting microstructures is fairly stated, as long as it is supported by a concrete simulation of the micro-structure.

ΕΙΣΑΓΩΓΗ

Ο σκοπός της παρούσας διπλωματικής εργασίας είναι η προσομοίωση της ηλεκτροχημικής συμπεριφοράς στη μικροδομή ναυπηγικού χάλυβα με αξιοποίηση πειραματικών μετρήσεων πόλωσης. Για την ανάπτυξη του μοντέλου η προσομοίωση της μικροδομής ήταν επίσης αναγκαία. Πιο συγκεκριμένα, η ηλεκτροχημική συμπεριφορά του ναυπηγικού χάλυβα AH36, ο οποίος αποτελείται από φερρίτη και περλίτη, σε υδάτινο περιβάλλον με 3,5% NaCl, μελετήθηκε με προσομοίωση, που στοχεύει στην πρόβλεψη των καμπυλών πόλωσης που θα λαμβάνονταν πειραματικά με την ποτενσιοστατική μέθοδο. Για την προσομοίωση της ηλεκτροχημικής συμπεριφοράς αυτού του κράματος χρειάστηκαν δεδομένα για τις αντίστοιχες ηλεκτροχημικές συμπεριφορές των συστατικών μερών της μικροδομής του: φερρίτης α-φάσης και περλίτης. Για το λόγο αυτό, διεξήχθησαν ηλεκτροχημικά πειράματα, με ποτενσιοστατική πόλωση, σε δοκίμιο σιδήρου α φάσης (μικροδομής φερρίτη) και σε δοκίμιο ευτηκτοειδούς σύστασης με 0.8% κατά βάρος περιεκτικότητα σε άνθρακα (μικροδομής περλίτη), καθώς και σε σε ναυπηγικό χάλυβα AH36 φερριτικοπερλιτικής μικροδομής για την εξακρίβωση της μοντελοποίησης. Οι καμπύλες Tafel που λήφθηκαν από τα ηλεκτροχημικά πειράματα που πραγματοποιήθηκαν, έδειξαν ότι ο φερρίτης παρουσιάζει χαμηλότερες τιμές για το δυναμικό διάβρωσης - E_{corr} σε σχέση με τον περλίτη, υποδεικνύοντας ότι οι φάσεις φερρίτη θα παρουσιάζουν μεγαλύτερη τάση για διάβρωση. Αυτή η διαφορά υποδηλώνει ότι θα ήταν δυνατό για ένα γαλβανικό στοιχείο να σχηματίζεται στο επίπεδο της μικροδομής ενός κράματος που συνίσταται από τις δύο προαναφερθείσες φάσεις. Πιο συγκεκριμένα, σε φερριτοπερλιτικά κράματα χάλυβα που εκτίθενται σε διάβρωση, οι κόκκοι φερρίτη θα μπορούσαν να δράσουν ως άνοδοι παρέχοντας ηλεκτρόνια προς τις περιοχές του περλίτη (που θα δρούσαν ως κάθοδοι). Για την προσομοίωση της φερριτοπερλιτικής μικροδομής του ναυπηγικού χάλυβα AH36, χρησιμοποιήθηκε η μαθηματική διακριτοποίηση Voronoi Tessellation. Τελικά η προκύπτουσα από την εφαρμογή του μοντέλου μικροδομή μετρήθηκε να αποκλίνει 0,36% από την πραγματική μικροδομή, ως προς τα ποσοστά της κάθε φάσης, και επομένως θεωρήθηκε επαρκώς αποδεκτή. Όσον αφορά την ηλεκτροχημική συμπεριφορά, συγκρίνοντας τη μοντελοποιημένη με την αντίστοιχη των πειραματικών καμπυλών πόλωσης, προέκυψαν μικρές αποκλίσεις. Το ίδιο συμπέρασμα προέκυψε για τις παραμέτρους E_{corr} και i_{corr} για τις οποίες, παρομοίως, υπολογίστηκαν κοντινές τιμές. Η πρόβλεψη της διάλυσης του μετάλλου, στο μοντέλο που αναπτύχθηκε, δείχνει ότι ο ηλεκτρολύτης διεισδύει έναντι του μετάλλου κυρίως στις περιοχές του φερρίτη, υποδηλώνοντας τη διάλυση των αντίστοιχων μεταλλικών φάσεων. Η συμφωνία μεταξύ των καμπυλών δυναμικού – ρεύματος του μοντέλου με τις αντίστοιχες πειραματικές, σε

συνδυασμό με τη συμφωνία των λαμβανομένων παραμέτρων E_{corr} και i_{corr} , απέδειξε ότι η υπόθεση της εξάρτησης της ηλεκτροχημικής συμπεριφοράς του ναυπηγικού χάλυβα AH36 φερριτοπερλιτικής μικροδομής, από την ηλεκτροχημική συμπεριφορά των συστατικών μερών του, είναι έγκυρη, εφόσον μάλιστα υποστηρίχθηκε και από επαρκώς ακριβή προσομοίωση της μικροδομής του.

ACKNOWLEDGEMENTS

The development of this thesis took place during the academic year of 2015-2016 in the Shipbuilding Technology Laboratory of the Naval Architecture and Marine Engineering School of NTUA. I would like to dedicate this work to my family, George Stamatia and Dimitris, as well as my friends Konstantina and George for their psychological and moral support throughout most of my academic career.

In addition, I would like to thank Mrs. Traka, with whom we worked in parallel, as a colleague for her altruistic cooperation and dedication, Ass. Prof. Mrs. Irene Koronaki for her guidance and Mrs. Dora Tsiourva for the idea of this thesis and her final contribution to this work. Finally, I want to show my gratitude towards Mr. Dimitris Pantelis, who supported this work and supervised it with intense interest.

CONTENTS

CHAPTER 1 – SCIENCE OF CORROSION	1
1.1: Principles of Corrosion – Application on metals.....	1
1.1.1: Nature of Corrosion	1
1.1.2: Reactions and Terminology.....	2
1.1.3: Thermodynamics of Corrosion.....	4
1.1.4: Half - cell Potential	6
1.1.5: Galvanic corrosion.....	8
1.1.6: Polarization	10
1.1.6.1: Activation Polarization	11
1.1.6.2: Concentration Polarization	11
1.1.7: Metal dissolution	12
1.2: Corrosion in marine structures	14
1.2.1: Introduction	14
1.2.2: Corrosion in Bulk Carrier’s Cargo Holds.....	16
1.2.3: Corrosion in Tanker’s Cargo Holds.....	17
1.2.4: Corrosion in Water Ballast Tanks.....	20
BIBLIOGRAPHY - CHAPTER 1	24
CHAPTER 2 – ASPECTS OF MODELLING.....	25
2.1: Introduction to scientific modelling.....	25
2.1.1: Analytical modelling.....	26
2.1.2: Numerical modelling.....	27
2.1.3: Statistical modelling.....	28
2.1.4: Modelling Applied on Corrosion Problems.....	29
2.2: Contemporary Models of Corrosion	30
2.2.1: Numerical Corrosion Modelling.....	30
2.2.1.1: Introduction	30
2.2.1.2: Density Functional Theory - Physics	30

2.2.1.3: Density Functional Theory - Application on Corrosion ^[5]	36
2.2.2: Analytical Corrosion Modelling.....	40
2.2.2.1: Introduction	40
2.2.2.2: Analytical model – Application on Fatigue Crack Corrosion ^[13]	40
2.2.3: Statistical Corrosion Modelling.....	51
2.2.3.1: Introduction	51
2.2.3.2: Statistical model – Application on ship’s corrosion ^[15]	51
BIBLIOGRAPHY - CHAPTER 2	63
CHAPTER 3 – EXPERIMENTS.....	67
3.1: Introduction	67
3.2: Experimental procedures.....	67
3.3: Experimental Results	70
3.3.1 Microstructure study of specimens	70
3.3.2 Electrochemical experiments.....	74
3.5: Results and Discussion.....	84
BIBLIOGRAPHY - CHAPTER 3	87
CHAPTER 4 – SIMULATION OF FERRITIC AND PEARLITIC GRAIN MICROSTRUCTURES	89
4.1: Introduction	89
4.2: Voronoi Tessellation	90
4.2.1: Voronoi Diagram Definition	90
4.2.2: Delaunay triangulation	91
4.2.3: Voronoi Tessellation - Delaunay triangulation dependence	92
4.3 – Microstructure Simulation – Application on G11 Steel	93
4.3.1: Model Description.....	93
4.3.2 – Model Application.....	94
4.4 – Results and Discussion for Microstructure Simulation	99
BIBLIOGRAPHY – CHAPTER 4.....	100
CHAPTER 5 – NUMERICAL MODELLING OF THE ELECTROCHEMICAL BEHAVIOUR OF AH36.....	103
5.1: Introduction	103
5.2: Model Development	105

5.2.1: Geometry	105
5.2.2: Physics analysis	111
5.2.2.1 – System’s Physics and Definitions	111
5.2.2.2 – Defining the Differential Equations.....	113
5.2.2.3 – Defining the Boundary Conditions.....	115
5.2.3: Numerical method and Mesh	118
5.3 – Modelling Procedure.....	121
5.3.1: Model Presentation	121
5.3.2: Model Application.....	123
5.3.2.1: Input values.....	123
5.3.2.2: Results.....	125
BIBLIOGRAPHY – CHAPTER 5.....	132
CHAPTER 6 – CONCLUSIONS	133
ANNEX 1	137
CODE-1	137
CODE-2	139
CODE-3	139
CODE-4	146
CODE-5	146
ANNEX 2	147
CODE-1	147
CODE-2	150
CODE-3	150

CHAPTER 1 – SCIENCE OF CORROSION

1.1: Principles of Corrosion – Application on metals

1.1.1: Nature of Corrosion

Corrosion is a phenomenon in which a material lowers its Free Energy (enthalpy). Therefore, it is a natural process, involving spontaneous chemical reactions. When a material interacts with its environment, and the total energy of this system is not at the least level possible, then corrosion occurs. At this point chemical reactions take place.

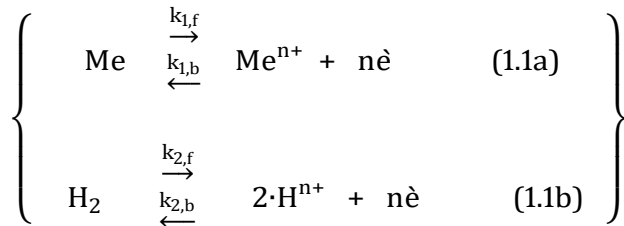
Metals in specific, corrode because they are more stable in their oxide form. Before mining, metals are found under the earth as ores. There, most of them are oxides, sulfides and silicates. This means that iron for example, that is found as an oxide, contains much more stored energy as pure iron than as iron oxide. Thus, iron will react with its environment whenever possible, in order to release all this energy and become more stable.

The amount of energy that each metal needs after its extraction from earth, in order to convert it from the oxide to the pure metal, varies for each different metallic element, and so does the stored energy it will reserve afterwards. This is the reason why some metals tend to corrode easily while others will not corrode at all.

For example, iron (Fe) is found as an oxide Fe_2O_3 and in order to convert it to iron (Fe) the amount of energy needed is 6.71 MJ/kg [5]. Therefore, iron has 6.71 MJ/kg stored energy that “wants” to get rid of through corrosion. On the other hand, platinum (Pt), is found as an oxide PtO_2 and in order to convert it to pure Platinum (Pt) the amount of energy needed is 0.44 MJ/kg [5]. So platinum has 0.44 MJ/kg stored energy that “wants” to get rid of through corrosion. If the activation energy to react is less than the stored energy, the metal will corrode. Of course platinum will probably never corrode, but iron will.

1.1.2: Reactions and Terminology

Considering a case of a corrosive environment (containing hydrogen forming into hydrogen ions), the reactions that will happen on the interface of a metal that will be exposed to that environment are the following [1], [2]:



In the above reactions $k_{1,f}$ and $k_{1,b}$ are the reaction rate coefficients for the forward (f) and the backward (b) reaction respectively, of (1.1a). The same applies for $k_{2,f}$ and $k_{2,b}$ with respect to reaction (1.1b).

The values of k of a specific reaction are obtained through the Arrhenius equation, as follows:

$$k = c \cdot e^{-E_{\alpha}/R \cdot T} \quad (1.2)$$

In the above definition k corresponds to the reaction of activation energy E_{α} and temperature T

Where:

- E_{α} : the activation energy (necessary energy) for the reaction of the respective k
- n : the number of electrons transferred
- Me : the metallic atoms that react on the surface (either in mol or mol/volume unit)
- H_2 : the hydrogen molecules that are formed or cleaved (either in mol or mol/volume unit)
- c : the pro- exponential factor (constant)
- R : is the universal gas constant so that $R = 8.3144598 \text{ J}/(\text{mol}\cdot\text{K})$
- T : is the temperature in K (-Kelvin) at which the reaction of the respective k takes place

Reactions (1.1) show the possible reactions that may appear on the metallic surface.

- Oxidation is the reaction when “ n ” electrons are given up, so $n\text{e}^-$ appears at the products.
- Reduction is the reaction when “ n ” electrons are bounded, so $n\text{e}^-$ appears at the reactants.

When the forward reaction rate equals the backwards reaction rate, in reaction (1.1a), then the metal is in equilibrium with itself. The same applies for hydrogen in reaction (1.1b). When the metallic surface is exposed to a corrosive environment (an environment that contains an amount of hydrogen), and corrosion appears, then reactions (1.1) are not in equilibrium anymore.

However, the system will have to be in equilibrium, which means that the total reaction rate of both reactions will be the same. Specifically, supposing that the metal corrodes in a way that only the forward reaction happens (oxidation), then the rate at which the metal oxidizes will have to equal the rate of the hydrogen evolution. This is chemically translated as:

$$[\text{Me}] \cdot k_{1,f} = [\text{H}^{n+}] \cdot k_{2,b} \quad (1.3)$$

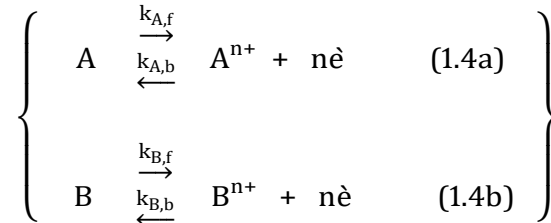
It is now shown how the metal cannot be in its ground state when a corrosive environment appears. The metal has to stop keeping the equilibrium in reaction (1.1a), and start giving up electrons in order to achieve equilibrium in the system of (1.1).

All of the above correspond to a simplified approach of corrosion phenomenon. In reality there are more reactions and more substances that control the problem, but even then, the oxidation-reduction systems will behave accordingly.

In terms of corrosion, “anodic reaction” is the reaction of oxidation, and the material giving up the electrons is called “anode”. Similarly, “cathodic reaction” is the reaction of reduction, and the material that gains the electrons is called “cathode”. The interface of the metal and the environment is called corroding surface.

1.1.3: Thermodynamics of Corrosion

Considering an electrochemical system constituted of the following reactions (similar to equations 1.1):



Where the reaction rate coefficients k in the above reactions (equations 1.4) are defined as in equation (1.2). However, here they correspond to the activation energies E_α and temperatures T of this particular case. This means that $k_{A,f}$ and $k_{B,f}$ correspond to the rates at which substances A and B form into ions A^{n+} and B^{n+} respectively. Likewise, $k_{A,b}$ and $k_{B,b}$ correspond to the rates at which ions A^{n+} and B^{n+} form to substances A and B, respectively.

Assuming the system is isolated (it does not interact with its surroundings in any way, and so mass and energy remains constant within the system), then the total energy should remain constant. The law of the conservation of energy, in this case, takes the form of the first thermodynamic law [7]:

$$\text{First Thermodynamic Law : } \Delta U = Q - W \quad (1.5)$$

The above equation (1.5) states that the internal energy of a closed system is equal to the amount of heat supplied to the system, minus the amount of work consumed by the system on its surroundings.

Assuming that the system of reactions (equations 1.4) constitute a reversible process (ideal situation), then the second thermodynamic law can also be applied: [7]

$$\text{Second Thermodynamic Law : } dQ = T \cdot dS \quad \Rightarrow \quad Q = \int_V T \cdot dS \quad (1.6)$$

The work produced in the system is constituted from the mechanical and the electrical work and so:

$$W = W_{\text{mech}} + W_{\text{el}} = \int_V p \cdot dV + W_{\text{el}} \quad (1.7)$$

Where:

- Q : heat supplied to the system
- ΔU : total internal energy change inside the system
- W : work produced by the system
- W_{mech} : the mechanical work produced by the system
- W_{el} : electrical work produced by the system
- p : the pressure in the system
- V : the system 's volume
- T: the temperature in the system

Supposing that the electrochemical system functions under constant pressure P and temperature T then, equations (1.6) and (1.7) become [2], [7]:

$$\left\{ \begin{array}{l} W = \int_V p \cdot dV + W_{\text{el}} = p \cdot \Delta V + W_{\text{el}} \\ Q = \int_V T \cdot dS = T \cdot \Delta S \end{array} \right\} \quad (1.8)$$

Substituting equation (1.8) into (1.5), the electrical work is expressed as:

$$W_{\text{el}} = -\Delta U + T \cdot \Delta S - p \cdot \Delta V \quad (1.9)$$

By definition, the change on free Gibbs energy is given by the following equation [1], [2], [7]:

$$G = U + p \cdot V - T \cdot S \quad (1.10a)$$

Then the total differential of G in (1.10a):

$$dG = dU + p \cdot dV + dp \cdot V - T \cdot dS - dT \cdot S \quad (1.10b)$$

For constant pressure P and temperature T , the integration of equation (1.10b) gives:

$$\int_V dG = \int_V dU + \int_V p \cdot dV + \int_V dp \cdot V - \int_V T \cdot dS - \int_V dT \cdot S \Rightarrow$$

$$\xrightarrow{dT=0, dp=0} \Delta G = \Delta U + p \cdot dV - T \cdot dS \quad (1.10c)$$

From equations (1.9) and (1.10c):

$$\Delta G = - W_{el} \quad (1.11)$$

Equation (1.11) denotes that the change in Gibbs free energy for the electrochemical system is given by the total electrical work produced.

1.1.4: Half - cell Potential

Electrode potential (Half - cell Potential), E , in electrochemistry, is the difference on the electrochemical potentials between two elements A and B that are in contact. This potential difference is the electromotive force causing the reactions of equations (1.4), on the interface between A and B . [1]

The electrode potential E for a system, is related to the electrical work done as follows:

$$W_{el} = n \cdot F \cdot E \quad (1.12a)$$

Where:

- n : the moles of electrons reacting
- F : Faraday constant so that $F = 96485.33289$ Coulomb/mol

Substituting equation (1.11) in (1.12a), it is obtained:

$$\Delta G = - n \cdot F \cdot E \quad (1.12b)$$

Equation (1.12b) is the electrode potential definition according to [1], [6].

Whenever corrosion appears on a metallic surface, there is a specific value of potential, in which the corroding surface is expected to find equilibrium and thus stabilize. This value depends on the metal, the environment and the conditions under which corrosion takes place. For each metal, a value of this potential, called half – cell potential, has been specified under experiments that have been conducted. Of course, the measured potentials correspond to a specific environment (electrolyte) and specific conditions (temperature and concentration of hydrogen or other oxidizers) [1].

In practice, the electrochemical half – cell potentials (equilibrium potentials) that are commonly used, are the differences measured between the potential of the metal and the potential of the standard hydrogen electrode, when the metal is being corroded by purified water with 3.5% NaCl, under 25 °C. These potentials are known as potentials versus standard hydrogen electrode (SHE).

Any other electrochemical equilibrium potential of the metal with its environment can be predicted, using an equation known as Nernst equation [1], [6]:

$$\Delta G = \Delta G^0 - R \cdot T \cdot \ln \left(\frac{\sum_{i=\text{product}}^N [M_i]^{v_i}}{\sum_{i=\text{reactant}}^N [M_i]^{v'_i}} \right) \quad \xrightarrow{(1.12b)}$$

$$\Rightarrow E_{\text{eq}} = E_{\text{eq}}^0 - \frac{R \cdot T}{n \cdot F} \cdot \ln \left(\frac{\sum_{i=\text{product}}^N [M_i]^{v_i}}{\sum_{i=\text{reactant}}^N [M_i]^{v'_i}} \right) \quad (1.13)$$

Where:

- E_{eq}^0 : The standard electrochemical half – cell potentials of the metal M_i
- ΔG^0 : The standard change of free Gibbs energy of the metal M_i
- M_i : the molecular concentration of the i substance involved in reactions
- v_i : the stoichiometric coefficient of the i substance as a product
- v'_i : the stoichiometric coefficient of the i substance as a reactant
- R : is the universal gas constant so that $R = 8.3144598 \text{ J}/(\text{mol} \cdot \text{K})$
- T : is the temperature in K (-Kelvin)
- n : the moles of electrons reacting

- F: Faraday constant so that $F = 96485.33289$ Coulomb/mol (corresponds to the charge carried by one mole of electrons)

1.1.5: Galvanic corrosion

When two metals of different electric potential are connected electrically, the metal that is less electronegative, tends to “send” electrons to the other metal. If there is a path found for these electrons to return to their initial position, then the procedure would be possible to happen. This is exactly the nature of galvanic corrosion.

The reactions that will occur on the interfaces between each metal and its environment, lead to the formation of ions, which will leave or attach to the metallic surface. This capability, allows the system to keep up the procedure of electron flow, since the electric potential of each metal will be able to remain on a certain level, without changing due to the electric current flow between the metals.

Thus, in order for galvanic corrosion to occur, there must be both a difference in the electric potentials and a certain conductivity provided from the electrolyte solution.

In reality this means that galvanic corrosion will occur when all the following appear:

- Two metals with different electric potentials, are in electrical conductivity
- These two metals have a surface exposed in a corrosive environment (electrochemical potentials occur)

When the above exist, the two metals will start reacting with the environment, both acting as anodes (both metals give electrons to the environment, and the environment acts as a cathode on both surfaces). Simultaneously, the metal with the highest electric potential will send electrons to the other one, through the electric conductor. Here, the metal which gives the electrons is called anode and the metal receiving them is called cathode (the metal that takes the electrons is called cathode in this case, since the cathodic reaction of the environment will prevail over the metal’s anodic) [2]. The cathode takes the electrons, but of course will not keep them, so it sends them to the surface exposed to the corrosive environment. This means that the cathode will “save” some electrons and will not form the same number of ions and will not undergo the same mass change, which would if it wasn’t in contact with the anode.

Essentially, galvanic corrosion is about an electrical circuit (see figure 1.1), formed by the two metals in electrical contact and the electrolyte (-corrosive environment) who has the role of the electrochemical conductor through whom the electrons can travel back to the anode (as anions of the electrolyte that were formed on the cathode – electrolyte surface) [1], [2].

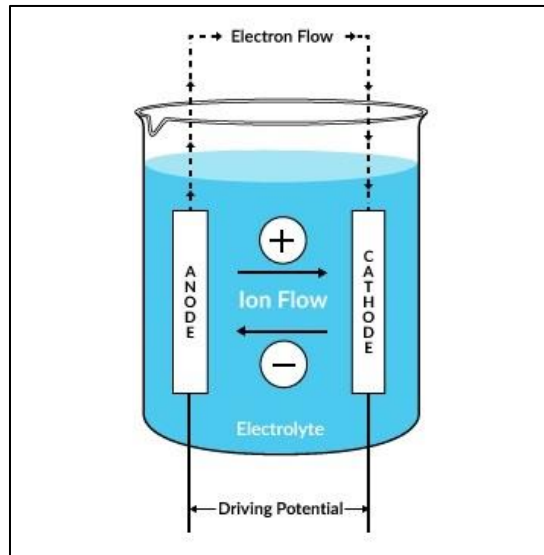


Figure 1.1: The equivalent electrical circuit of galvanic corrosion. [8]

Considering the reactions explained in paragraph 1.1.2, it is not possible in the case of a galvanic couple, for the corroding surfaces to be in their equilibrium state. The anodic reaction of the metal with the more negative potential will prevail compared to the cathodic of the environment, whilst for the other metal the cathodic reaction of the environment will prevail compared to the anodic. The equilibrium of the system in this case, requires that the total reaction rates of both corroding surfaces are equal. Thus the system will be in its equilibrium state, but each metal will not. Each metal will exhibit a voltage difference from the equilibrium half - cell potential.

1.1.6: Polarization

In practice the real potential of a metal corroding, can have a different value of the expected equilibrium potential. This indicates that the reaction rate of the anodic reaction occurring on an electrode surface differs from the cathodic one. This situation is called polarization. There, the electrochemical potential of the metal can either be more negative (cathodic polarization) or less negative (anodic polarization) than the corrosion-equilibrium potential measured (or calculated through equation (1.13) - Nernst equation) for the metal in the specific environment – electrolyte. This potential difference is called “polarization” or “overpotential” and it is defined as follows [1]:

$$\left\{ \begin{array}{ll} \eta_{\alpha} = E - E_{\text{eq}} & (1.14a) \quad \text{for the anodic polarization} \\ \eta_{\text{c}} = E_{\text{eq}} - E & (1.14b) \quad \text{for the cathodic polarization} \end{array} \right\}$$

Where:

- E : the real potential (-voltage) on the metallic surface
- E_{eq} : the equilibrium potential (-voltage) on the metallic surface

Studying a system of reactions similar to equations (1.1), the reaction rates (RR) for the anodic and the cathodic reactions are expressed as follows [2]:

$$\left\{ \begin{array}{l} \text{RR}_{\text{anodic}} = [\text{Me}] \cdot k_{1,\text{f}} \\ \text{RR}_{\text{cathodic}} = [\text{H}^{\text{n}+}] \cdot k_{2,\text{b}} \end{array} \right\} \xrightarrow{(1.2)} \left\{ \begin{array}{ll} \text{RR}_{\text{anodic}} = [\text{Me}] \cdot c_1 \cdot e^{-E_{\alpha,\text{anodic}}/R \cdot T} & (1.15a) \\ \text{RR}_{\text{cathodic}} = [\text{H}^{\text{n}+}] \cdot c_2 \cdot e^{-E_{\alpha,\text{cathodic}}/R \cdot T} & (1.15b) \end{array} \right\}$$

When the reaction rates of equations (1.15a) and (1.15b) have different values, then polarization occurs.

1.1.6.1: Activation Polarization

From equations (1.15a) and (1.15b) it is clear how a reaction's rate depends on its activation energy. Hence, by altering either the metal's oxidation activation energy $E_{\alpha,\text{anodic}}$ or the hydrogen's reduction activation energy $E_{\alpha,\text{cathodic}}$ by some source, then the reaction is said to be under "activation polarization".

In this case the polarization is called "activation polarization" or "overpotential". The overpotential relates to the current densities (functions of reaction rate), and are calculated through the following equations known as Tafel equations [1], [6]:

$$\left\{ \begin{array}{ll} \eta_{\alpha} = \beta_{\alpha} \cdot \log\left(\frac{i_{O,M}}{i_{\text{corr}}}\right) & (1.16a) \quad \text{for the anodic overpotential} \\ \eta_c = -\beta_c \cdot \log\left(\frac{i_{R,Z}}{i_{\text{corr}}}\right) & (1.16b) \quad \text{for the cathodic overpotential} \end{array} \right\}$$

Where:

- β_{α} : the tafel slope for anodic overpotential
- β_c : the tafel slope for cathodic overpotential
- $i_{O,M}$: total oxidation current (from all oxidizing reactions taking place on the metallic surface)
- $i_{R,Z}$: total reduction current (from all reducing reactions taking place on the metallic surface)
- i_{corr} : total current when $E = E_{\text{eq}}$ on the metallic surface

When potential is imposed on a metallic specimen from an external voltage source, such as a potentiostat, a current will pass according to the following equation [4]:

$$i_{\text{MEASURED}} = i_{O,M} - i_{R,Z} \quad (1.17)$$

1.1.6.2: Concentration Polarization

From equations (1.15a) and (1.15b) it is clear how the rates of each reaction depend on the concentrations of its respective reactants. Thus, when the metallic atoms increase in concentration near

the corroding surface, the anodic reaction rate RR_{anodic} will increase accordingly. This is reasonable since it indicates that more material is provided for oxidation. Likewise, when the hydrogen cations increase in concentration near the corroding surface, the cathodic reaction rate RR_{cathodic} will increase as well, implying that more hydrogens cations will be available for hydrogen molecule formation. These changes in concentration result to difference between the two reaction rates, causing polarization. This concentration dependent polarization is known as concentration polarization.

In practice, a metallic atom's concentration alters only in very high corrosion rates, and thus anodic concentration polarization appears in most cases intentionally. However, changes on the hydrogen cations' concentration is a usual phenomenon, where hydrogen cations depletion appears near the electrode surface.

In any case, for the calculation of the concentration polarization, Nernst equation (1.13) is applied as follows:

$$E = E_{\text{eq}}^0 - \frac{R \cdot T}{n \cdot F} \cdot \ln \left(\frac{\sum_{i=\text{product}}^N [M_i]^{v_i}}{\sum_{i=\text{reactant}}^N [M_i]^{v_i}} \right) \xrightarrow{1.14b} \eta_c = \frac{R \cdot T}{n \cdot F} \cdot \ln \left(\frac{[H^+]^2}{[H_2]^1} \right) \quad (1.18)$$

1.1.7: Metal dissolution

When a metal undergoes corrosion, either as one metallic surface or as a part of a galvanic couple, electron flow will occur. Every electron that leaves or is absorbed by a surface implies that there has been ion formation. In case of metals, when atoms become ions, the electronic energy of the metallic structure changes. This of course means that the potential of the metal will change as well. In order for the metal to remain in its lowest energy level, these ions must leave the metallic structure. This is why a metal dissolves during corrosion. As it is shown in reaction (1.1) of chapter 1.1.2 a metal's oxidation, results to the release of n electrons and the formation of cations Me^{n+} . A metal's dissolution is therefore depending on the number of electrons participating. For every n electrons, a molecule leaves the metallic structure. The electric charge that leaves the metal can be calculated [2]:

$$\left\{ \begin{array}{l} Q = F \cdot dN \cdot n \quad (1.19a) \\ I = \frac{dQ}{dt} \Rightarrow Q = \int_0^t I \cdot dt \quad (1.19b) \end{array} \right\}$$

Where:

- F : Faraday constant so that $F = 96485.33289$ Coulomb/mol
- dN : the number of moles of the metal that reacted, and so it equals the dissolution in moles
- n : the number of electrons per molecule of the reacting species
- I : the total current in Amperes, that is produced because dN molecules reacted

Because (1.19a)=(1.19b) :

$$F \cdot dN \cdot n = \int_0^t I \cdot dt \Rightarrow dN = \frac{\int_0^t I \cdot dt}{F \cdot n} \quad (1.20)$$

Equation (1.20) calculates the metal's dissolution in moles for a period of time t. But [2]:

$$\text{mol} = \frac{\text{mass unit}}{\text{molar weight [mass/mol]}} \Rightarrow dm = dN \cdot MW \text{ [mass/mol]} \xrightarrow{(1.20)}$$

$$\Rightarrow dm = \frac{\int_0^t I \cdot dt}{F \cdot n} \cdot MW \quad (1.21)$$

Equation (1.21) calculates the metal dissolution in mass units, where:

- MW : the material's molar weight

1.2: Corrosion in marine structures

1.2.1: Introduction

One of the most basic needs in today's world is transportation, both for personal and commercial reasons. Considering the globalization of the modern economy things need to be transferred from city to city, country to country or even from continents to continents. Most of the global transportations is done via ships, due to the unit per transportation price ratio which is essentially lower than other means (e.g. planes).

As every complex structure, so do ships have problems in being built and conserved so they can travel safely and have an appropriate lifespan. Both are important factors, safety always comes first and regulations demand the meeting of certain standards. In addition to that, a decent lifespan makes the ship a more profitable investment since the costs for that, during building and maintenance, are less than building a new ship in a short period of time.

In pursuit of this goal, all affecting parameters which can cause any kind of corruption on the structure must be extensively studied and properly restricted. Corrosion is a parameter of major importance, since it does not only lead to destructive results, but also protection against it is significantly difficult. The difficulty lies in the continuity of its appearance on the marine structures, the numerous parts of the ship that are affected from it and the hardships of defining the grade of all affecting parameters. All of the above make the need to have a life expectancy of 20-25 years even harder to satisfy.

The rate of corrosion is controlled by the rate of the relevant chemical reactions (e.g. the reactions 1.11 and 1.12). Therefore, every parameter affecting the rate of any of the constituting reactions, will either delay or accelerate the process.

Considering the above, corrosion is controlled by the diffusion of reactants to and from the metallic surface. The bare metal surfaces corrode at a faster rate than those coated or covered with a compact layer of corrosion products (rust). Corrosion is also determined by the diffusion of oxygen through the water to the metallic surface, since the amount of available oxygen molecules in the environment, accelerates the process. For example, regions where corrosive fluids have high flow velocity, such as those located near bell mouths, corrode at higher rates, because there the oxygen is constantly resupplied and so its concentration remains high. Areas covered by a thin layer of moisture, such as

empty ballast tanks or the empty space at the top of the tanks (where air could be trapped), have much higher corrosion rates than areas that are submerged in water, where the oxygen content is low.

Additionally, temperature, is an important factor in corrosion. As temperature increases, higher corrosion rates are observed. This is because temperature not only affects the diffusion coefficients but also affects the reaction rates and the electrochemical potentials of corroding surfaces (see equation 1.4 – Nerst).

Finally, corrosion rates increase as the conductivity of the corrosive environment increases, due to the faster transportation of ions in the solution. The conductivity in a solution (ionic conductivity) is determined from the number of ions it contains. The rate of corrosion is very high for solutions with high concentrations of ions, such as seawater. Common seawater contains sodium chloride (NaCl), which becomes sodium ions (Na⁺) and chloride ions (Cl⁻), both of which conduct electricity. The chlorides contained in seawater are very destructive (corrosive) in the same way sulfur ions contained in tanker loads are. [1]

The main reasons why ships undergo corrosion are:

- The marine environment combines the effects of saline seawater, salt laden air, localized high temperatures, atmosphere and weather conditions (rain, condensation). Thus, it is considered as the most corrosive environment.
- Ships are made out of steel, or aluminum alloys in some cases, both of which will have the tendency to corrode, a tendency which is magnified considering all the additional factors that may increase the corrosion potential (e.g. residual stresses, fatigue, cracks).

In addition to this highly corrosive environment, the structural complexity makes handling the problem more difficult and many sections need their own approach due to the uniqueness of the phenomena they are facing. Ship structures have been studied extensively over the years around the corrosion problems they deal with. Engineers have given solutions on how every single area of a ship can be protected. Of course, not every area undergoes corrosion in the same way. Areas on a ship suffering from corrosion are:

- Outer hull
- Ballast Tanks

- Cargo Tanks (Both Oil Tanks and Holds – Grain Tanks)
- Fresh Water Tanks
- Bilges
- Pipeline system
- Propeller
- Shaft
- Boilers and Engines
- Valves
- Fuel Oil and Diesel Oil Tanks
- Flanges
- Bearings
- Pumps

Out of the pre-mentioned areas, higher corrosion damage is found in bulk carrier holds, tanker holds and water ballast tanks.

1.2.2: Corrosion in Bulk Carrier's Cargo Holds

Bulk carrier cargo holds are a high risk zone, since it is the area of a ship that can be found empty, full or partially filled with either cargoes of different properties or even ballast. There humidity and human interaction, loading and unloading cargo, can be considered as constant factors which affect the conditions of the corrosion phenomena. Cargoes that can further cause corrosion are those which are ionically conducting, possess a large surface area with a significantly high moisture content or associated water and act as cathodes. Following are examples of such cargo: [5]

- Sulphur in bulk
- Copper concentrate (contains sulphur),
- Coal (contains sulphur),
- Petroleum Coke and Iron Ore
- Bauxite

Their cathodic behavior demands existing exposed steel under them so that they can form a galvanic couple, having the anodic reaction (Equation (1.11)) occurring on the steel surface and the cathodic

(Equation (1.12)) on the cargo. Even though the cathodic reaction tends to be slow due to the lack of oxygen, the very large surface of the cargo removes this limitation causing no control over the dissolution of the steel plate. The formation of the mass loss of the steel is in pits (see Figure 1.2), due to part of the structure surface being tangent to the cargo and the rest being exposed to the environment. The cargo-steel surface is protected from corrosion and the exposed part is corroding with high rates, leading to pitting corrosion. The chemical reactions that govern this phenomenon are the following [1], [2]:

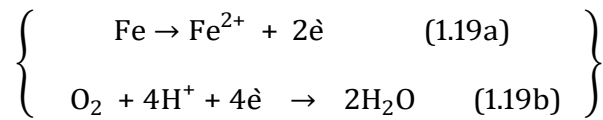


Figure 1.2: Pitting Corrosion on the sides of a Bulk Carrier's Cargo Hold [5]

1.2.3: Corrosion in Tanker's Cargo Holds

The phenomenon of corrosion in tankers, systematically concerns the international scientific community as it is the first cause of maritime accidents. Wears observed on tankers due to corrosion are very common and their occurrence increases with the age of a ship. [1]

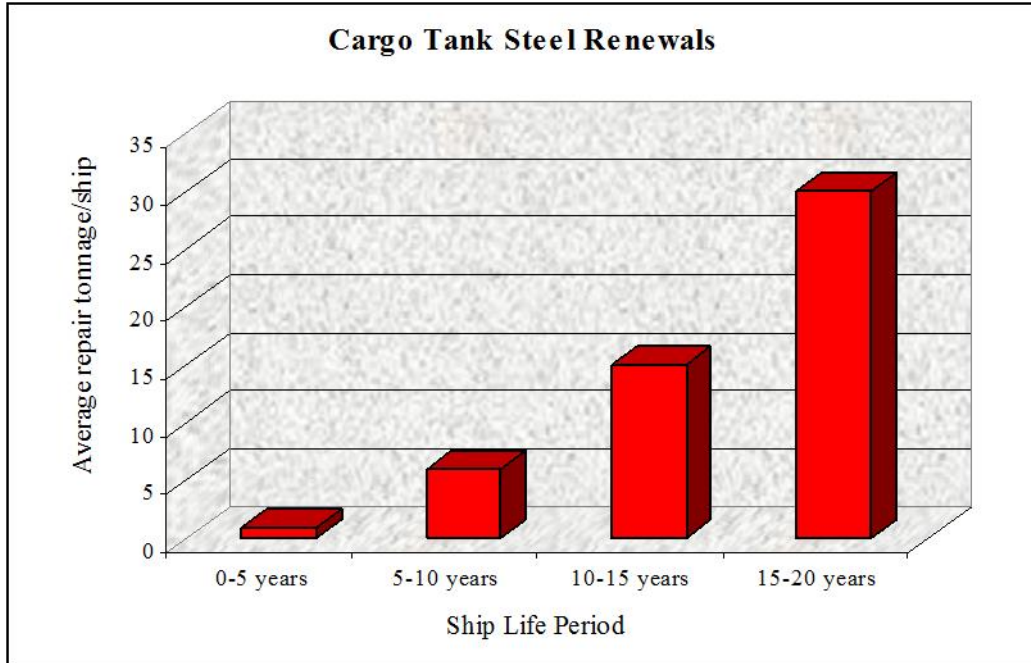


Figure 1.3: Steel quantity (in tons) replaced on tankers due to corroded cargo tanks (fully unprotected) as function of time [1]
 Generally, corrosion in cargo tanks of such ships, is related to the cargo and its loading condition.

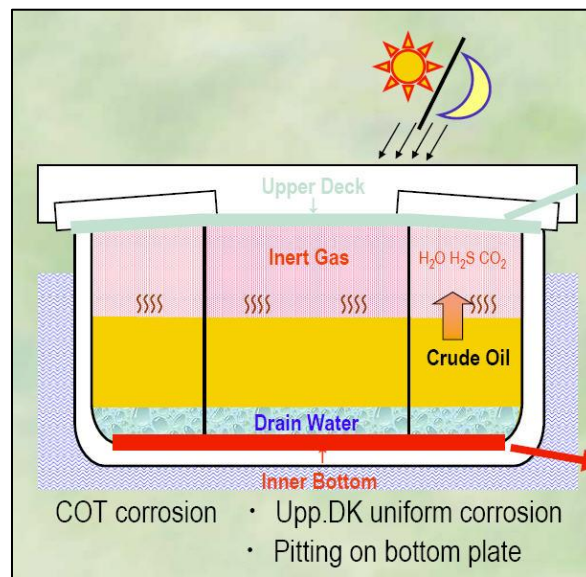


Figure 2.4: Partially filled tank with crude oil and inert gas filling the empty space [1]

When the tank is partially full, cargo is loaded up to a certain percentage and the above empty space of the tank is loaded with inert gas (see figure 1.4 above) so that any potential case of explosion is avoided. Crude oil releases volatile organic components, which are mixed with the inert gas. Out of these

components the more active is the hydrogen sulphide gas, which quickly reacts with traces of oxygen and water vapor to form sulfuric acid at various concentrations. These liquids are very acidic, resulting to the attack of the steel surface and the formation of iron sulfate. The same components are produced when bacteria, which exist in the environment of a tank, oxidize hydrogen sulfide forming sulfuric acid. [6]

When the tank is empty (of cargo) it is filled with inert gas. The inert gas, however, entering the tank contains large amounts of water vapor, which then condense on the surface of the steel. For example, the inert gas enters the tank at about 45°C and during the night the temperature decreases at 20°C. The cooling of such large amounts results in the condensation of significant amounts of water on the plates under the deck and the adjacent parts of the construction. During the day the heat combined with the water stored at the regions below the deck, favors the dissolution of various substances such as carbon dioxide and nitrogen oxides contained in the inert gas. This creates carbonates and nitrates solutions that affect the area below the deck [6].

As the above mechanisms imply, intense corrosion occurs at the upper internal plates of the cargo tanks. This form of corrosion which occurs in these regions is usually uniform, but when localized forms appear, they can lead to perforation of the plates [1].

Corrosion rate is always increased when the cargo remains on high temperatures. However, in the case of double hull tankers corrosion is enhanced not only when referring to heated cargo transport. There, even when the cargo is not heated during the transportation, the cooling procedure that would otherwise take place due to the lower temperature of the sea is limited. The empty space on the side walls prevents the transmission of heat between the load and the sea so the plates are kept at higher temperatures for longer times, in comparison to the plates of single skin tankers (see figure 1.5 below). Since the phenomenon of corrosion highly depends on temperature, the elevated temperature accelerates the rate of corrosion. [1]

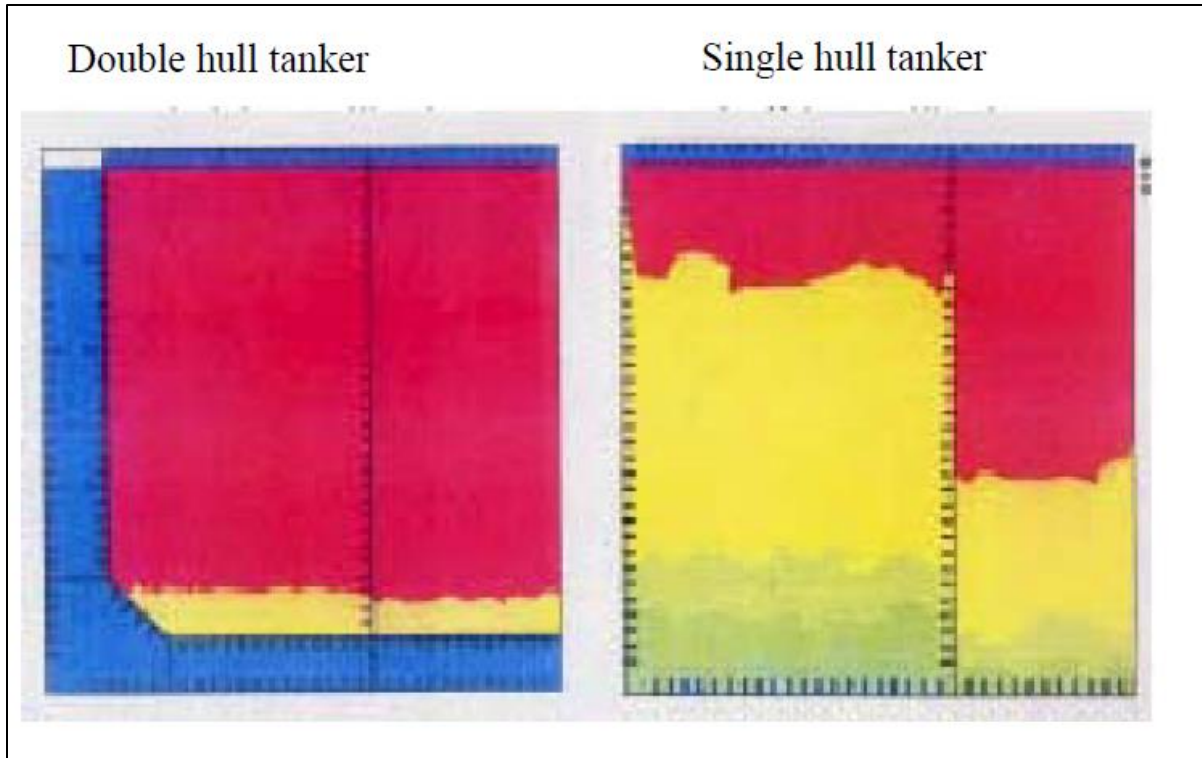


Figure 1.5: The temperature distribution for the cargo in double and single hull tankers respectively
Red colored regions indicate higher temperatures and yellow lower [1]

1.2.4: Corrosion in Water Ballast Tanks

Ballast tanks in general, are one of the most vulnerable places to corrosion, since both the states they are found in, filled with ballast or empty, cause extreme corrosion. In the first case, where the tank is filled or partially filled with ballast, the seawater acts as the corrosive environment. However, even when the tank is empty, high percentage of humidity remains inside leading to corrosion. The main protection used is coatings, which in some cases are combined with sacrificial anodes. The severity of the consequences, leading to steel replacement, when leaving ballast tanks steel unprotected is shown in the following figure 1.6.

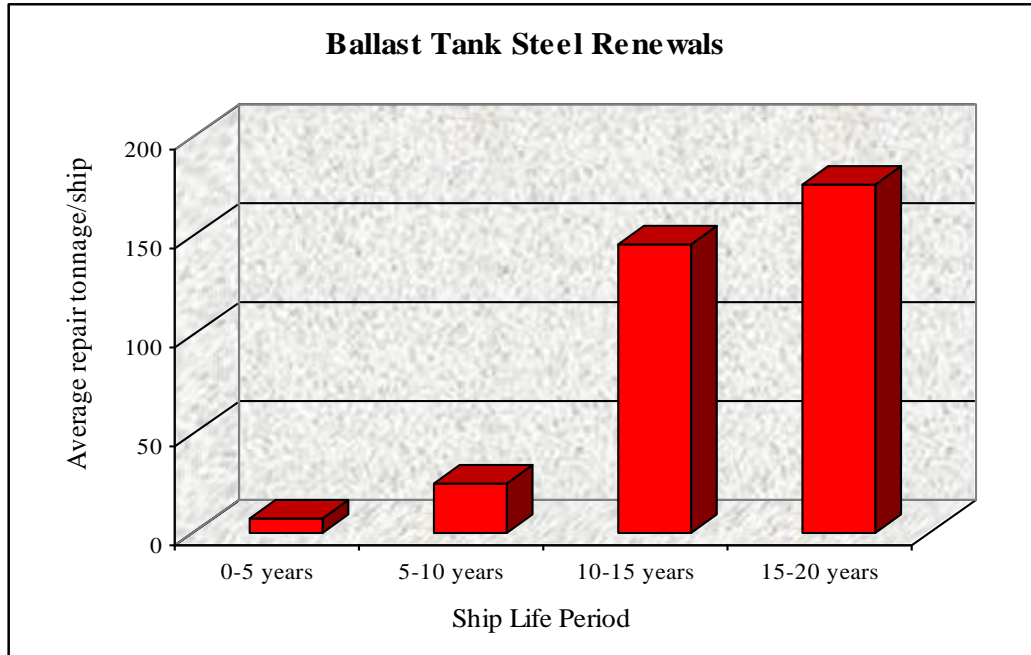


Figure 1.6: Steel quantity (in tons) replaced on tankers due to corroded ballast tanks (fully unprotected) as function of time [1]

Ballast tanks, as already mentioned, are protected with coatings. Thus, the problem regards to the coatings abrasion, which indicates the beginning of corrosion. However, no traces of pitting corrosion are commonly found. [1]

Corrosion is mostly found in longitudinal stiffeners at the ends of the web (-reinforced) frames (see figures 1.7, 1.8). The significant deterioration of the coatings is observed in upper side ballast tanks. This great wear on the coating makes steel in these regions more susceptible to corrosion than the steel in double bottom tanks.



Figure 1.7: Corrosion of longitudinal stiffeners in ballast tanks (fully unprotected) [1]



Figure 1.8: Corrosion of longitudinal stiffeners in ballast tanks (fully unprotected) found near the transverse web region [1]

The higher risk found on upper side ballast tanks is due to the temperature there, which is significantly higher than the one in the double bottom tanks. The seawater lowers the temperature of the double bottom tanks while on the upper side ballast tanks it increases due to the convection of heat through the deck, which is heated by solar radiation (see figure 1.9). [1]

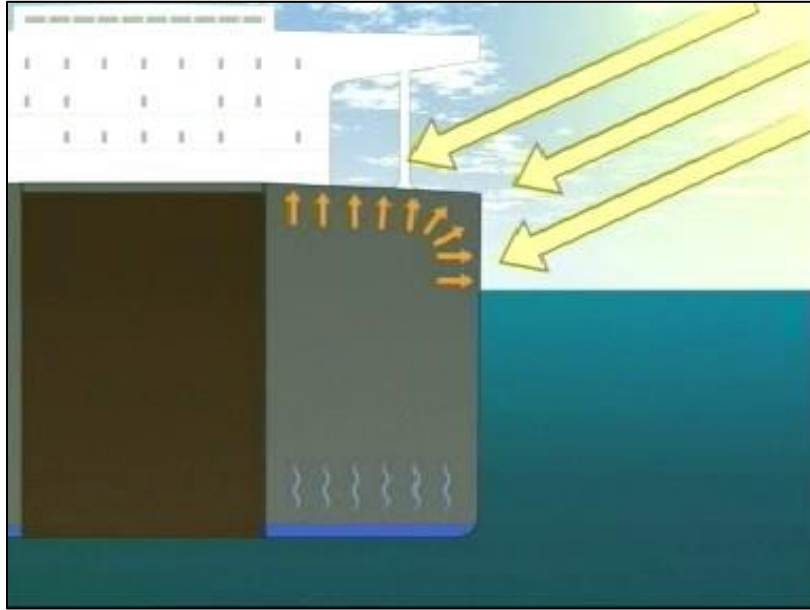


Figure 1.9: Heating of the top side ballast tanks due to solar radiation [1]

Anyhow, the corrosion rate of a tank depends on the protective measures taken. If coatings are applied as the sole protective measure, then any scraped regions imply that the exposed steel will corrode. This applies both when the tanks are full and when empty. In the case of additional sacrificial anodes, the steel would remain protected even without the coating. However, this method can only provide protection in the case of ballast loaded tanks, since seawater acts as an ionic conductor. When the tank is empty, no current will be supplied from the anodes and so the corrosion will start if any coating abrasion takes place. [1]

BIBLIOGRAPHY - CHAPTER 1

- [1] Παντελής Δ.Ι., Τσιούρβα Θ., “Διάβρωση Και Προστασία Ναυπηγικών Κατασκευών” , Πανεπιστημιακές Εκδόσεις ΕΜΠ, Αθήνα 2012.
- [2] Traka K., “Numerical simulation of electrochemical behavior for naval steel microstructure via Tafel curves extrapolation method”, Diploma Thesis for the degree of Naval Architecture and Marine Engineering, National Technical University of Athens, 2016.
- [3] “Basics of Corrosion Measurements”, Application Note Corr 1, EG&G Princeton applied research, Princeton University, NJ 1985.
(http://www.ameteki.com//media/ameteki/download_links/documentations/library/princetonappliedresearch/application_note_corr-1.pdf?la=en)
- [4] Pierre R. Roberge, “Handbook of Corrosion Engineering”, McGraw-Hill Publication, 2000.
- [5] Dr Jane Lomas & Dr Les Callow, “Premature Failure of Cargo Hold Coatings by “Active” Cargoes”, Notes, Amtech Consultants, Frodsham, Cheshire, 2015.
<http://www.amteccorrosion.co.uk/motorshipch.html>)
- [6] Denny A. Jones, “Principles and Prevention of Corrosion (2nd Edition)”, Prentice Hall Publishing, University of Nevada, Reno, Nevada 1995.
- [7] Κορωνάκη Ε., Θερμοδυναμική, Παραδόσεις Μαθήματος, ΕΜΠ Αθήνα 2013.
- [8] APP Blog Notes, “Corrosion Part 2: The Nitty Gritty”, 2015. (<http://blog.appinc.co/corrosion-part-2-the-nitty-gritty>).

CHAPTER 2 – ASPECTS OF MODELLING

2.1: Introduction to scientific modelling

In science, a model is a representation of an object or even a process or a system that is used to describe and explain phenomena that cannot be experienced directly. It describes one or more aspects of the structure, the properties or the behavior of the system studied. A model is a collection of entities, with clearly predefined properties which can be correlated by well-defined rules or relationships. The purpose of the model is to simulate accurately the substantive aspects of a particular area of reality [3].

Generally, the term modelling includes any method which attempts to describe a process, through the definition of some of its constituting parameters. The components and the purposes of the study are determined by the 'designer' of the model. For each modelling, the presence of experimental data that serve, either as reference for the evaluation of the model or as input data for the model's application, is essential [3].

Modelling is applied in physical problems for the estimation of certain variables. Modelling is needed to find solutions in a system's consisting variables, whenever classical science's theorems and formulas are not applicable. This is usually found in physical systems that include complex phenomena and consisting variables do not fulfill the conditions that the application of these formulas requires. Such conditions are usually for ideal situations that differ from a practical application's problem. Therefore, the real physical system will not comply with the necessary requirements, and a different analysis, such as modelling, should be applied.

Scientific modelling is mostly accomplished in the following three ways:

- Analytically
- Numerically
- Statistically

In the following paragraphs, each of these modelling approaches is explained.

2.1.1: Analytical modelling

Analytical models are mathematical models where the equations used to describe changes in a system have a closed form solution, expressed as a mathematical analytic function. More specifically, analytical modelling regards to the description of a system or a process using well-defined mathematical expressions. The analytical modelling of physical problems, uses fundamental equations, develops them and decreases the degrees of freedom (whenever needed) involved through stated assumptions. Eventually, the analytical model results in the production of approximate relations, which aim to cover as many cases as possible and to give the least deviations possible from experimental results.

It is applied in systems where predefined fundamental equations cannot stand alone and describe properly the ongoing procedure. Such physical problems, may be mathematically described (e.g. using a partial differential equation), but a well-defined solution cannot be induced (e.g. the degrees of freedom is larger than the number of independent equations). In order for the model to provide solutions, it subdivides the phenomena involved in the system and studies their physical quantities with appropriate equations. At this point each separately studied phenomenon's variable acts as a parameter for the others, whilst its value will have to be appropriately altering – modelled. Therefore, the production of any mathematical expression capable of predicting a system's behavior contains simplifications and assumptions of other parameters. After an assessment or simplification is made in a stage of the model's development, it is obligatory to estimate the divergence from reality. In this case, reality refers to the outcome of any appropriate experiment that already has or not been conducted. [3]

The final expression that describes the modelled system has to be a mathematical function of certain parameters. It can be therefore used to any physical problem that complies with the model's development. In specific, the fundamental equation and every assumption made during this stage need to be the same for every application.

An example of a problem that analytical modelling can be used on, is a system described with the differential equation of heat transport as the fundamental equation. There, the mathematical expression produced will calculate the total thermal energy as a function of time and space. Of course, for this to happen the final expression should only contain one dependent variable, here the total thermal energy.

For instance, the heat convection coefficient, which normally depends on the temperatures, will have to be assumed stable during temperature variations or in some way be expressed differently.

Similarly, all other consisting variables of the original equation will be degenerated into parameters, which can differ in value for each application.

2.1.2: Numerical modelling

Numerical modelling uses numerical methods and gives a quantitative representation of the studied variables over the course of time. It is used for systems whom equations do not have analytical solutions, and so numerical methods should be applied. In this case the modelling procedure attempts to simulate reality through the numerical results obtained. The aim is to represent a procedure with the use of well-defined equations and multiple calculations so that the process studied can be characterized and predicted with small deviation from reality.

These equations are solved for various points in space. The division of space into smaller parts is done through finite elements which are defined as three dimensional entities with certain geometrical and spatial attributes. In specific, the solution of the equations takes place at each node of the finite element and the model's solution derives from their interpolation. The results a numerical model produces, are distributions and graphs. However, any graph of the solution may contain curves (-functions), but they will not be expressed mathematical. This is because these curves are not obtained as schematic illustrations of an analytical expression. Instead, they have been calculated as values that the dependent variable receives according to certain values of its arguments.

The main difficulty in such a task is the initial definition of the physical equations governing the phenomena occurring in the simulation, and the interaction between them. In addition, the modelling procedure should be not only, possible, but also time and cost effective in order to be considered as a useful application. This is a function of several parameters such as the type of the program used for the simulation, the number of equations for which calculations are executed, the number of finite elements etc. [3]

An example of a problem that numerical modelling can be used on, is a system described with the differential equation of momentum transport (e.g. Navier Stokes) as the fundamental equation. Such an equation cannot induce a catholic solution, thus, it is approximated numerically instead. A variety of numerical analysis tools can be applied for the production of an accurate estimation of the dependent variable, such as the finite difference method.

2.1.3: Statistical modelling

Statistical – probabilistic modelling is a methodology where statistical analysis is applied on a wide range of data, in order to provide a mathematical expression which can adequately predict a certain variable. These data are actually values measured for the variable that the model is aiming to predict with the expression. It is used when the phenomena which are to be described are complex, but are found to have correlation between them.

Statistical – probabilistic modelling is applied in systems where it is difficult or impossible to describe the ongoing procedures. This can be found on systems where the occurring phenomena are uncertain or the physics that applies to them is not well defined. There, a statistical approach can be applied since it does not require acknowledge of the fundamental equations that comply with the system.

It can be noted that such modelling differs from the aforementioned analytical and numerical modelling. Here the outcome expressions do not have a physical meaning, but are only a best fit for statistical distributions that the studied physical quantity supposedly follows. The advantage that such methodologies provide is that through statistical analysis, the validity is mostly dependent on the sample space and estimated prior to the creation of the expression itself (standard deviations, mean values etc.)

2.1.4: Modelling Applied on Corrosion Problems

The corrosion fundamental theory itself cannot describe real life situations but rather ideal that only contain the physics of electrochemistry. As explained in previous chapters, corrosion processes are complex and occur in combination with many other phenomena. This means that a scientific field cannot effectively, or at all, predict the outcome of such physical system by itself. A corroding metal will undergo so many changes that even its properties will be affected. This means that the description of the ongoing procedures, does not only require Electrochemistry, because changes of properties related to Strain – Stress analysis, Fluid Mechanics, Thermodynamics and Transport Phenomena should be taken into account. For example, during corrosion, apart from current and potential changes, there may also occur deformation and fractures alterations, temperature variations, products and reactants diffusion. All the above, imply that corrosion deductions affect the system's parameters and therefore the validity of electrochemical approaches decreases. Thus, the modelling of such phenomena can be characterized as mandatory for accurate predictions of their development. In the following chapters models that have been applied on corrosion systems will be presented, explained and discussed.

Corrosion modelling is commonly used for the prediction of both experimental systems and practical applications. Many different models have been developed even for the same type of corrosion. The numerous phenomena that corrosion systems encounter (deformation, electrostatics etc.) is the reason why they can be studied and described by many different aspects and scientific fields. Moreover, corrosion problems are found to be studied analytically, numerically and statistically. In the following sections, three models are explained, each corresponding to a different type of modelling.

2.2: Contemporary Models of Corrosion

2.2.1: Numerical Corrosion Modelling

2.2.1.1: Introduction

During corrosion, a metallic surface undergoes changes that may or not be macroscopically visual. However, all changes will happen on its atoms and crystals, whose behavior will determine how the grains (and whole surface at the end) will respond. This is the reason why a metal's corrosion could be modelled on the level of atoms.

Nano – scale modelling in general, refers to the simulation of a material's behavior on the level of atoms or molecules. In order to accomplish this task, even smaller particles will have to be studied (electrons, protons, etc.). Hence, in this level of modelling, only quantum mechanics can explain and predict the system's state. However, quantum mechanics equations, and specifically Schrodinger equation, cannot be solved analytically, with a general solution. This means that any calculations on an atomic level, will have to involve simplifications and admissions and in many cases numerical solutions.

In the past few years, certain methodologies have been developed and proposed, capable of approximating the true solutions of a variety of problems studied on the system's atomic level. One of the most famous and widely used is the density functional theory. This method can be applied in any system of atoms or molecules, aiming to predict how the system will respond under external changes.

2.2.1.2: Density Functional Theory - Physics

Given any system of atoms (or ions), the state at which it will find its equilibrium, will be the one containing the lowest energy. This of course is the ground state of the given system. From quantum mechanics, it is explained how this state can be defined by Schrödinger equation [9]:

$$\hat{H} \cdot \Psi(\{\vec{r}_m\},\{\vec{r}_n\}) = E \cdot \Psi(\{\vec{r}_m\},\{\vec{r}_n\}) \quad (2.1)$$

Where:

- \hat{H} : The Hamiltonian (total energy operator) so that:

$$\left\{ \begin{array}{l} \hat{H} = \hat{T} + \hat{V}_{\text{coulomb}} \\ \hat{T} : \text{kinetic energy operator} \\ \hat{V}_{\text{coulomb}} : \text{electric energy operator} \end{array} \right\}$$

- E : The total energy in the system
- $\Psi(\{\vec{r}_m\},\{\vec{r}_n\})$: The system 's wave function so that:

$$\left\{ \begin{array}{l} \vec{r}_m = (x,y,z,\sigma) : \text{exact coordinates (and } \sigma=\text{spin) for the m electron} \\ \vec{r}_n = (x,y,z) : \text{exact coordinates for the n nuclei} \\ \{\vec{r}_m\} = \vec{r}_1, \vec{r}_2, \dots, \vec{r}_{N_e} \quad \text{with } N_e \text{ the number of electrons} \\ \{\vec{r}_n\} = \vec{r}_1, \vec{r}_2, \dots, \vec{r}_{N_n} \quad \text{with } N_n \text{ the number of nuclei} \\ \Psi(\{\vec{r}_m\},\{\vec{r}_n\}) \cdot \Psi^*(\{\vec{r}_m\},\{\vec{r}_n\}) : \text{the probability density for all } \vec{r}_m, \vec{r}_n \text{ being true} \end{array} \right\}$$

Börn - Öppenheimer approximation [17]

At this point the first approximation is made, related to the fact that nuclei particles are much more heavy and slow in comparison to electrons. As a result, the motion of electrons is separated from the motion of nuclei, leading to the assumption that the total wave function can be decoupled into the product of the wave function of electrons only, and the wave function of nuclei only. The above is expressed as following:

$$\left\{ \begin{array}{l} m_{\text{nuclei}} \gg m_e \\ \vec{u}_e \gg \vec{u}_{\text{nuclei}} \end{array} \right\} \Rightarrow \Psi(\{\vec{r}_m\}, \{\vec{r}_n\}) = \Psi_e(\{\vec{r}_m\}, \{\vec{a}_n\}) \cdot \Psi_{\text{nuclei}}(\{\vec{a}_n\}) \quad (2.2)$$

Where:

- \vec{a}_n : exact coordinates for the n nuclei (expressed as \vec{a}_n instead of \vec{r}_n to denote they are assumed constant)
- m_{nuclei} , m_e : nuclei mass and electron mass respectively
- \vec{u}_{nuclei} , \vec{u}_e : nuclei velocity and electron velocity respectively

In equation (2.2) it is shown how the electrons wave function depends on the nuclei positions, but they are expressed as \vec{a}_n instead of \vec{r}_n . This is because they are not supposed to move on the electrons system of inertia and so there they are “seen” as the fixed \vec{r}_n positions. Thus to avoid any confusion they are now symbolized as \vec{a}_n . Furthermore, since these positions are fixed for the electrons wave function, the \vec{r}_n become parameters here, and so it can be written:

$$\Psi_e(\{\vec{r}_m\}, \{\vec{a}_n\}) = \Psi_e(\{\vec{r}_m\}) \quad (2.3)$$

Then the electrons wave function (and so the one for nuclei) will satisfy Schrodinger equation since the energy of the system of the electrons will not interact with the one of the nuclei. From equations (2.1), (2.3):

$$\hat{H} \cdot \Psi_e(\{\vec{r}_m\}) = E \cdot \Psi_e(\{\vec{r}_m\}) \quad (2.4)$$

Since equation (2.4) refers only to the electrons and how they respond, the Hamiltonian will as well refer only to the operators that act on electrons. This means that \hat{H} can be calculated as:

$$\hat{H} = \hat{T} + \hat{V}_{\text{coulomb}} = -\frac{\hbar^2}{8 \cdot \pi^2 \cdot m_e} \cdot \sum_m^{N_e} \nabla^2 + \frac{1}{8 \cdot \pi \cdot \epsilon_0} \cdot \sum_m^{N_e} \sum_n^{N_n} \frac{e^2}{|\vec{r}_m - \vec{r}_n|} + \frac{1}{8 \cdot \pi \cdot \epsilon_0} \cdot \sum_{m1}^{N_e} \sum_{m2 > m1}^{N_e} \frac{e^2}{|\vec{r}_{m1} - \vec{r}_{m2}|} \quad (2.5)$$

Equation (2.4) is an Eigen - Value problem at which E is the Eigen - Value table of table \hat{H} and then $\Psi_e(\{\vec{r}_m\})$ are the Eigen - Functions in the form of $\Psi_e(\{\vec{r}_m\}) = \{\Psi_{e1}(\{\vec{r}_m\}), \Psi_{e2}(\{\vec{r}_m\}) \dots, \Psi_{eNe}(\{\vec{r}_m\})\}$.

So the orbital of each m electron is found as the Eigen - Function $\Psi_{em}(\{\vec{r}_m\})$

The problem with solving equation (2.4) is that in order to find the ground state of a given system of N_e electrons, the dimensions (and so the degrees of freedom) will be:

$$N_e \cdot \dim\{\vec{r}_m\} = N_e \cdot 4$$

Where:

- N_e : the number of electrons involved in the system

This means that it is not efficient to calculate and find numerical solutions of equation (2.4), for systems containing moles and solid materials or anything else that involves a big number of electrons.

Density functional theory suggests a methodology at which instead of $(N_e \cdot 4)$ degrees of freedom, each problem only contains 4 (at least), according to [10]. This is achieved by using the electron density instead of each electron's wave function, as the variable that defines the state of the system.

The definition of electron density is as follows [6], [10], [11]:

$$n(\vec{r}) = N_e \cdot \int \dots \int \left(\Psi_e(\{\vec{r}_m\}) \cdot \Psi_e^*(\{\vec{r}_m\}) \right) ds_1 d\vec{r}_2 d\vec{r}_3 \dots d\vec{r}_{N_e} \quad (2.6)$$

Equation (2.6) shows that the probability of finding an electron at the \vec{r} position depends only on the amplitude of the total electron wave function, and so instead of having $(N_e \cdot 4)$ degrees of freedom, by calculating $n(\vec{r})$ the problem will only contain 4 degrees of freedom (the position and spin of the supposed electron).

Hartree – Fock Product approximation [18]

The problem when solving equation (2.6) is the difficulty finding the total wave function that can describe all the electrons in a system.

The basic idea of Hartree - Fock theory [18] is the assumption that the electrons don't interact with each other (so that Coulomb's energy between them equals 0). If that was true, then the Hamiltonian would be separable, and the total electronic wave function would be easily calculated as the product of each electron's wave function as follows [6], [9], [10], [11]:

$$\Psi_e(\{\vec{r}_m\}) = \Psi_{e1}(\vec{r}_1) \cdot \Psi_{e2}(\vec{r}_2) \cdot \dots \cdot \Psi_{eNe}(\vec{r}_{Ne}) \quad (2.7)$$

Considering the total system 's wave function can be simplified as it is shown in equation (2.7), then in this case equation (2.6) will become:

$$n(\vec{r}) = \sum_m^{Ne} \Psi_{em}(\vec{r}) \cdot \Psi_{em}^*(\vec{r}) \quad (2.8)$$

Obviously, pretending that the electrons ignore each other is a big simplification. Nevertheless, this is just a first approximation and it will be corrected when solving Schrodinger equation afterwards (in equation 2.9 the term E_{XC}).

Density functional theory is mostly related to the two following theorems introduced by Hohenberg and Kohn [19] at 1964, and widely used since then in quantum mechanics [6],[9],[10],[11]:

Hohenberg–Kohn Theorem 1 [19]: The ground state energy of any given system is a unique functional of the electron density. The above is expressed as:

$$E = E[n(\vec{r})] \Rightarrow \text{the electron density defines the value of total energy}$$

Hohenberg–Kohn Theorem 2 [19]: The electron density that minimizes the energy of the overall functional is the true ground state electron density. The above is expressed as:

$$E[n(\vec{r})] > E_0[n_0(\vec{r})] \Rightarrow \text{Schrodinger equation is true only for } E = E_0[n_0(\vec{r})]$$

Köhn - Sham Method [20]

The two theorems of density functional theory, imply that the Hamiltonian (energy operator) can be expressed as a function of electron density instead of every single electron's position \vec{r}_m .

Taking into account the Hartree - Fock simplification made above (equations 2.7, 2.8) and equation (2.5), the energy of the system can finally be expressed using the interaction of electrons added on the total energy summation [6], [9],[10],[11], as it was introduced by W. Kohn and L .J Sham in 1965 [20]:

$$E = \frac{\hbar^2}{8 \cdot \pi^2 \cdot m_e} \cdot \left[- \sum_m^{N_e} \int \Psi_{em}(\vec{r}) \nabla^2 \Psi_{em}^*(\vec{r}) d\vec{r} - \sum_{n=1}^{N_n} N_n \int \frac{n(\vec{r})}{|\vec{r}_n - \vec{r}|} d\vec{r} + \iint \frac{n(\vec{r}) \cdot n(\vec{x})}{|\vec{r} - \vec{x}|} d\vec{r} \cdot d\vec{x} \right] - E_{XC} \quad (2.9)$$

Where:

- E_{XC} : the exchange correlation energy between the electrons of the system

Equation (2.9) gives the expression for the total energy as a function of the electron density. The term E_{XC} is added as a correction for the approximation made in equations (2.7) and (2.8) from Hartree – Fock about the non – interacting electrons.

It is obvious from equation (2.9) that without knowing the wave functions and so the positions of the electrons, it is possible to calculate the system's energy and define it's ground state if the electron density and the exchange correlation energy are known.

The analytical expression ends with equation (2.9). At this point in order to give solutions to the ground state of a system, equation (2.9) will be solved numerically. The suggested methodology [10] is as follows:

- a) At first a random guess of the electron density 's value is made
- b) Then equation (2.9) uses this value and calculates the system 's energy
- c) With E known, equation (2.4) can be solved as an eigenvalue problem, with E being the Eigen-Value table of table \hat{H} . The solution obtained is the Eigen-Functions $\Psi_{em}(\vec{r})$ responding to each m electron
- d) With $\Psi_{em}(\vec{r})$ known equation (2.8) gives the value of electron density $n(\vec{r})$
- e) Comparing the electron density $n(\vec{r})$ from step (a) and step (d) the process will either end here (in case of negligible deviation) or it will be repeated with step (a) estimating the electron density again from the beginning (equal to the one calculated is (d) this time).

- f) The procedure of steps (a) – (e) should be repeated until convergence of the value of electron density
- g) $n(\vec{r})$ is ensured. The final value calculated for the electron density is considered as the true one in ground state.

2.2.1.3: Density Functional Theory - Application on Corrosion ^[5]

For the better understanding of how nano – scale corrosion modelling works, a model [5] is presented in this section. The particular model uses density functional theory for the necessary calculations in order to predict the behavior of a structure containing a pre-covered with oxygen iron surface, when exposed to water.

It is well known how iron surfaces suffer from corrosion when exposed to aqueous environments. However, the complicated aqueous corrosion mechanism of iron is not fully understood from microscopic levels. Participation of oxygen and water molecules plays a major role in the process of aqueous corrosion. The purpose of this theoretical study [5] is to present a direction for an elucidation of iron aqueous-corrosion reactions from a microscopic point of view. The microscopic approach for iron aqueous corrosions was made for an iron surface using DFT-based computer simulations. The examined surface was pre-covered with oxygen, and then exposed in water. The simulation was performed using the software SIESTA. The particular software calculates the ground state of a given system, by the methodology of Density Functional Theory. The following table, shows all the parameters selected by the user for the simulation.

Table 2.1: The input parameters for the model

Parameter for the model	Value	Explanation
Crystal Lattice type for Iron Surface	bcc	Iron 's metallic structure
Miller Indices for Iron Surface	(100)	Exposed iron surface
Lattice parameter for Iron Surface	a=2.882Å	Calculated (Dft) for the bcc (100) structure
Temperature of electrons	300 K	Electron temperature
Oxygen atoms coverage $O_s / Fe(100)$	0.25ML	Pre – covering substance amount
Water (H ₂ O) adsorbed on the slab	1 mol	Corrosive environment

The modelled geometry for the simulation (from the data obtained from table 2.1), is shown in figure 2.1. The pre-covered oxygen atoms are symbolized as O_s and they were located at four-fold hollow site [17], meaning that an oxygen O_s was located on the area enclosed by 4 atoms of iron (Fe). The coverage amount corresponded to 0.25ML where ML refers to the fraction $O_s / \text{Fe}(100)$ of atoms found in a unit cell [12]. The corrosion simulation involved the adsorption of the H_2O molecule, which as shown in figure 2.1, contains oxygen atoms O_w and hydrogen atoms H (grey spheres in figure 2.1) which will also be placed on the crystal lattice within the DFT calculations.

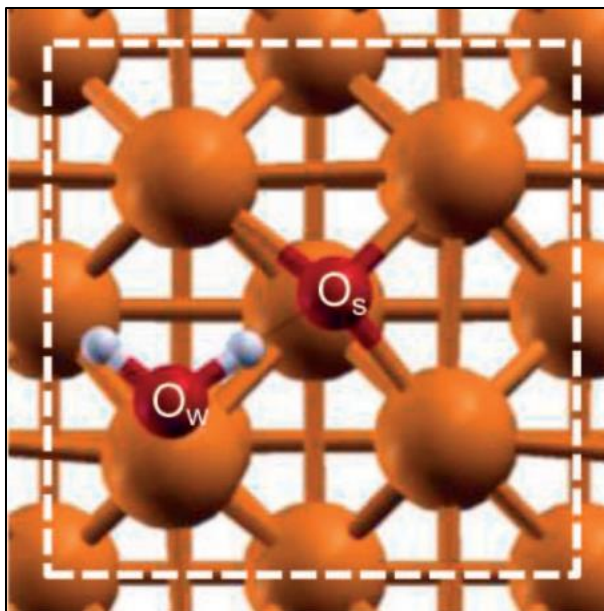


Figure 2.1: Top view of the modeled structure of Fe (100) with pre - covered oxygen on SIESTA software on Fe(100) surface using DFT-based computer simulations [5]

The DFT calculations for the corrosion evaluation, define the electron density all over the structure. Figure 2.2 shows the results for the electron density, by presenting the isosurface variations of it on the structure. Particularly, the red regions in figure 2.2 correspond to the raise of $0.004 \text{ e}\text{\AA}^{-3}$ electron density, and the blue regions in figure 2.2 to the loss of $0.004 \text{ e}\text{\AA}^{-3}$ electron density.

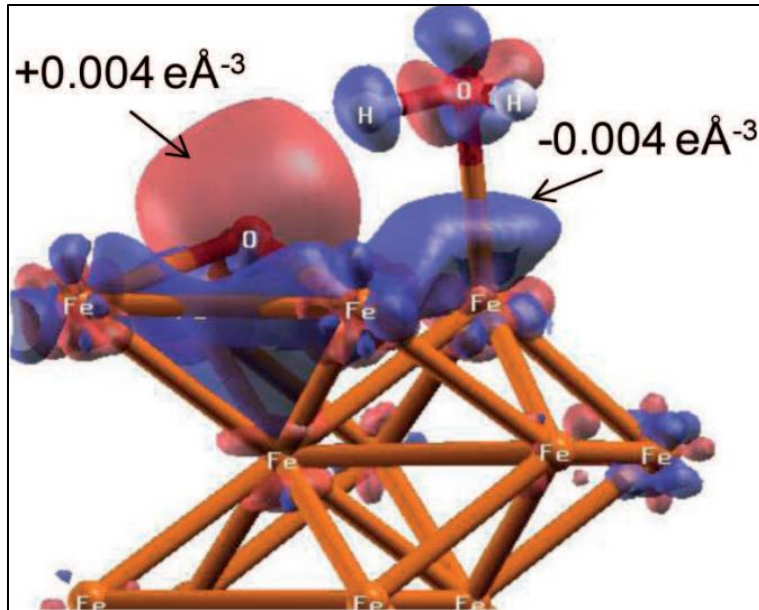


Figure 2.2: Results of the SIESTA software simulation showing the isosurface variations in the adsorption-induced electron density change for an adsorbed H_2O molecule on oxygen-covered Fe (100) of 0.25 ML coverage. Red (blue) region indicates a gain (loss) of electron density [5]

Proceeding the DFT calculations, in order to evaluate the effect of pre – covering the iron surface with oxygen (O_s atoms), multiple simulations made for different values of the coverage parameter. In particular, apart from the 0.25 ML coverage of oxygen atoms (as denoted in table 2.1), the model was executed for a few more values of the coverage within the interval of 0.25 to 1 ML. The results are shown in figure 2.3.

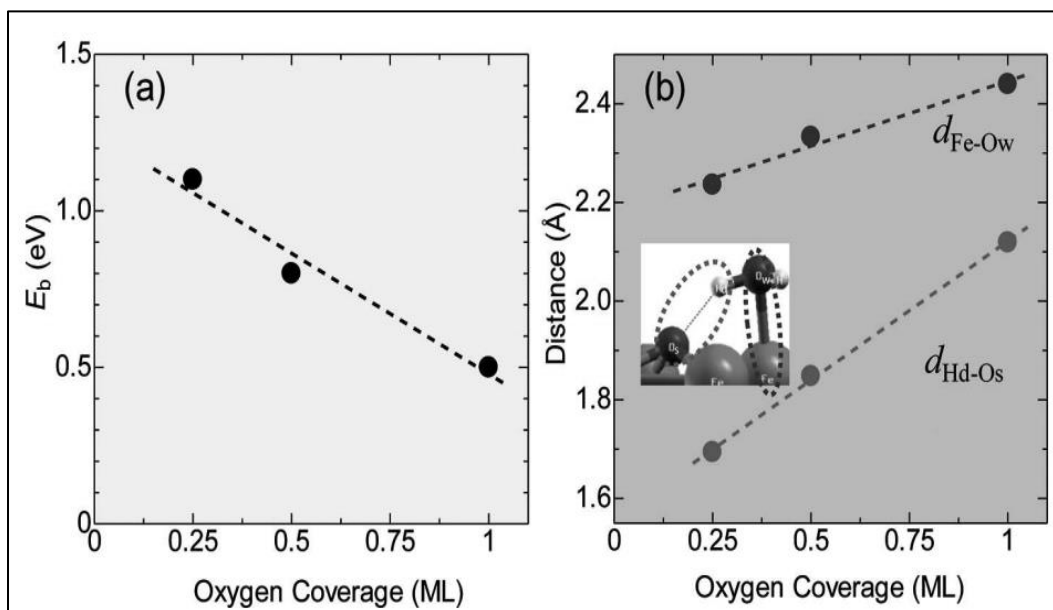


Figure 2.3: (a) Calculated binding energies (E_b) as a function of oxygen coverage and (b) atomic distance as a function of oxygen coverage. [5]

Figure 2.3a shows the results for the binding energies of the water molecule with the iron structure, calculated for the whole geometry, as a function of the amount of the pre-covered oxygen atoms O_s . Figure 2.3b shows the results for the distances of iron – oxygen from water (d_{Fe-O_w}), and the distances of hydrogen – pre-covered oxygen ($d_{H_d-O_s}$), respectively. However, as the binding energies decrease and the above distances increase, the corrosion rate decreases since the reactions on the iron surface slow down. This means that from figures 2.3a and 2.3b it is clear how the corrosion rate decreases, as more oxygen pre-covers the iron surface.

Finally, the calculations for 0.25 ML coverage of oxygen were again made by the software. The aim now was to calculate the distances of different atoms (and so the reaction rates between them) as functions of time. The obtained results are shown in figure 2.4 following.

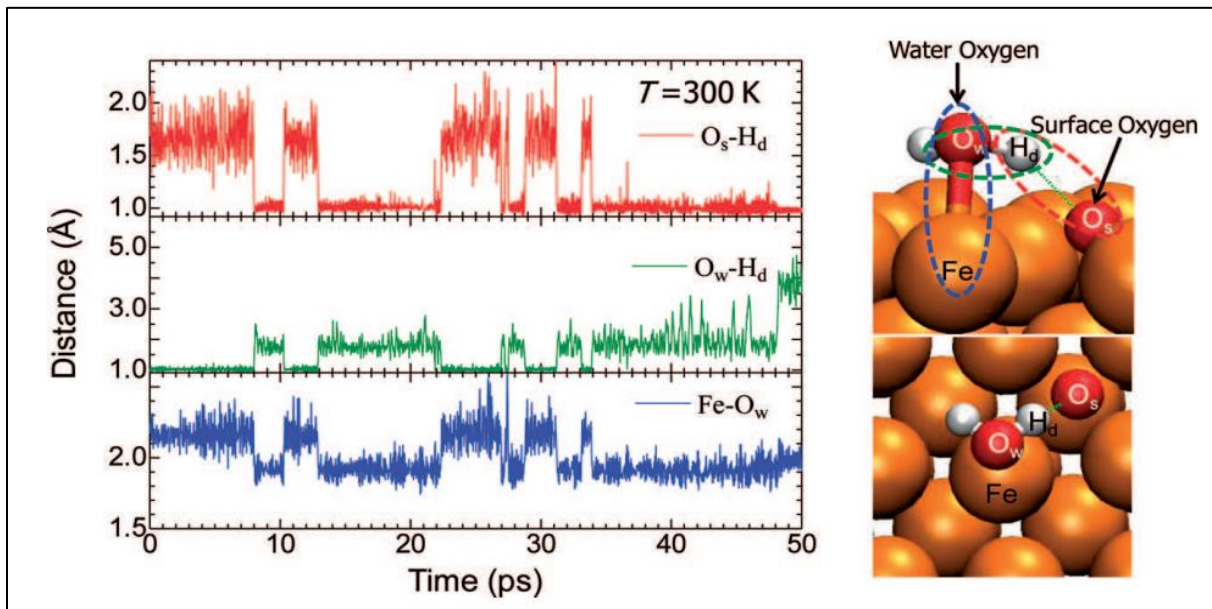


Figure 2.4 : Time dependence of the atom to atom distances calculated for an adsorbed H_2O molecule on oxygen-covered Fe(100) of 0.25 ML coverage and temperature of 300K [5]

Figure 2.4 shows the atomic distances calculations within the density functional theory method. The results show that whenever the distance between oxygen from the water molecule and hydrogen $d_{H_d-O_w}$ increases (indicating the dissociation reaction of water), the oxygen and iron distance d_{Fe-O_w} decreases (indicating the increase of the iron oxide forming) and the surface oxygen and hydrogen distance $d_{H_d-O_s}$ decreases (indicating the increase of hydrogen adsorption). This result has suggested the process of the hydroxylation on the surface of iron.

This model proves (see figures 2.3) that as surface oxygen pre-coverage increases, the surface is less activated, which makes the adsorption of water on the surface weaker.

2.2.2: Analytical Corrosion Modelling

2.2.2.1: Introduction

In the corrosion phenomena due to the many undetectable variables that affect the procedure it is impossible to describe them by applying fundamental equations. Therefore, the production of any mathematical expression capable of predicting any of the aforementioned variables, requires the study and development of analytical models. These models vary a lot depending not only on the way and stage of the material's corrosion but also on the way that the subject is approached. For example, when studying galvanic corrosion, the variables affecting this procedure are mostly studied with the use of electrochemistry as it can explain the highest percentage of the occurring phenomena. However, types of corrosion that involve stress and strain, are usually approached by mechanics, whereas uniform corrosion has also been studied by thermodynamics. In any case, apart from the physics that describe a corroding system, the mathematical tools used are mostly partial differential equations.

Concluding, analytical modelling of corrosion, is a complex procedure that involves more than one scientific field and usually combinations of them.

2.2.2.2: Analytical model – Application on Fatigue Crack Corrosion ^[13]

For the better understanding of how an analytical model can be generated and therefore describe a specific type of corrosion, a model [13] is presented in this section. The particular model refers to a material undergoing fatigue crack corrosion. This means that the system is constituted by the simultaneous act of repeatedly applied loads whilst exposed in a corroding environment. According to [1] the combination of fatigue and corrosion on a metallic structure can worsen both the fatigue effects (-crack growth) and the corrosion evolution. This complicated relationship between these two is what makes their prediction hard, thus leading to a necessity of an analytical model.

The purpose of this theoretical study [13] is the production of an appropriate mathematical expression to assess the residual life of corrosion fatigue crack growth for metallic alloys. The physics used is a modification of the fatigue theory, which introduces necessary variables to take into account the corrosion effects.

The developed methodology was examined and applied to 2524-T3 and 7050-T7451 aluminum alloys. The model aims to predict the same results that would be experimentally obtained via fatigue crack growth tests. The experiments were also used in the end for the model's verification. These tests were carried out on 2524-T3 and 7050-T7451 aluminum alloys subjected to actual spectra loading at three reference stress levels of 109 MPa, 91 MPa and 68 MPa under the environments of dry air and 3.5%NaCl solution to separately model the pure and under corrosion fatigue crack growth lives. The specimens of 2524-T3 and 7050-T7451 aluminum-alloys, respectively, have the initial artificial prefabricated crack sizes α_0 of 6 mm and 8 mm through linear cutting and polishing.

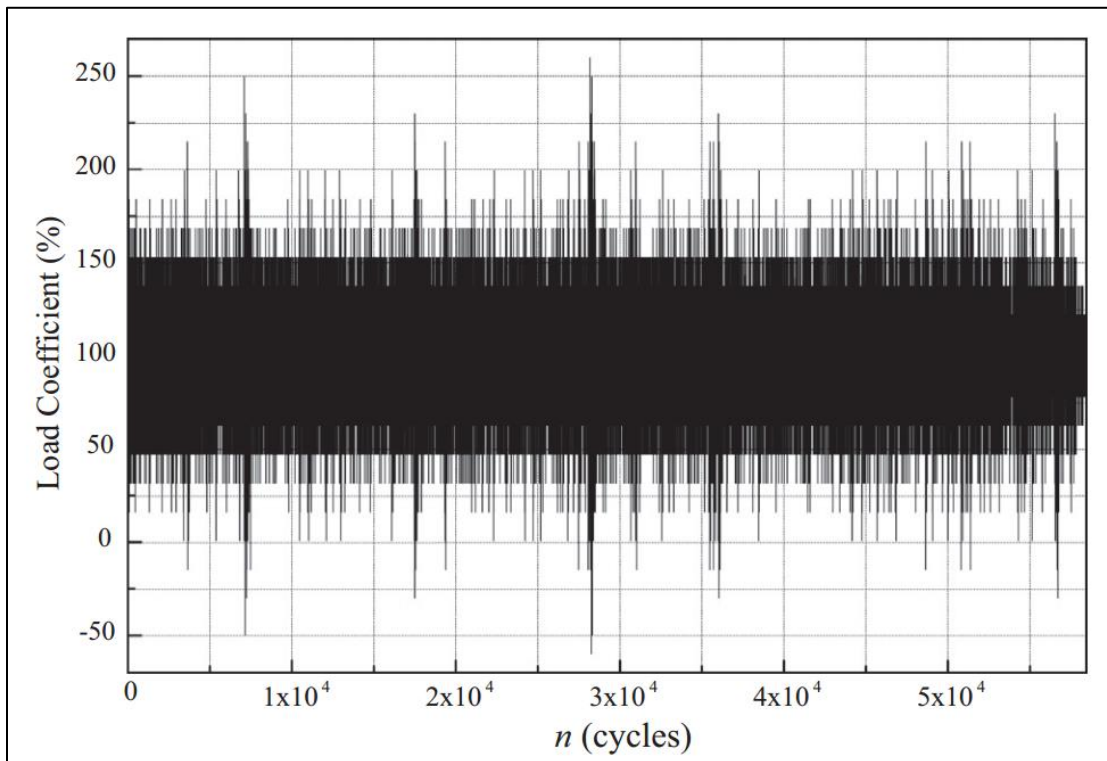


Figure 2.5: The applied – experimental load spectra that the model refers to. [13]

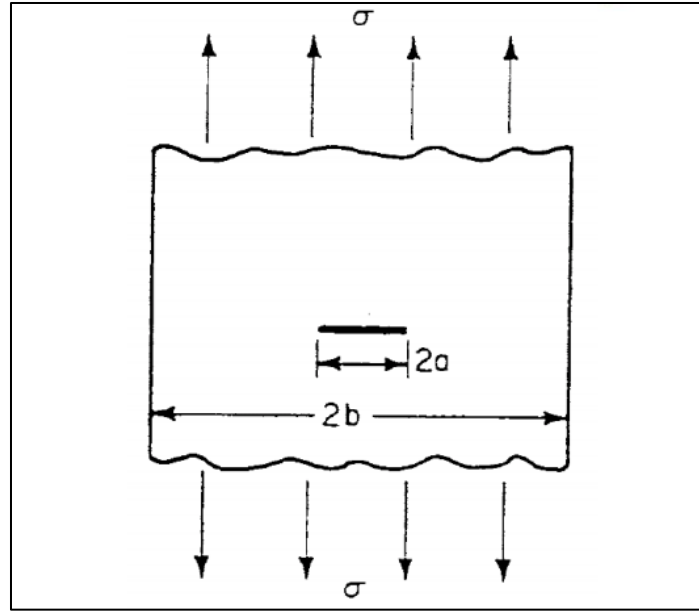


Figure 2.6: A cracked specimen geometry similar to the one used in the model's [13] experiments. [12]

According to the [2], [12], the stress intensity factor for the particular specimen (with central crack) is expressed as:

$$K = \left[\frac{2 \cdot b}{\pi \cdot \alpha} \tan \left(\frac{2 \cdot b}{\pi \cdot \alpha} \right) \right]^{1/2} \cdot \sigma \cdot \sqrt{\pi \cdot \alpha} \quad (2.10)$$

And the fatigue crack growth rate can be expressed as:

$$\frac{d\alpha}{dN} = \left\{ \begin{array}{ll} C \cdot (\Delta K - \Delta K_{th})^{m_1} \cdot (1-R)^{m_2} & , \quad \Delta K \geq \Delta K_{th} \\ 0 & , \quad \Delta K \leq \Delta K_{th} \end{array} \right\} \quad (2.11)$$

Where:

- N : the current number of stress cycles
- b : half of specimen 's width in mm (see figure 2.6)
- σ : the stress acting on the specimen in MPa (see figure 2.6)
- α : the crack length in mm (with respect to the N cycle)
- R: stress ratio so that $R = \frac{\sigma_{min}}{\sigma_{max}}$
- K: stress intensity factor (function of α and σ) in $MPa \cdot mm^{0.5}$
- ΔK : the stress intensity factor 's range in $MPa \cdot mm^{0.5}$ so that $\Delta K = K_{max} - K_{min}$

- ΔK_{th} : the value of ΔK at the threshold (-at the point where the crack is supposed to start propagating) in $MPa \cdot mm^{0.5}$
- C, m_1, m_2 : constants depending on the material and the corrosive environment, that will be determined from experimental datasets

The problem with equation (2.11) is that it does not take into consideration the load interaction's significant effect on fatigue crack growth under random spectra loading. This is because of the effects of tensile overload retardation and compressive load acceleration as well as the reduction of overload retardation effect caused by the compressive load immediately following the tensile overload. Hereby, it is desirable to have the model to address these features by considering the above effects for residual life prediction of fatigue crack growth under random spectra loading. According to plastic zone theory the effective stress ratio R_{eff} at crack tip depicts the load interaction effect on fatigue crack growth under random spectra loading. Considering the above, equation (2.11) can be modified to:

$$\frac{d\alpha}{dN} = \left\{ \begin{array}{ll} C \cdot (\Delta K - \Delta K_{th})^{m_1} \cdot (1 - R_{eff})^{m_2} & , \quad \Delta K \geq \Delta K_{th} \\ 0 & , \quad \Delta K \leq \Delta K_{th} \end{array} \right\} \quad (2.12)$$

Where:

$$\left\{ \begin{array}{l} R_{eff} = 1 - \frac{\Delta K}{(K_{max})_{eff}} \text{ is the effective stress ratio} \\ (K_{max})_{eff} = K_{max} - \frac{(K_{max})_{OL} - (K_{max})_{th}}{(R_{OL} - 1) \cdot (K_{max})_{OL}} \cdot \left((K_{max})_{OL} \sqrt{1 - \frac{\Delta \alpha'}{Z_{OL}}} - K_{max} \right) \text{ is the effective spectra peak value of } K \\ (K_{max})_{th} = \frac{\Delta K_{th}}{1 - R} \text{ is the spectra peak stress intensity factor of overload stress cycles} \\ Z_{OL} = \frac{1}{2\pi} \cdot \left(\frac{K_{max}}{\sigma_b} \right)^2 \text{ is the size of overload retardation zone} \end{array} \right\} \quad (2.13)$$

For equations (2.13) the following are also defined:

- $(K_{max})_{OL}$: is the spectra peak stress intensity factor of overload stress cycles in $\text{MPa}\cdot\text{mm}^{0.5}$
- $\Delta\alpha'$: is the incremental crack growth following the overload in mm
- σ_b : is the tensile ultimate strength in MPa
- r : overload shut-off ratio

By assuming small $\Delta\alpha_i$ ranges to approximate $d\alpha$ in Equation (2.12), for the i^{th} stress cycle under a certain spectrum loading, the crack growth increment can be calculated:

$$\frac{d\alpha}{dN} = \left(\frac{\Delta\alpha}{\Delta N}\right)_i \Rightarrow \Delta\alpha_i = \left\{ \begin{array}{ll} C \cdot [(\Delta K)_i - \Delta K_{th}]^{m_1} \cdot [1 - (R_{eff})_i]^{m_2} & , \quad \Delta K \geq \Delta K_{th} \\ 0 & , \quad \Delta K \leq \Delta K_{th} \end{array} \right\} \quad (2.14)$$

From equation (2.14), the current crack growth can be estimated with cycle-by-cycle accumulation.

$$\alpha_{cr} = \sum_{N_1=0}^{N_{failure}} \Delta\alpha_i \quad (2.15)$$

From equation (2.15) it is obvious that for a given α_{cr} we can obtain $N_{failure}$

For a given plane stress fracture toughness of material K_c , failure implies that [2], [12], [14]:

$$K = K_c \xrightarrow{(2.10)} \left[\frac{2 \cdot b}{\pi \cdot \alpha_{cr}} \tan\left(\frac{2 \cdot b}{\pi \cdot \alpha_{cr}}\right) \right]^{1/2} \cdot \sigma \cdot \sqrt{\pi \cdot \alpha_{cr}} = K_c \Rightarrow$$

$$\left[\frac{2 \cdot b}{\pi \cdot \alpha_{cr}} \tan\left(\frac{2 \cdot b}{\pi \cdot \alpha_{cr}}\right) \right] \cdot \alpha_{cr} = \left(\frac{K_c}{\sigma}\right)^2 \cdot \frac{1}{\pi} \quad (2.16)$$

Equation (2.16) can be solved by iterative process and so α_{cr} will be calculated. The final expression is equation (2.15) which calculates $N_{failure}$ (cycles for failure). The variables in equation (2.15) are

calculated through equation (2.14) (with the assistance of equation (2.13)) for the values of $\Delta\alpha_i$, for every i , and through equation (2.16) for α_{cr} .

With the analytical model now expressed via equations (2.13), (2.14), (2.15), (2.16), the next step is to detect the constants contained. From the aforementioned equations, it is clear that C , m_1 , m_2 , ΔK_{th} , K_c , σ_b act as parameters. For their determination, fatigue crack growth tests were performed on 2524-T3 and 7050-T7451 aluminum alloys subjected to constant amplitude loading at three stress ratios (R) of 0.06, 0.3 and 0.5 under the environments of dry air and 3.5% NaCl sodium chloride solution to determine the pure and corrosion fatigue crack growth rate behaviors, respectively.

The necessary experiments were conducted for the aluminum specimen, with predefined parameters as shown in table 2.2.

Table 2.2 : The predefined parameters for the model and experiments

Parameter for the model	Value for 2524-T3	Value for 7050-T7451	Units	Explanation
b	75	75	mm	half of specimen 's width
$R = \sigma_{min}/\sigma_{max}$	0.06, 0.3, 0.5	0.06, 0.3, 0.5	-	stress ratio
σ_b	430	488	Mpa	the tensile ultimate strength
r	2.8	2.8	-	overload shut-off ratio
$K_c = K_c(T)$	From bibliography for $T=25^\circ\text{C}$	From bibliography for $T=25^\circ\text{C}$	$\text{MPa}\cdot\text{mm}^{0.5}$	plane stress fracture toughness

From the experiments, the crack growth per cycle could be evaluated as the distance between two consecutive striations, since each striation corresponds to a load cycle N_i , as explained in [2], [14]. The detection of these distances is available through SEM observation (figure 2.7 can be used as a sample).

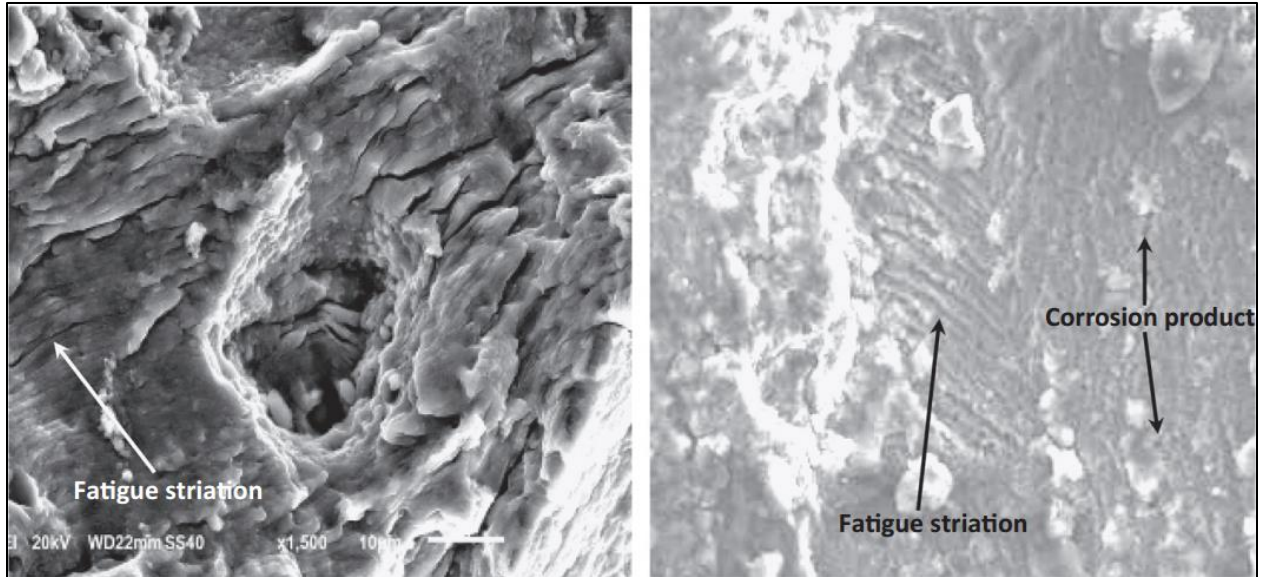


Figure 2.7: Fractographic pictures for 2524-T3 Al alloy subjected to constant amplitude loading ($R = 0.06$, $S_{max} = 182$ MPa). [13]

The experimental data of crack length α_i with respect to the number of stress cycles N_i was determined and the crack growth rate $\left(\frac{d\alpha}{dN}\right)_i$ corresponding to the crack length α_i can be calculated by using any finite difference method (here the secant method was used) on the experimental data $[\alpha_i, N_i]$.

The obtained results are shown in figures 2.8 and 2.9 for 2524-T3 aluminum alloy and 7050-T7451 aluminum alloy, respectively.

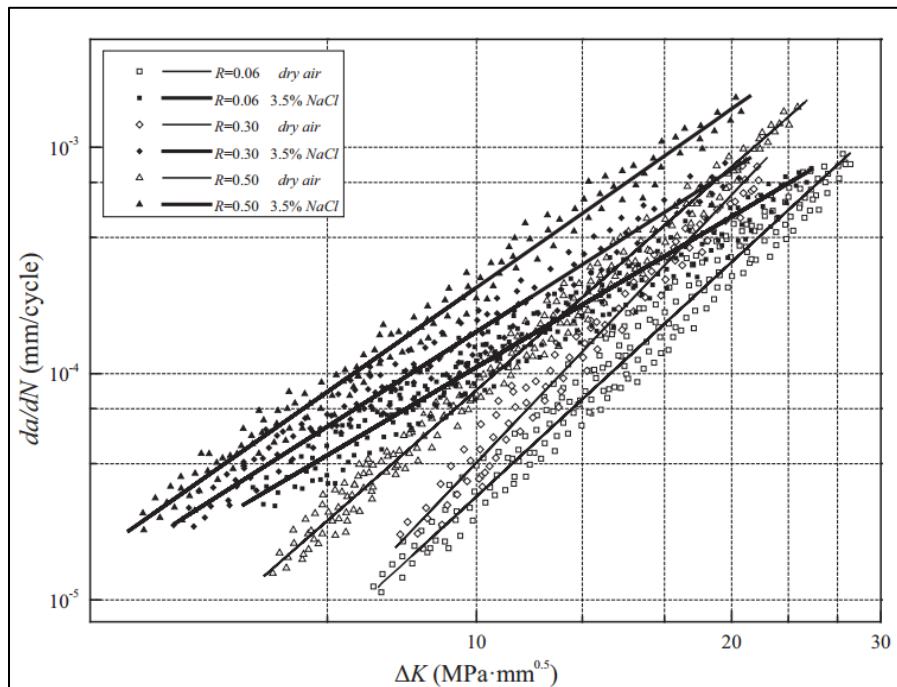


Figure 2.8: Crack growth rate behavior of $d\alpha/dN - \Delta K$ curve for 2524-T3 Al alloy as obtained from the experiments [13]

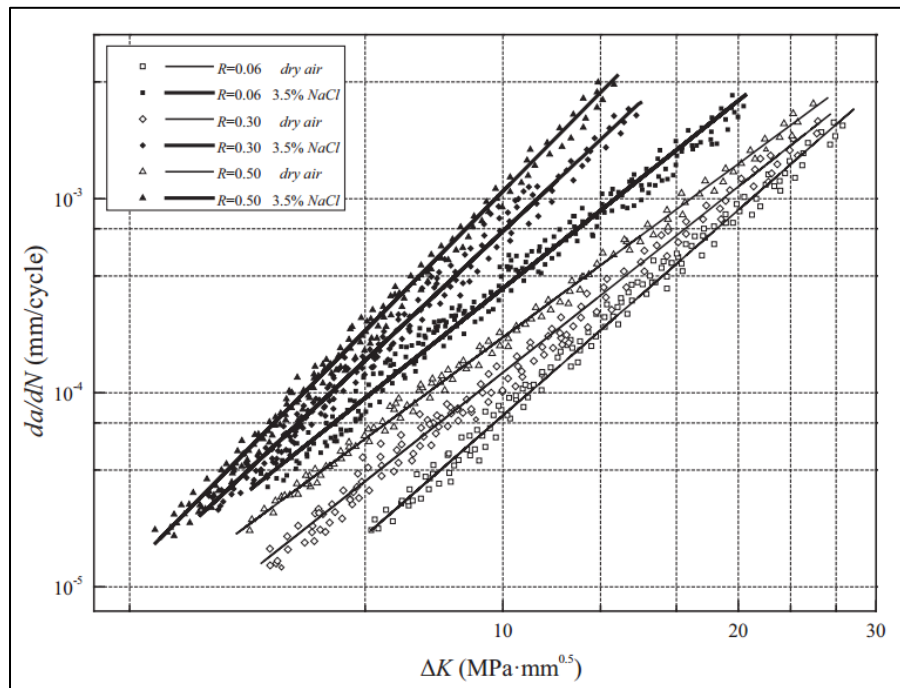


Figure 2.9: Crack growth rate behavior of $d\alpha/dN$ - ΔK curve for 7050-T7451 Al alloy as obtained from the experiments [13]

With the use of the experimental data and the creation of the best fitting lines as seen at the above figures (figures 2.8 and 2.9) it was able to evaluate the necessary for the model constant values. For the better understanding of how three parameters (C , m_1 , m_2) were evaluated out of the experiments the following figures show the three-dimensional representation of figures 2.8 and 2.9. The surfaces $d\alpha/dN$ (ΔK , R) are shown in figures 2.10 and 2.11.

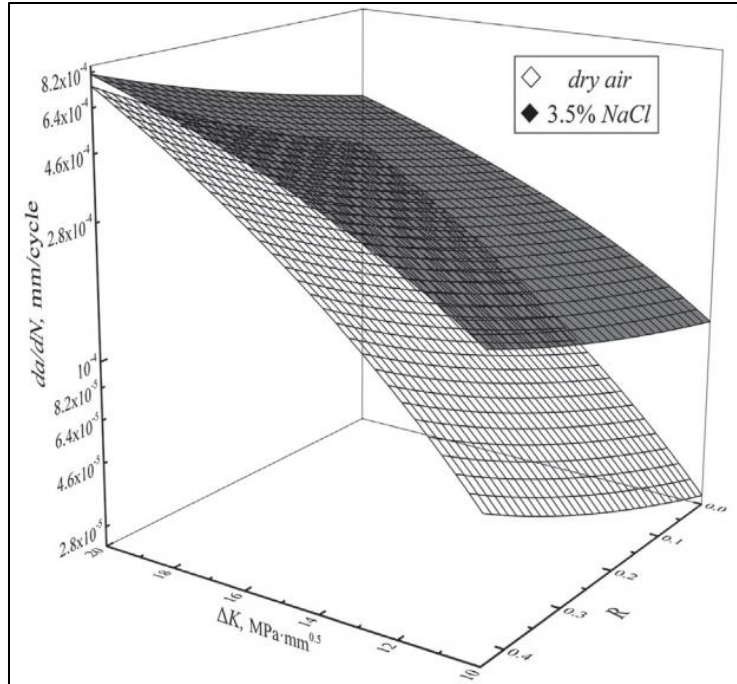


Figure 2.10: Crack growth rate behavior of $d\alpha/dN$ - ΔK - R surface for 2524-T3 Al alloy as obtained from the experiments [13]

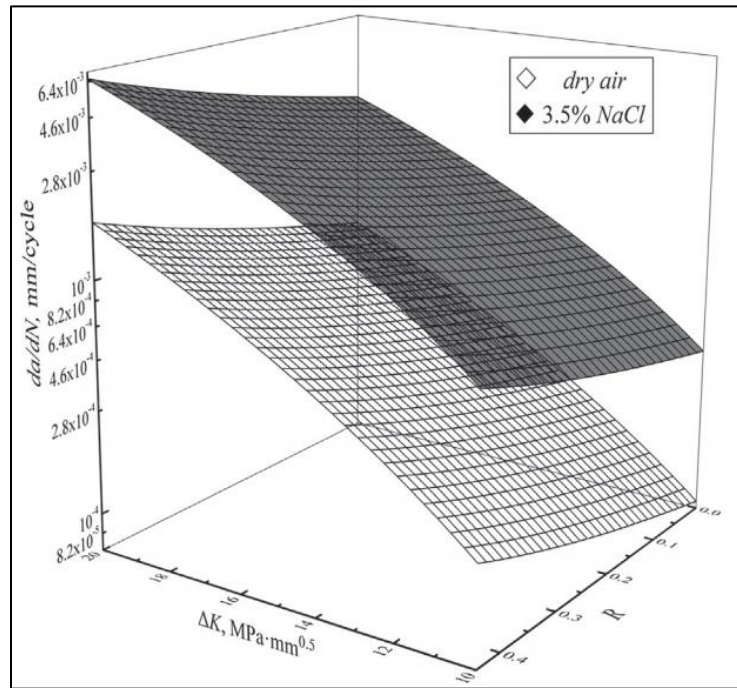


Figure 2.11: Crack growth rate behavior of $d\alpha/dN$ - ΔK - R surface for 7050-T7451 Al alloy as obtained from the experiments

From the above surfaces the final values of the parameters are defined and shown in tables 2.3 and 2.4 along with the parameter ΔK_{th} , which was estimated as the mean value of the starting points (the lowest ΔK) of each $d\alpha/dN$ - ΔK curve (see figures 2.8, 2.9).

Table 2.3: The experimentally obtained parameters for the model for 2524-T3

Parameter for the model	Value for Dry Air	Value for 3.5% NaCl	Units	Explanation
C	$1.58 \cdot 10^{-8}$	$4.76 \cdot 10^{-6}$	mm/(cycle·MPa·mm ^{0.5})	Material - environment constant
m₁	3.29	1.57	-	Material - environment constant
m₂	-1.71	-1.15	-	Material - environment constant
ΔK_{th}	0.52	2.76	MPa·mm ^{0.5}	ΔK at the threshold

Table 2.4: The experimentally obtained parameters for the model for 7050-T7451

Parameter for the model	Value for Dry Air	Value for 3.5% NaCl	Units	Explanation
C	$4.9 \cdot 10^{-8}$	$2.32 \cdot 10^{-6}$	mm/(cycle·MPa·mm ^{0.5})	Material - environment constant
m₁	3.21	2.48	-	Material - environment constant
m₂	-1.54	-1.42	-	Material - environment constant
ΔK_{th}	0.21	2.31	MPa·mm ^{0.5}	ΔK at the threshold

With the replacement of the parameters of tables 2.3 and 2.4 in equation (2.14), the analytical expressions of the particular application are fully defined (see equations 2.17, 2.18 below).

$$\Delta\alpha_i = \left\{ \begin{array}{l} 1.58 \cdot 10^{-8} \cdot [(\Delta K)_i - 0.52]^{3.29} \cdot [1 - (R_{\text{eff}})_i]^{-1.71} \quad , \quad \text{Dry air} \\ 4.76 \cdot 10^{-6} \cdot [(\Delta K)_i - 0.52]^{1.57} \cdot [1 - (R_{\text{eff}})_i]^{-1.15} \quad , \quad \text{3.5\% NaCl} \end{array} \right\} \text{ for 2524-T3 Al alloy (2.17)}$$

$$\Delta\alpha_i = \left\{ \begin{array}{l} 4.9 \cdot 10^{-8} \cdot [(\Delta K)_i - 0.21]^{3.21} \cdot [1 - (R_{\text{eff}})_i]^{-1.54} \quad , \quad \text{Dry air} \\ 2.32 \cdot 10^{-6} \cdot [(\Delta K)_i - 2.31]^{2.48} \cdot [1 - (R_{\text{eff}})_i]^{-1.42} \quad , \quad \text{3.5\% NaCl} \end{array} \right\} \text{ for 7050-T7451 Al alloy (2.18)}$$

For verification of expressions (2.17) and (2.18), experimental values of the residual lives of corrosion fatigue crack growth were measured. The experiment corresponds to random spectra loading (see figure 2.5).

For selected amplitudes inside the spectra, expressions (2.17) and (2.18) were used along with (2.13), (2.15) and (2.16) in order to calculate the modelled residual lives of corrosion fatigue crack growth. The comparison is shown in table 2.5.

Aluminum alloy	Environment	Load (MPa)	Experimental $N_{failure} (\times 10^4)$	Modelled $N_{failure} (\times 10^4)$	Relative deviation (%)
2524-T3	Dry air	109	4.44	3.43	22.7
2524-T3	Dry air	91	7.44	6.19	16.8
2524-T3	3.5% NaCl	109	3.45	4.36	26.4
2524-T3	3.5% NaCl	91	5.14	6.12	19.1
7050-T7451	Dry air	68	4.9	4.39	10.4
7050-T7451	3.5% NaCl	68	1.25	1.47	17.6

Concluding from the model it is obvious that:

- there is good agreement between the experimental data and the predicted (-modelled) values (see table 2.5)
- The values of C in 3.5% NaCl sodium chloride solution are greater compared to these in dry air (tables 2.3, 2.4). This means that inside a corrosive environment crack propagation per cycle is greater, denoting the contribution of the corrosive environment on the crack growth.

2.2.3: Statistical Corrosion Modelling

2.2.3.1: Introduction

Another way of approaching corrosion is with the use of statistical analysis. This is mainly applied in big industries, where the structures are complex and their maintenance seems to have a uniform procedure and is massively done. A characteristic example is that of the inspection and maintenance rules that have been set for ships. Any physical analysis of how a ship corrodes, aiming to catholically explain - predict this behavior would be widely impractical. Marine structure corrosion can occur in many different ways according to [1]. This is mainly due to the vast variety of the location, structural geometry, environmental conditions and operational use (load carrying) of each component of the ship. As it has been explained in chapter 1 the above parameters can affect widely the behavior of the corroding material. In addition, the variety of uncertainties during the evolution of the process (e.g. the application corrosion protection systems), make the physical analysis of a system that includes corrosion, even more difficult.

2.2.3.2: Statistical model – Application on ship’s corrosion ^[15]

For the better understanding of how statistical corrosion modelling works, a model [15] is presented in this section. The particular work made by Jeom Paik [15], is a mathematical model used for predicting time - variant corrosion wastage of the structures of single and double-hull tankers. In this section the methodology proposed by Paik [15] is analyzed and explained thoroughly and indicative results of the publication are presented followed by personal conclusions about the methodology.

A set of time dependent corrosion wastage models for 34 different structural members (considering plates, webs and stiffeners) grouped by type and location are developed. The models were produced with the use of statistical analysis conducted on corrosion measurements data. The study [15] examines the cases of both general (-uniform) and local corrosion. Therefore, the data gathered, derive from measurements corresponding to both cases. However, the contribution percentage of each in the sample space used, is not clarified.

The first step of the study is to explain the rules and abbreviations used for the definition of the several parts of the ship as shown in table 2.6 and figures 2.12, 2.13, respectively.

Symbol	Meaning
A	Exposed to Air
B	Exposed to Ballast Water
O	Exposed to Air
S	Exposed to Air
W	Referring to Web
F	Referring to flange
H	Horizontal member
V	Vertical member
COT	Exposed to Cargo Oil Tank
WBT	Exposed to Water ballast tank

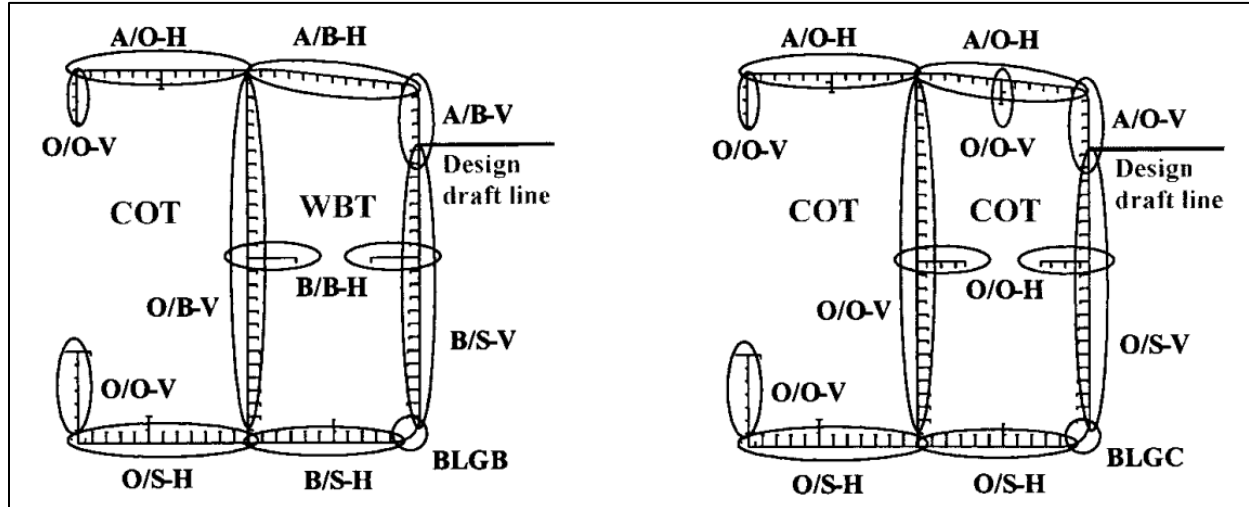


Figure 2.12.: The plating member groups defined schematically for typical single-skin tanker structures [15]

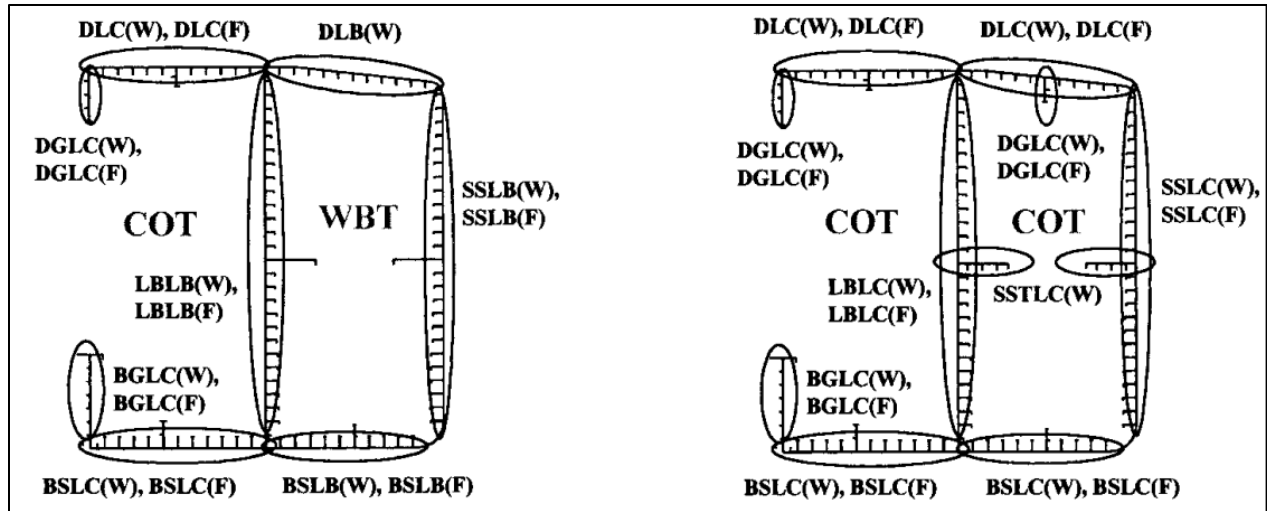


Figure 2.13.: The stiffener member groups defined schematically for typical single-skin tanker structures [15]

For the statistical analysis of how corrosion evolves on a tanker, the amount of data gathered and studied for each part of the ship is shown in figure 2.14

ID No.	Member Type	Example	No. of Data
1	B/S-H	Bottom shell plating (segregated ballast tank)	148
2	A/B-H	Deck plating (segregated ballast tank)	1,410
3	A/B-V	Side shell plating above draft line (segregated ballast tank)	33
4	B/S-V	Side shell plating below draft line (segregated ballast tank)	274
5	BLGB	Bilge plating (segregated ballast tank)	164
6	O/B-V	Longitudinal bulkhead plating (segregated ballast tank)	361
7	B/B-H	Stringer plating (segregated ballast tank)	19
8	O/S-H	Bottom shell plating (cargo oil tank)	849
9	A/O-H	Deck plating (cargo oil tank)	5,557
10	A/O-V	Side shell plating above draft line (cargo oil tank)	86
11	O/S-V	Side shell plating below draft line (cargo oil tank)	692
12	BLGC	Bilge plating (cargo oil tank)	348
13	O/O-V	Longitudinal bulkhead plating (cargo oil tank)	1,082
14	O/O-H	Stringer plating (cargo oil tank)	42
15	BSLB(W)	Bottom shell longitudinals in ballast tank, web	672
16	BSLB(F)	Bottom shell longitudinals in ballast tank, flange	678
17	DLB(W)	Deck longitudinals in ballast tank, web	975
18	SSLB(W)	Side shell longitudinals in ballast tank, web	913
19	SSLB(F)	Side shell longitudinals in ballast tank, flange	913
20	LBLB(W)	Longitudinal bulkhead longitudinals in ballast tank, web	1,024
21	LBLB(F)	Longitudinal bulkhead longitudinals in ballast tank, flange	973
22	BSLC(W)	Bottom shell longitudinals in cargo oil tank, web	2,030
23	BSLC(F)	Bottom shell longitudinals in cargo oil tank, flange	2,205
24	DLC(W)	Deck longitudinals in cargo oil tank, web	2,215
25	DLC(F)	Deck longitudinals in cargo oil tank, flange	34
26	SSLC(W)	Side shell longitudinals in cargo oil tank, web	2,187
27	SSLC(F)	Side shell longitudinals in cargo oil tank, flange	2,091
28	LBLC(W)	Longitudinal bulkhead longitudinals in cargo oil tank, web	2,850
29	LBLC(F)	Longitudinal bulkhead longitudinals in cargo oil tank, flange	2,634
30	BGLC(W)	Bottom girder longitudinals in cargo oil tank, web	154
31	BGLC(F)	Bottom girder longitudinals in cargo oil tank, flange	42
32	DGLC(W)	Deck girder longitudinals in cargo oil tank, web	94
33	DGLC(F)	Deck girder longitudinals in cargo oil tank, flange	36
34	SSTLC(W)	Side stringer longitudinals in cargo oil tank, web	35
Total			33,820

Figure 2.14: Number of gathered data from thickness measurements for 34 primary structural member groups in oil tanker structures [15]

The models can be used for predicting the depth of corrosion in oil tanker structures. The study of the corrosion process for a coated marine steel structure, can be modeled [15] in a way that the corrosion is represented by curves as the ones shown in figure 2.15.

At first we define:

- t_r : depth of corrosion wastage (mm)
- T_e : time of exposure under corrosion environment (year)
- C_1, C_2 : coefficients to be determined by the statistical analysis of corrosion data
- T_c : life of coating (year)
- T_t : duration of transition (year)
- T : age of vessel (year)
- r_r : annualized corrosion rate (mm/year)

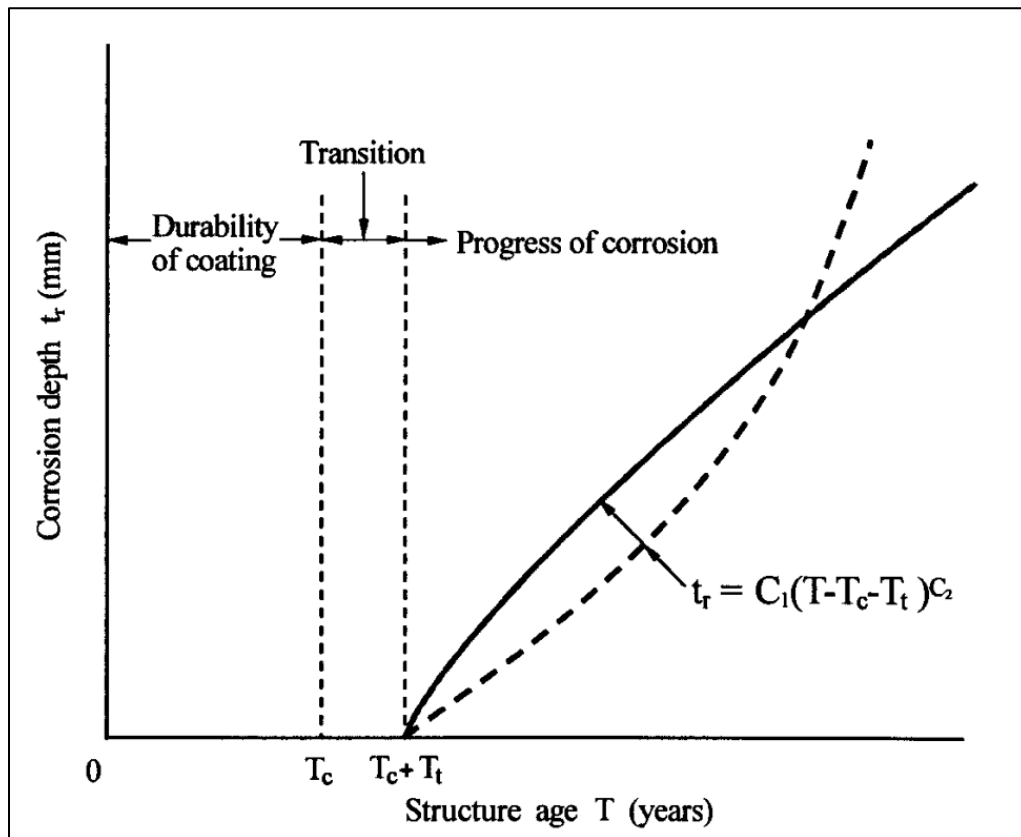


Figure 2.15: A schematic of a corrosion process model for marine structures [15]

Thus, the corrosion behavior in this model [15] is categorized into three phases:

- a) durability of coating, T_c
- b) transition to visibly obvious corrosion, T_t
- c) progress of such corrosion, $T_e = T - T_t - T_c$

The equation corresponding to the above curves (figure 2.15) is:

$$t_r = C_1 \cdot T_e^{C_2} \Rightarrow t_r = C_1 \cdot (T - T_t - T_c)^{C_2} \quad (2.19)$$

Corrosion rate can be expressed as the gradient of corrosion depth t_r with respect to the time of exposure under corrosion environment T_e . So from equation (2.19):

$$r_r = \frac{d(t_r)}{d(T_e)} = C_1 \cdot C_2 \cdot (T - T_t - T_c)^{C_2-1} \quad (2.20)$$

The curvature of the $t_r - T_e$ curves, is then obtained by the gradient of r_r , so from equation (2.20):

$$\frac{d^2(t_r)}{d^2(T_e)} = \frac{d(r_r)}{d(T_e)} = C_1 \cdot C_2 \cdot (C_2-1) \cdot (T - T_t - T_c)^{C_2-2} \quad (2.21)$$

From equation (2.21) it is clear that:

$$\left\{ \begin{array}{l} C_2 > 1 : \frac{d(r_r)}{d(T)} > 0 \Rightarrow t_r \text{ is convex and } r_r \text{ is an ascending function of } T \quad (2.22a) \\ 0 < C_2 < 1 : \frac{d(r_r)}{d(T)} < 0 \Rightarrow t_r \text{ is concave and } r_r \text{ is a descending function of } T \quad (2.22b) \\ C_2 = 0 \text{ or } C_2 = 1 : \frac{d(r_r)}{d(T)} = 0 \Rightarrow t_r \text{ is linear and } r_r \text{ is a constant function of } T \quad (2.22c) \end{array} \right\}$$

From equations (2.22) examining each case:

- Case (2.22a): Corrosion rate is increasing as corrosion proceeds. This type of corrosion progression may be likely to happen in dynamically loaded structures, such as ship structures where structural flexing due to wave loading continually exposes additional fresh surface to the corrosive attack
- Case (2.22b): Corrosion rate is decreasing as the corrosion progress proceeds. This is because corroded material stays on the steel surface, protecting it from contact with the corrosive environment, and the corrosion process stops. This type of corrosion progression may be typical for statically loaded structures so that relatively static corrosion scale at the steel surface can disturb the corrosion progression.
- Case (2.22c): Corrosion rate remains constant as corrosion proceeds, without any dependence of the time the material is exposed to the corrosive environment.

The above cases are shown in the following figure for several values.

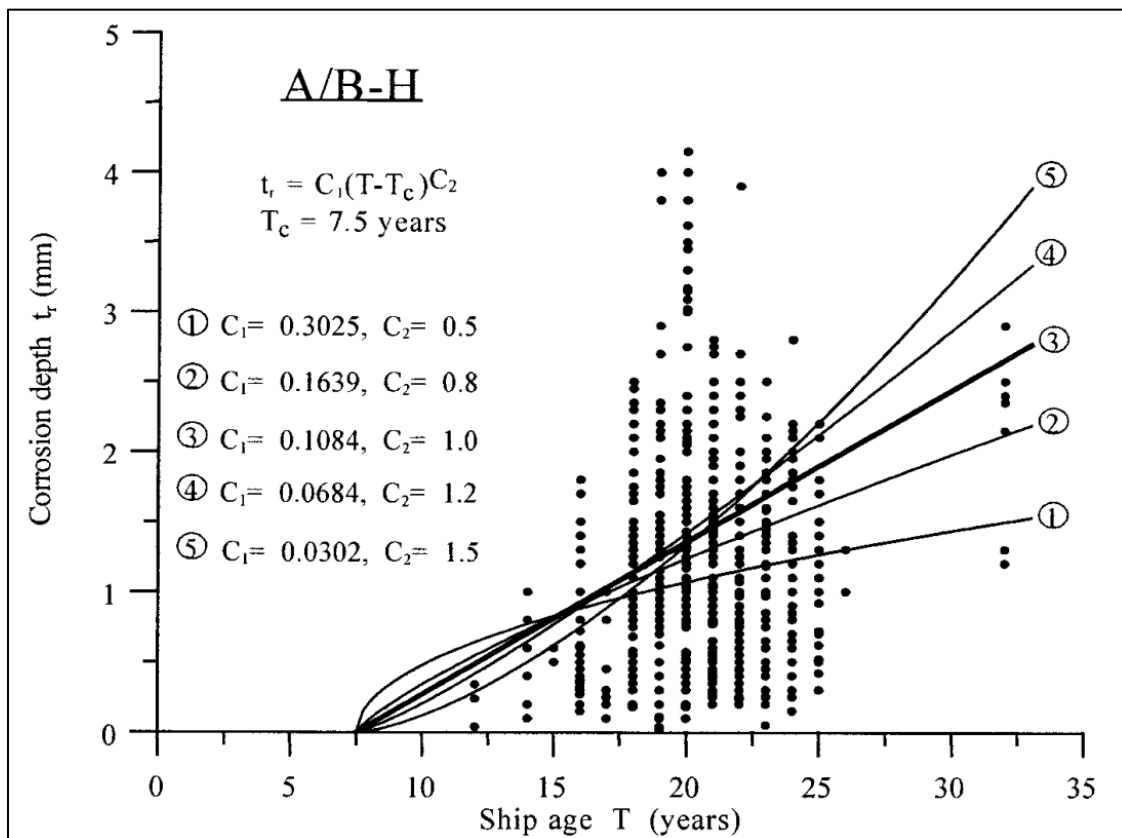


Figure 2.16.: The dependence of t_r on the values of C_1 and C_2 coefficients, shown for A/B-H plate and $T_c = 7.5$ years [15]

It is obvious from figure 2.16 that in all cases and despite the value of C_1 , as the value of C_2 increases, the curvature of the $t_r - T$ curves increases (the curves become more “convex”) and the corrosion rate becomes a more “ascending” function of time.

It is noteworthy that the dots seen in figure 2.16 correspond to the ships that were studied. In specific, each dot refers to a ship with a certain age, whose A / B - H (segregated ballast tank – see figure 2.14) plate was found with certain corrosion depth, whilst its coating life was estimated to have been 7.5 years.

The next step of the modelling procedure is to define the C_1, C_2, T_t, T_c parameters for each ship member, so that the relation $t_r - T$ can be fully defined.

At first, for practical reasons it is supposed that:

$$C_2 = 1 \quad (2.23a)$$

Then for the transition time, it is assumed that:

$$T_t = 0 \quad (2.23b)$$

Equation (2.23b) indicates that corrosion starts immediately after the breakdown of coating, which is a conservative (- worst case and therefore safest) assumption.

From equations (2.19),(2.23):

$$t_r = C_1 \cdot T_e^{C_2} \Rightarrow t_r = C_1 \cdot (T - T_c) \quad (2.24)$$

Equation (2.24) is the final expression of corrosion depth t_r as a function of the ship’s age T , with C_1 and T_c as parameters. In order to fully define equation (2.24) for a certain structural member of ship, it is necessary to determine the values of these parameters.

Since the prediction of the lifespan of the coating is not an easy task, for practical reasons, T_c is considered to vary between the following three values:

$$\left\{ \begin{array}{l} T_c = 5 \text{ years} \\ T_c = 7.5 \text{ years} \\ T_c = 10 \text{ years} \end{array} \right\} \quad (2.25)$$

From equation 2.24, C_1 can be expressed as:

$$C_1 = \frac{t_r}{(T - T_c)} \quad (2.26)$$

The aim is to estimate three values for each structural member of the coefficient C_1 , in respect to each value of T_c (equation 2.25). For this purpose, the corrosion data of each structural member of a specific vessel's is used to provide the t_r value with respect to a certain T (age of the ship that the t_r was measured). The above observations now lead to a new statistical variable, of the same sample, the one of the coefficient C_1 as it calculated from equation 2.26.

With the above data a scatter of points of calculated C_1 , each one corresponding to $[t_r, T]_i$ is created. In Paik's study, the data is used for the creation of two sample spaces. The first is consisted of the entirety of the available data whereas the second contains the 5 % of the worst cases of corrosion (in the sense of the highest values measured for t_r). According to the study [15] the scatters are approximated as follows:

- All corrosion data: the statistical distribution of C_1 follows the Weibull distribution
- Above 95% band: the statistical distribution of C_1 follows the normal distribution

The above are schematically shown for the A / B - H member (see figure 2.14 for definition) for the case of $T_c=5$ years, in the following figures 2.17 along with the mean value and the coefficient of variation (COV) of C_1 .

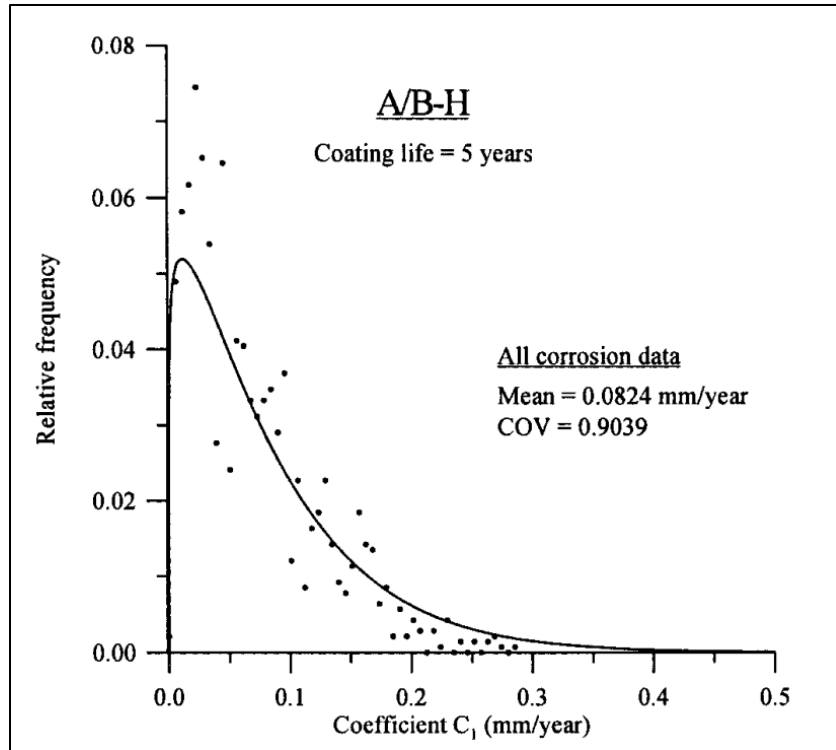


Figure 2.17a: The best fit of a Weibull distribution for the coefficient C_1 for all corrosion data shown for A/B-H plate and $T_c = 5$ years [15]

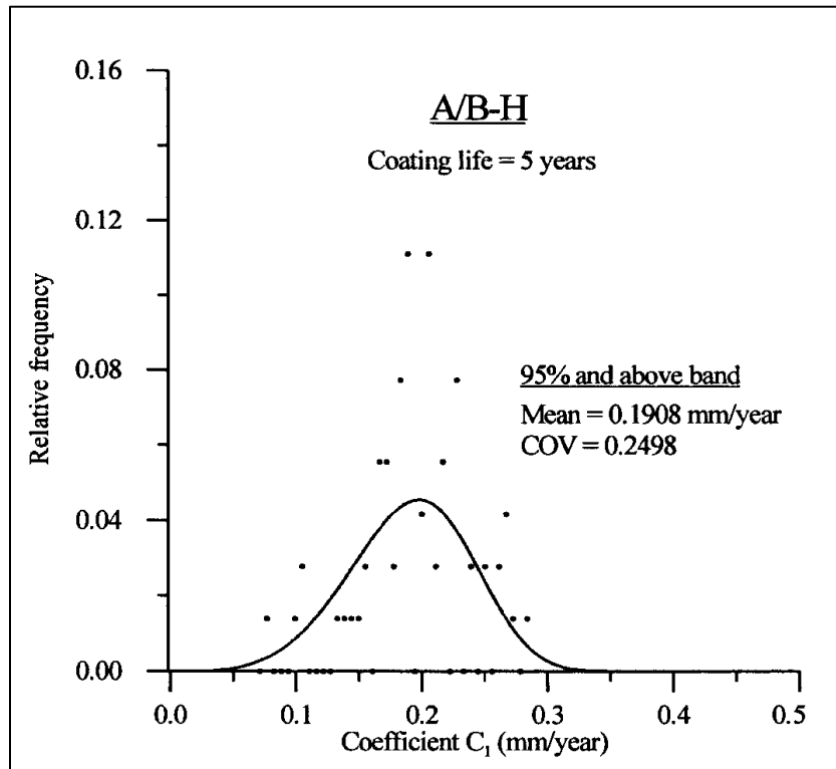


Figure 2.17b. : The best fit of a Normal distribution for the coefficient C_1 using the 95% and above band of the corrosion data shown for A/B-H plate and $T_c = 5$ years [15]

Figures similar to 2.17 are created for all three values of T_c for each part of the 34 members that corrosion data was available and so the mean value and covariance (COV) could be estimated for the annualized corrosion rate (coefficient C_1). The following table represents the final results as they were calculated for longitudinal stiffeners in single-skin tanker from [15].

Table 2.7: The results for the mean and COV of the annualized corrosion rate (coefficient C_1) for longitudinal stiffeners in single-skin tanker

ID No.	Member Group	T_c Coating Life (years)	All Corrosion Data		95% and above band	
			Mean C_1 (mm/year)	COV of C_1	Mean C_1 (mm/year)	COV of C_1
1	B/S-H	5	0.0518	0.8439	0.1483	0.2387
		7.5	0.0597	0.9901	0.1717	0.229
		10	0.0704	0.9894	0.2159	0.1974
2	A/B-H	5	0.0824	0.9039	0.1908	0.2498
		7.5	0.1084	0.8183	0.2323	0.2277
		10	0.1208	0.8922	0.3012	0.1942
3	A/B-V	5	0.0552	1.1258	0.1582	0.3227
		7.5	0.0661	1.1341	0.1897	0.3227
		10	0.0762	1.1147	0.2436	0.3207
4	B/S-V	5	0.0545	1.0033	0.1566	0.2387
		7.5	0.0622	1.003	0.1823	0.2185
		10	0.0731	1.002	0.2382	0.1942
5	BLGB	5	0.0539	0.9134	0.1525	0.3008
		7.5	0.0619	0.8821	0.1805	0.2167
		10	0.0728	0.8559	0.2371	0.2387
6	O/B-V	5	0.0792	0.8162	0.1616	0.2498
		7.5	0.1012	0.7994	0.1919	0.2277
		10	0.1184	0.8369	0.2483	0.1866
7	B/B-H	5	0.1111	0.229	0.2206	0
		7.5	0.1408	0.2704	0.2586	0
		10	0.179	0.2708	0.3125	0
8	O/S-H	5	0.0526	0.8439	0.1503	0.2601
		7.5	0.0607	0.8248	0.1777	0.2167
		10	0.0709	0.7793	0.2217	0.208
9	A/O-H	5	0.0489	0.843	0.1434	0.2495
		7.5	0.0581	0.8262	0.1689	0.229
		10	0.0682	0.824	0.2113	0.1942
10	A/O-V	5	0.0444	1.0023	0.1339	0.2601
		7.5	0.0523	1.0111	0.1529	0.2167
		10	0.0633	0.9993	0.1928	0.1942
11	O/S-V	5	0.0346	0.9134	0.1318	0.2387
		7.5	0.0423	0.7601	0.1497	0.229
		10	0.0532	0.7563	0.1841	0.1827
12	BLGC	5	0.034	1.001	0.129	0.2704
		7.5	0.0414	1.0033	0.1446	0.2167
		10	0.0513	0.9993	0.1776	0.1827

13	O/O-V	5	0.0475	0.8108	0.1406	0.2498
		7.5	0.0577	0.8162	0.1621	0.2185
		10	0.0671	0.817	0.2014	0.2055
14	O/O-H	5	0.033	1.1979	0.1251	0.2495
		7.5	0.0405	1.1341	0.1423	0.2277
		10	0.0509	1.1258	0.1727	0.208
15	BSLB(W)	5	0.1184	0.8922	0.2126	0.2495
		7.5	0.1367	0.7802	0.2461	0.229
		10	0.1613	0.9325	0.3052	0.1942
16	BSLB(F)	5	0.0976	1.1147	0.2024	0.2704
		7.5	0.1127	1.0121	0.2343	0.1827
		10	0.133	1.1433	0.2905	0.1942
17	DLB(W)	5	0.2081	1.002	0.3667	0.2498
		7.5	0.2403	0.9165	0.4244	0.1942
		10	0.2836	1.0139	0.5263	0.1974
18	SSLB(W)	5	0.1224	0.8559	0.2242	0.2601
		7.5	0.1413	1.0097	0.2595	0.1942
		10	0.1667	0.9153	0.3218	0.2387
19	SSLB(F)	5	0.0764	0.9134	0.1408	0.2495
		7.5	0.0882	0.8966	0.163	0.2167
		10	0.1041	1.0283	0.2021	0.1866
20	LBLB(W)	5	0.1697	0.7793	0.3318	0.2387
		7.5	0.196	0.9993	0.384	0.1827
		10	0.2313	0.7955	0.4762	0.1866
21	LBLB(F)	5	0.1543	0.9894	0.2985	0.2498
		7.5	0.1782	0.9941	0.3455	0.2055
		10	0.2103	1.0394	0.4284	0.1974
22	BSLC(W)	5	0.0404	0.824	0.0767	0.3227
		7.5	0.0466	1.1156	0.0888	0.2387
		10	0.055	0.9062	0.1101	0.1942
23	BSLC(F)	5	0.0378	0.9993	0.0723	0.2387
		7.5	0.0437	1.1341	0.0837	0.1866
		10	0.0516	1.0238	0.1038	0.1942
24	DLC(W)	5	0.062	0.7563	0.1082	0.3008
		7.5	0.0716	0.8902	0.1252	0.2167
		10	0.0845	0.8263	0.1552	0.1827
25	DLC(F)	5	0.0509	0.9993	0.0916	0.2601
		7.5	0.0588	1.0032	0.106	0.1866
		10	0.0694	1.0211	0.1314	0.2055
26	SSLC(W)	5	0.0364	1.0258	0.07	0.2387
		7.5	0.042	1.0517	0.081	0.2185
		10	0.0496	1.1224	0.1004	0.208
27	SSLC(F)	5	0.0344	1.0507	0.0683	0.3008
		7.5	0.0397	0.8551	0.079	0.1866
		10	0.0468	1.135	0.098	0.2055
28	LBLC(W)	5	0.0476	0.9003	0.0814	0.2498
		7.5	0.055	0.8129	0.0942	0.1758
		10	0.0649	0.9859	0.1168	0.208
29	LBLC(F)	5	0.044	1.1341	0.0796	0.2601
		7.5	0.0508	1.0012	0.0921	0.2167

		10	0.0599	1.1944	0.1142	0.1942
30	BGLC(W)	5	0.0326	1.003	0.0617	0.2495
		7.5	0.0377	0.9824	0.0714	0.2395
		10	0.0445	1.1079	0.0885	0.1866
31	BGLC(F)	5	0.0276	0.8821	0.0499	0.2387
		7.5	0.0319	0.8439	0.0578	0.229
		10	0.0376	0.9039	0.0717	0.2055
32	DGLC(W)	5	0.0413	0.9432	0.0778	0.3008
		7.5	0.0477	1.0818	0.09	0.2277
		10	0.0563	1.0071	0.1116	0.208
33	DGLC(F)	5	0.0389	0.8248	0.0745	0.2601
		7.5	0.0449	0.9533	0.0862	0.1974
		10	0.053	0.8972	0.1069	0.1942
34	SSTLC(W)	5	0.0226	1.0111	0.0378	0.2495
		7.5	0.0261	1.0926	0.0437	0.1827
		10	0.0308	1.1255	0.0542	0.1974

Considering the above analysis, the following conclusions are made:

- When the model is used to predict corrosion wastage of a certain structural member, the user can find C_1 directly from the above table (for the case of longitudinal stiffeners in single-skin tanker) and calculate the plausible corrosion damage that will have appeared in a certain amount of time, both for a normal case (using all corrosion data statistical analysis) and for a pessimistic prediction (using 95% and above band statistical analysis).
- It is found that the statistical distribution of the annualized corrosion rate at the most probable (average) level follows a Weibull function, whereas it is closer to the normal function at the upper bound (severe) level. The normal function though, is a distribution with special properties [16]. For example when a variable X of a n number of measurements follows the normal distribution so that $X \sim N(\mu, \sigma)$, then $Z = \frac{X - \mu}{\sigma/\sqrt{n}}$ follows the standard normal distribution so that $Z \sim \Phi(0,1)$. The advantage of expressing a function of the corrosion rate C_1 , in this case $Z = \frac{C_1 - \mu}{\sigma/\sqrt{n}}$ is that the standard normal distribution $\Phi(0,1)$ provides tables of the cumulative probabilities of Z being lower than certain values. This means that for $Z \sim \Phi(0,1)$ the probability $P(Z \leq z)$ where z stands for a certain value, is known (and then so does $P(Z > z)$). Of course, in this case the above mean that it is not only possible to evaluate the annualized corrosion rate (coefficient C_1) for a structural member, but also when examining the worst scenarios, it is possible to know the probability of corrosion having exceeded certain bounds.

BIBLIOGRAPHY - CHAPTER 2

- [1] Παντελής Δ. Ι., Τσιούρβα Θ., “Διάβρωση Και Προστασία Ναυπηγικών Κατασκευών” , πανεπιστημιακές εκδόσεις ΕΜΠ, Αθήνα 2012.
- [2] Παπάζογλου Β., “Ναυπηγική Τεχνολογία”, πανεπιστημιακές εκδόσεις ΕΜΠ, ΕΜΠ Αθήνα 1995.
- [3] Traka K., “Numerical simulation of electrochemical behavior for naval steel microstructure via Tafel curves extrapolation method”, Diploma Thesis for the degree of Naval Architecture and Marine Engineering, National Technical University of Athens, 2016.
- [4] Παντελής Δ.Ι , Χρυσουλάκης Γ.Δ , “Επιστήμη Και Τεχνολογία των Μεταλλικών Υλικών”, Εκδόσεις Παπασωτηρίου 2^η έκδοση , 2008.
- [5] N. Nunomura, S. Sunada, “Density Functional Theory Based Modeling of the Corrosion on Iron Surfaces”, Archives of Metallurgy and Materials Journal Volume 58, 2013.
- [6] H. Eschrig, “The Fundamentals of Density Functional Theory”, Vieweg & Teubner Verlag Publishing, Technische Universität Dresden, Dresden, Germany 1996.
- [7] Κόλλια Κ., Ηλεκτρονιακή Δομή – Κυματοσυναρτήσεις, Σημειώσεις Μαθήματος “Γενική Χημεία”, ΕΜΠ, Τμήμα Ναυπηγών Μηχανολόγων Μηχανικών, Αθήνα 2016.
- [8] Kieron Burke and friends, “The ABC of DFT”, Notes by the Burke research group, Department of Chemistry, University of California, Irvine 2007.
- [9] Milan Sinor, “The Quantum Theory”, Lecture Notes, Czech Technical University of Prague , Department of Physical Electronics, 2010
- [10] Astrid Marthinsen, Fundamentals and Applications of Density Functional Theory, Lecture, Virtual Simulation Lab Norwegian University of Science and Technology (NTNU). (<https://www.youtube.com/watch?v=SXvhDLCycxc>)
- [11] Simon J. Garrett. 2001, “Adsorption, order and coverage. Ways to define surface adlayer coverage. Chemisorption and physisorption. Reasons for ordered monolayer formation”, Lecture Notes, University of Michigan, Department of Chemistry, Michigan 2001.

(<http://www.cem.msu.edu/~cem924sg/Topic05.pdf>)

[12] Τσούβαλης Ν. , “Ψαθυρή Θραύση”, Σημειώσεις Μαθήματος “Ναυπηγική Τεχνολογία”, ΕΜΠ, Τμήμα Ναυπηγών Μηχανολόγων Μηχανικών, Αθήνα 2015.

(http://mycourses.ntua.gr/courses/NAVAL1027/document/%D0%E1%F1%EF%F5%F3%E9%DC%F3%E5%E9%F2 %C4%E9%E4%E1%F3%EA%FC%ED%F4%F9%ED/%D8%C1%C8%D5%D1%C7 %C8%D1%C1%D5%D3%C7/%D8%C1%C8%D5%D1%C7 %C8%D1%C1%D5%D3%C7_Land.pdf)

[13] C.Q. Wang a, J.J. Xiong , R.A. Shenoi , M.D. Liu , J.Z. Liu , “A modified model to depict corrosion fatigue crack growth behavior for evaluating residual lives of aluminum alloys” , International Journal of Fatigue Vol. 83, Part 2, 2016.

[14] Τσούβαλης Ν. , “Θραύση Από Κόπωση”, Σημειώσεις Μαθήματος “Ναυπηγική Τεχνολογία”, ΕΜΠ, Αθήνα 2015.

(<http://mycourses.ntua.gr/courses/NAVAL1027/document/%D0%E1%F1%EF%F5%F3%E9%DC%F3%E5%E9%F2 %C4%E9%E4%E1%F3%EA%FC%ED%F4%F9%ED/%C8%D1%C1%D5%D3%C7 %C1%D0%CF%CA%CF%D0%D9%D3%C7/%C8%F1%E1%FD%F3%E7 %E1%F0%FC %CA%FC%F0%F9%F3%E7.pdf>)

[15] Jeom Kee Paik, Jae Myung Lee, Joon Sung Hwang, Young Il Park, “A Time-Dependent Corrosion Wastage Model for the Structures of Single- and Double-Hull Tankers and FSOs and FPSOs”, Marine Technology, Vol. 40, Published by Society of Naval Architects and Marine Engineers (SNAME), 2003.

[16] Σπηλιώτης Ι., Κοκολάκης Γ., “Εισαγωγή στις Πιθανότητες”, Εκδόσεις Συμεών, ΕΜΠ Αθήνα 2002.

[17] “The Born-Oppenheimer Approximation”, Notes by Department of Physics and Astronomy of the Georgia State University, Atlanta, Georgia.

(<http://hyperphysics.phy-astr.gsu.edu/hbase/molecule/bornop.html>)

[18] C. David Sherrill, “An Introduction to Hartree-Fock Molecular Orbital Theory”, Notes , Georgia Institute of Technology, School of Chemistry and Biochemistry, Georgia 2000.

(<http://vergil.chemistry.gatech.edu/notes/hf-intro/hf-intro.pdf>)

[19] P. Hohenberg, W. Kohn, “Inhomogeneous Electron Gas”, APS journals archive, Physical Review 136, B864 University of California at San Diego, 1964.

[20] W. Kohn and L. J. Sham, “Self-Consistent Equations Including Exchange and Correlation Effects”,
APS journals archive , Physical Review 136, B864 University of California at San Diego, 1965.

CHAPTER 3 – EXPERIMENTS

3.1: Introduction

The present thesis focuses on the simulation of electrochemical behavior for naval steel microstructure, exploiting Tafel curves extrapolation method. However, for the development of the model the simulation of the ferritic, pearlitic microstructure was mandatory. Thus, for both simulations, electrochemical behavior and microstructure, the respective experimental data were necessary.

The study of the microstructure was performed for ferritic - pearlitic AH36 steel specimen, as well as for pearlitic steel specimen and for α -phase pure iron specimen; the constituting microstructures of AH36 steel. The microstructure was studied employing Optical Microscopy.

The electrochemical behavior of each of the aforementioned specimen was studied employing large signal polarization: Potentiodynamic polarization in order to obtain Tafel polarization curves ($\pm 250\text{mV}$ vs. Open Circuit). Both experimental procedures were conducted in the Shipbuilding Technology Laboratory, at School of Naval Architecture and Marine Engineering of the National Technical University of Athens employing Optical Microscopy Leica MZ6 and Potentiostat Parstat 4 by Princeton Applied Research.

3.2: Experimental procedures

Three specimens were employed for the experimental procedures: AH36 steel specimen, pure iron (Fe) specimen, pearlitic steel specimen.

In particular the specimens used were:

- Pure Iron (Fe): α -phase Ferrite (as denoted at the Fe – C equilibrium phase diagram [3]).
- Pearlitic steel specimen: consisting of iron (Fe) with 0.8% carbon (C) in the form of α - ferrite and cementite (Fe_3C) (as denoted at the Fe – C equilibrium phase diagram [3]).
- AH36 steel specimen: consisting of α -phase ferrite and pearlite micro-constituents, high strength steel (HSS) with 0.179% C and other alloying elements (see table 3.1), which is characterized as hypoeutectic steel [3].

Table 3.1: Chemical Composition of the AH36 Steel (% w/w)

C	Mn	Si	P	S	Cr	Ni	Al	Cu
0.179	1.56	0.441	0.016	0.006	0.03	0.18	0.053	0.15
Ti	N	Nb	V	Mo	Ca	Sn	B	
0.003	0.007	0.003	0.005	0.054	0.000	0.002	0.0002	

The experimental procedures were conducted as follows:

- a) The specimens were cut in the laboratory's mechanical workshop and then mounted in epoxy resin of two components.
- b) The mounted specimens were mechanically grinded, until the surface was smoothed (without irregularities). The procedure involved the rotation of abrasive papers in contact with the metallic surface, while constant water flow was provided for the cooling of the specimen and the removal of resin and metal shavings from the metallic surface. The abrasive papers used consisted of hard granules of silicon carbides (SiC). In descending order, of abrasive grains size, the papers used had a grit number of: 80, 120, 220, 320, 500, 800, 1000, 1200, 2000, 4000
- c) The grinded specimens were afterwards polished. The polishing of the metallic surface was accomplished as it was in contact with a rotating, velvet-covered disc where alumina agglomerated suspension (Al_2O_3) was poured over in two stages: At first grain size used was $1\mu m$ and then $0.1\mu m$.
- d) The metallic surface was chemically etched so that its surface structure could be identified with optical microscopy. The solution used was Nital (98% alcohol and 2% nitric acid), where the specimens were immersed for approximately 10 seconds.
- e) The specimens were observed with the use of an optical microscope
- f) The specimens were grinded again for exposure of "new drastic" surface (repetition of step b) to the electrolyte solution.
- g) The specimens were placed appropriately (the corroding surface exposed to aqueous solution H_2O of 3.5% NaCl) at the electrochemical cell (see figure 3.1) at $25\text{ }^\circ C$ temperature. The electrodes (see figure 3.1a) were connected to the potentiostat (see figure 3.1b) as recommended [6]. It is noted that the reference electrode [1] used was a saturated calomel electrode (SCE), and the counter electrode a platinum (Pt) grid.

For the determination of the electrochemical behavior under polarization, as explained in section 1.1.6, the potentiostat applies an overpotential (from equilibrium potentials of the specimens) in a certain range and measured the current flow (equation 1.7 of chapter 1). In specific, the method applied for the Tafel curves approximation (see section 3.4) was a destructive method [6] with an applied voltage of ± 0.25 V versus the equilibrium electrochemical potential.

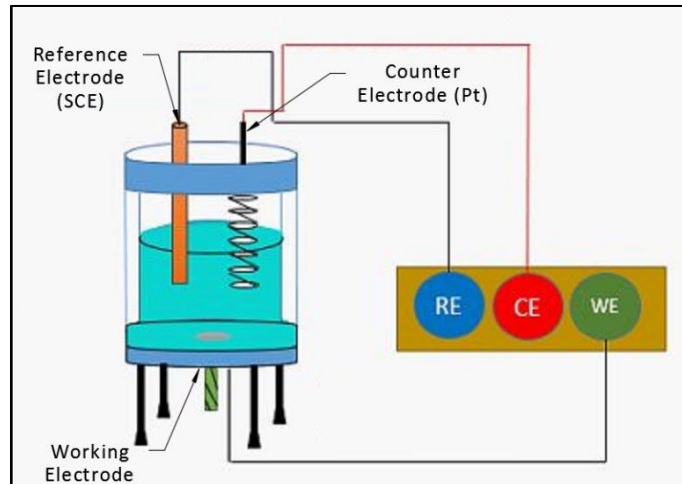


Figure 3.1a: Experimental setup for the three-electrode electrochemical cell used for the corrosion measurements [2]

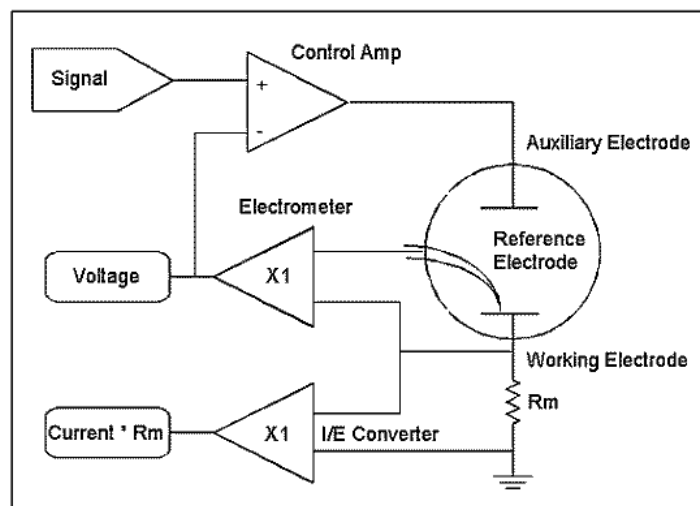


Fig.3.1b.Simple schematic of potentiostat and three electrodes electrochemical cell.

3.3: Experimental Results

The aforementioned experimental procedure (section 3.2) was applied to all specimens. The results are presented in the following paragraphs 3.3.1, 3.3.2 and 3.3.3 for ferritic specimen, pearlitic specimen and AH36 steel specimen respectively.

3.3.1 Microstructure study of specimens

a) Ferritic specimen (Pure Iron - α Phase)

The ferritic specimen was subjected to grinding, polishing and etching, as described in the previous paragraph (section 3.2), for its observation through optical microscopy. The ferritic phase is shown in figure 3.2a and figure 3.2b in different magnitude. This structure in the micrographs 3.2a and 3.2b consist of hundreds of individual ferrite grains separated by grain boundaries, shown as the dark borders of each grain. Each of these grains is a single crystal of ferrite. A grain or crystal of ferrite has a BCC crystal structure. A grain boundary separates a ferrite grain of one crystal lattice orientation from a ferrite grain of another orientation. The microstructure shown in these figures is typical of a low-carbon steel. The different in light reflection is owed to the different orientation of each grain. Additionally, the average grain size is approximated at 50-60 μm .

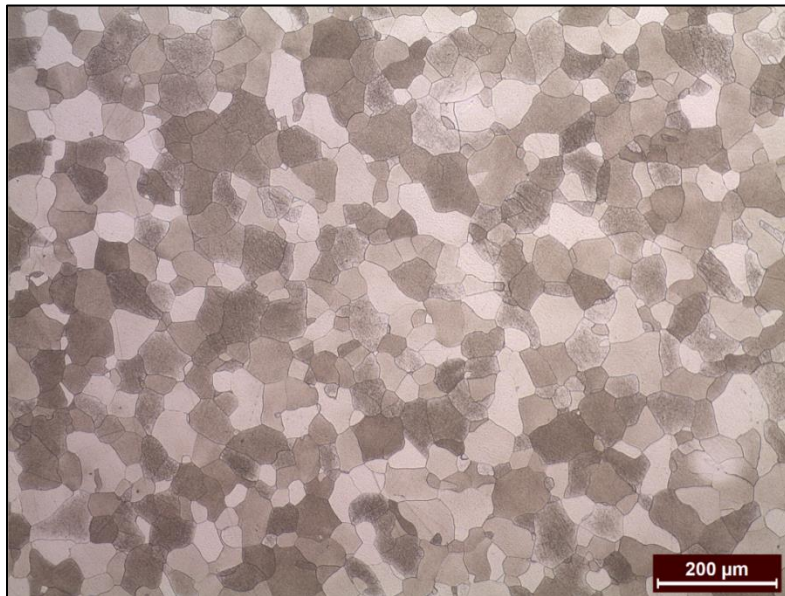


Figure 3.2a: Ferrite grains as observed via optical microscopy, Etching: Nital 2%

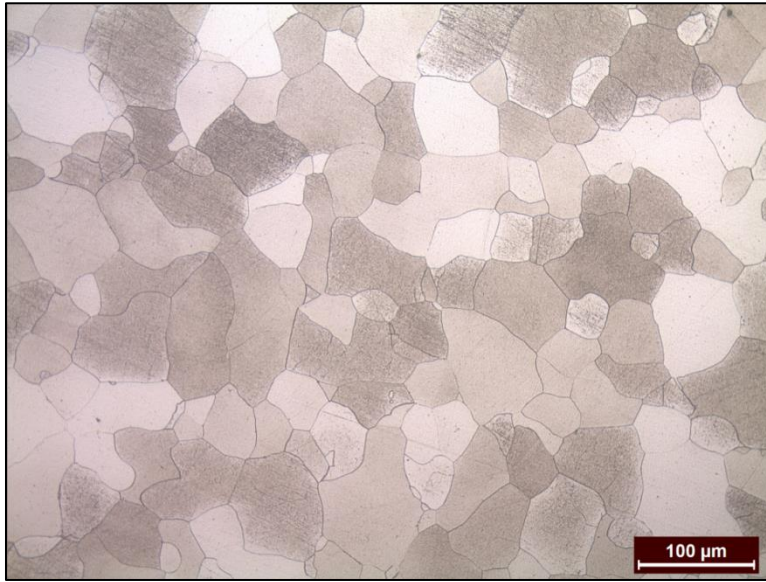


Figure 3.2b: Ferrite grains as observed via optical microscopy, Etching: Nital 2%

b) Pearlitic specimen

The 0.8% Carbon steel specimen was subjected to grinding, polishing and etching, as described in the previous paragraph (Chapter 3.2), for its observation through optical microscopy. The pearlitic microconstituents are shown in figure 3.3a and figure 3.3b in different magnitude. Pearlite is a mixture of ferrite and cementite phases. Additionally, the average grain size is approximated at 40-50 μm .



Figure 3.3a: Pearlite phases as observed via optical microscopy, Etching: Nital 2%

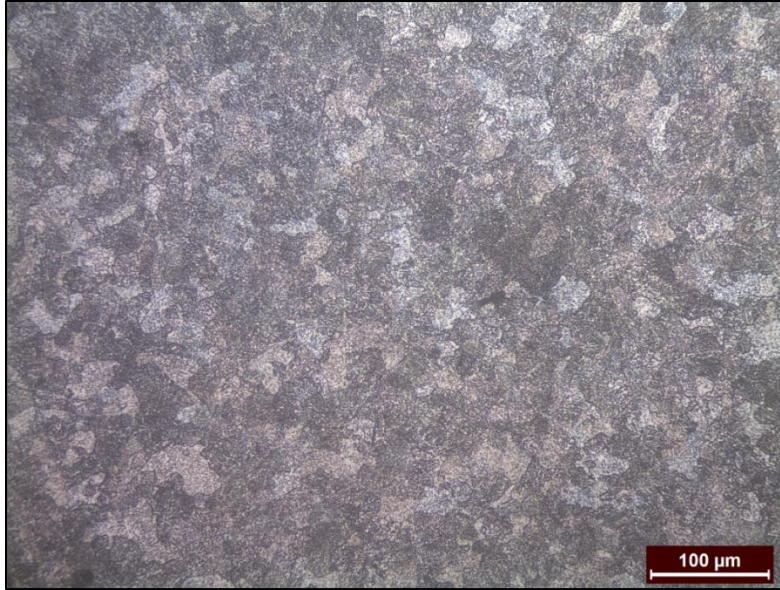


Figure 3.3b: Pearlite phases as observed via optical microscopy, Etching: Nital 2%

c) AH36 Steel specimen

The AH36 steel specimen was subjected to the grinding polishing and etching, as described in the previous paragraph (Chapter 3.2), for its observation through optical microscopy. The microstructure is shown in figure 3.4a and figure 3.4b, in different magnitude. There, the ferrite phases can be recognized by their white color in contrast to the pearlite micro-constituents which are dark colored. Additionally, rolling effect is observed in both magnitudes. This is recognized by the banded microstructure as seen in figure 3.3a and figure 3.3b.

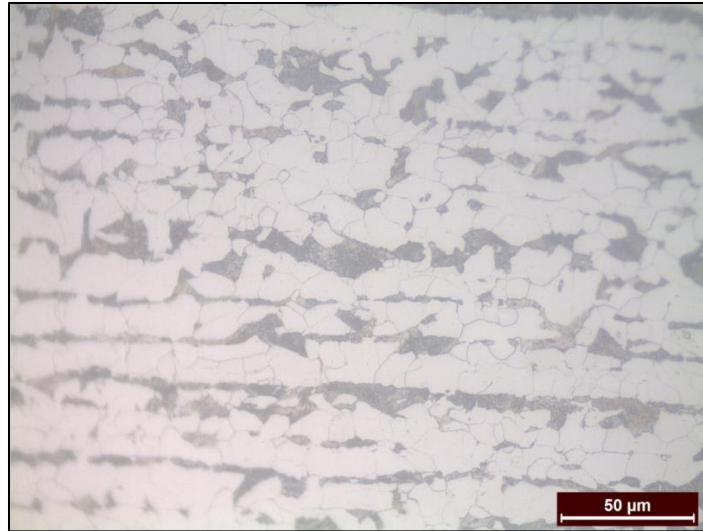


Figure 3.4a: AH36 Steel Alloy as observed via optical microscopy, Etching: Nital 2%

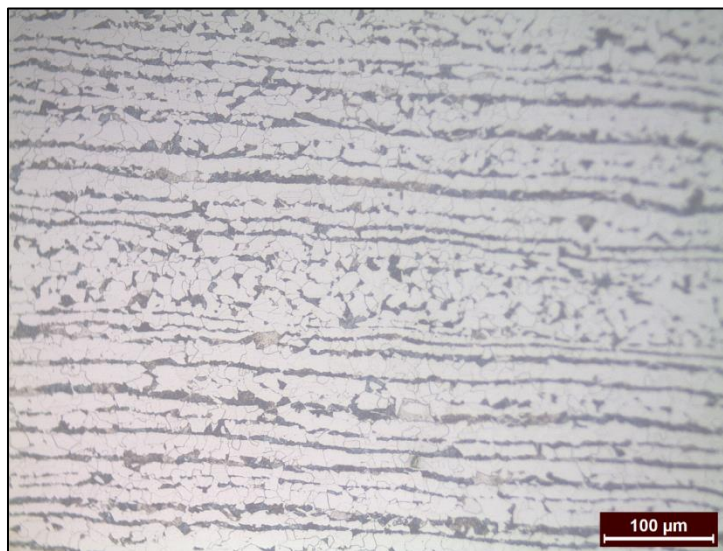


Figure 3.4b: AH36 Steel Alloy as observed via optical microscopy, Etching: Nital 2%

For the evaluation of the ferrite and pearlite portions within the AH36 steel's microstructure, a process with the use of the MIPAR software was followed. As shown in figure 3.5, during the process all pearlitic phases (black regions) were circumscribed (red outline) so that the area inside could be measured. The error of the measurements is estimated at 1.5 percent due to potential personal error caused by the uncertainty of feature rejection regarding to the grain boundaries.

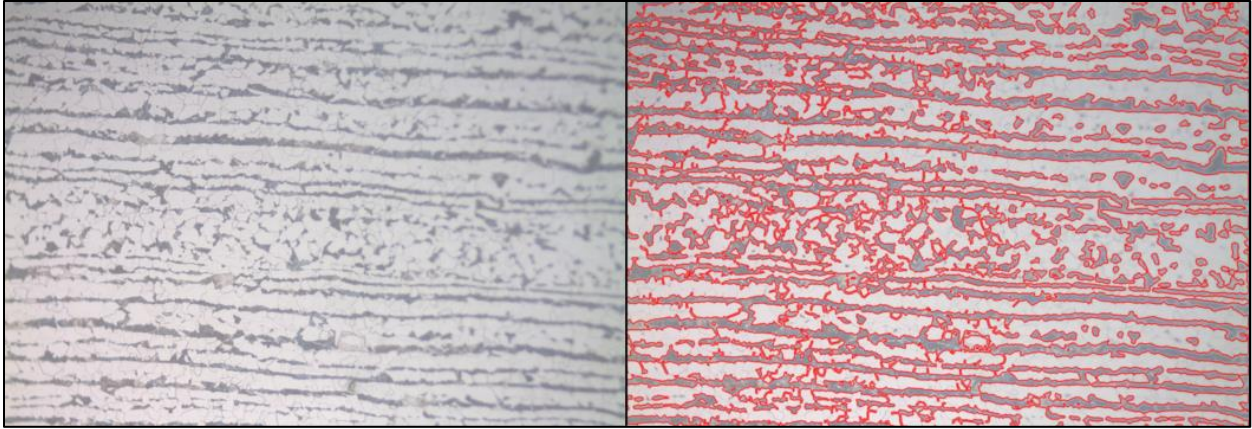


Figure 3.5: The process used on the AH36 Steel Alloy microstructure (left picture) for the pearlite and ferrite portion measurements (right picture). All pearlitic phases (black regions) are circumscribed (red outline) so that the area inside will be measured (MIPAR software)

The pearlitic area fraction was calculated as 32.2% of the total photographed (figure 3.4b or 3.5) area.

Thus, the AH36 specimen used in the experiments is constituted by:

- Pearlite: 32.2% \pm 1.5 %
- Ferrite: 67.8% \pm 1.5 %

The simulated AH36 microstructure used for the electrochemical behavior's numerical modelling, in chapter 5 will be of the same percentages with the experiment's microstructure (of the above figure 3.5).

3.3.2 Electrochemical experiments

All the three specimens were afterwards grinded again and consequently polished, in order for a uniform and electrochemically active metallic surface to be exposed to the electrolyte. The conducted electrochemical experiments regarding to this surface, provided the following current – potential curves as they are presented in the following figures 3.6, 3.7 and 3.8.

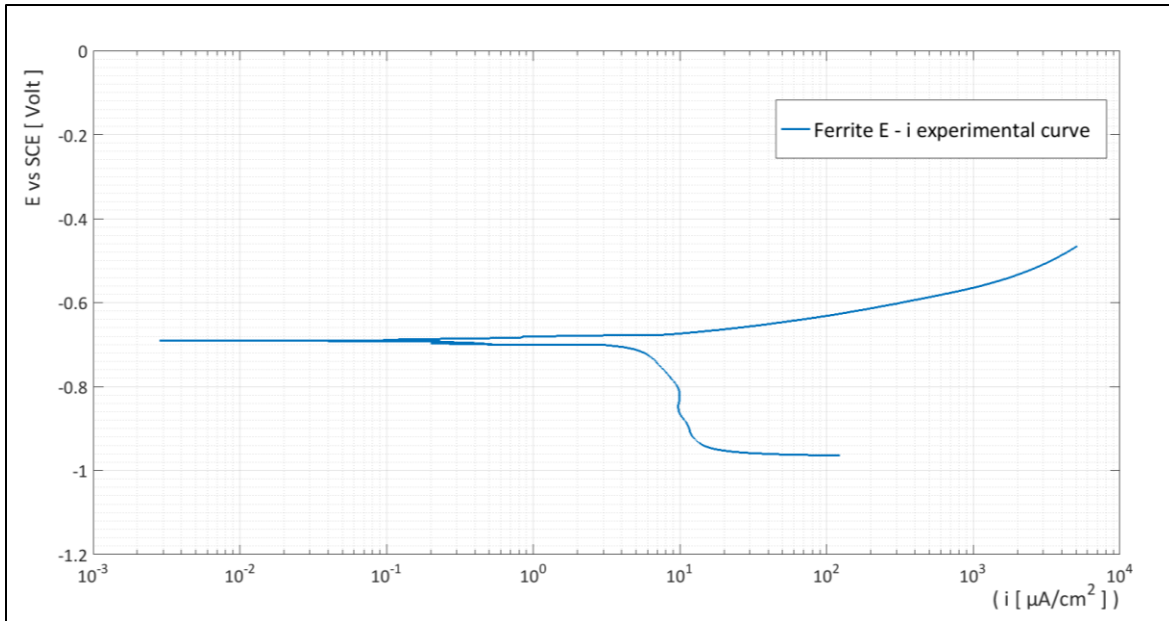


Figure 3.6: Current – potential experimental results (Tafel method) for Ferrite (α – phase pure iron specimen)

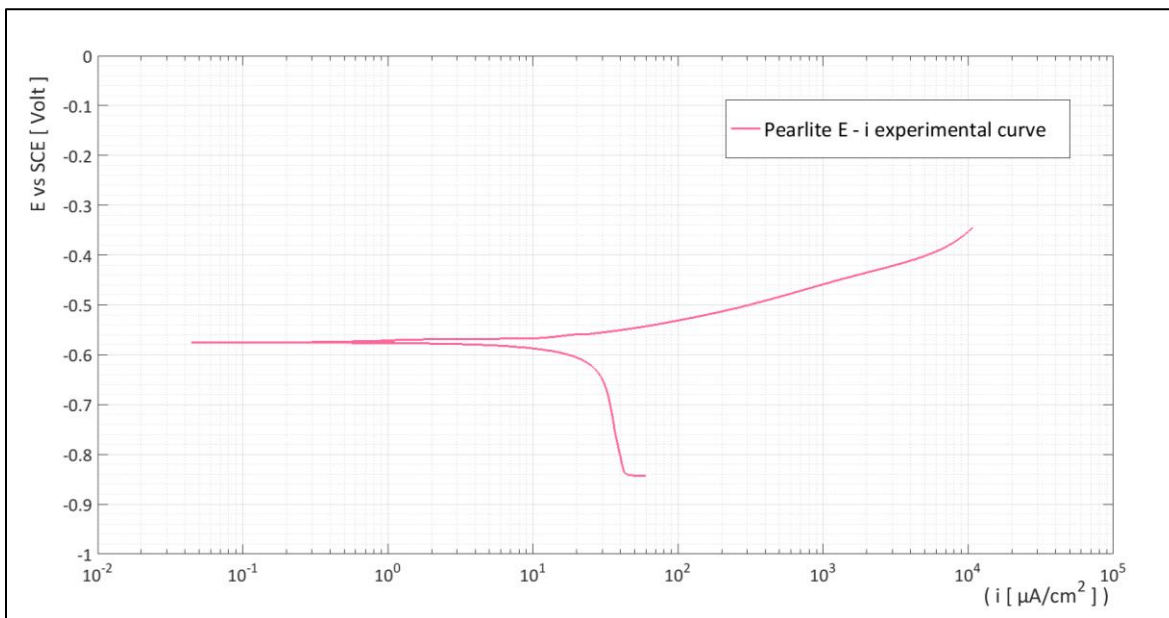


Figure 3.7: Current – potential experimental results (Tafel method) for Pearlite

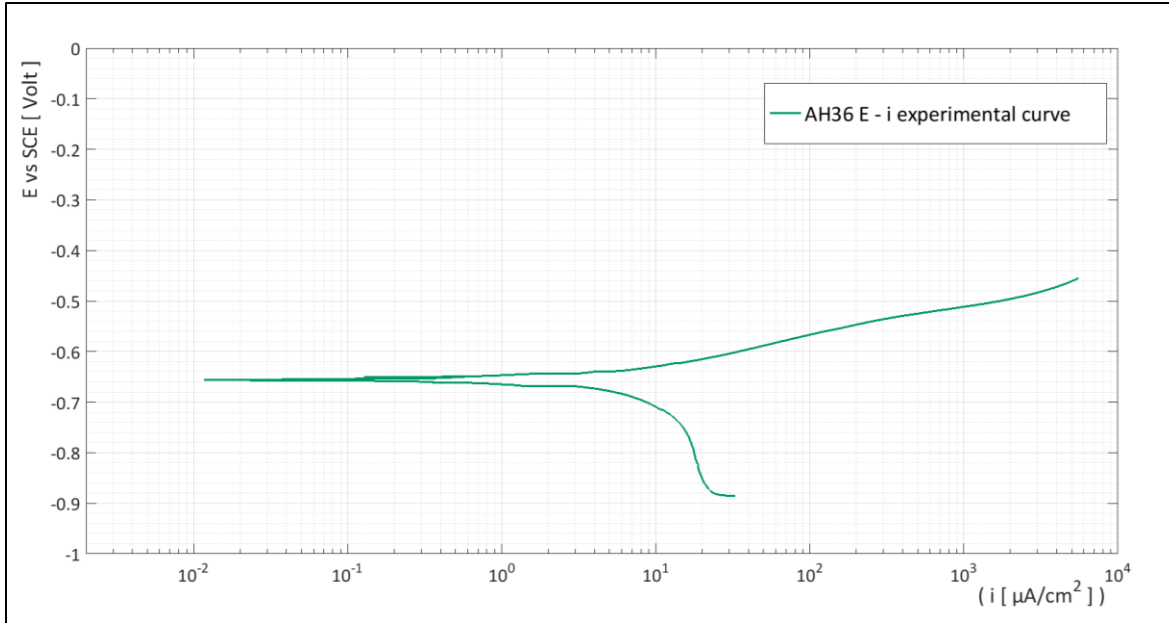


Figure 3.8: Current – potential experimental results (Tafel method) for AH36 steel alloy

From the electrochemical experiments presented in the previous graphs, the Tafel curves (figures 3.6, 3.7 and 3.8) for the ferrite, the pearlite and the AH36 specimens could be used to evaluate the electrochemical parameters of each specimen. In specific, the evaluated parameters were:

- The system's equilibrium (-corrosion) potential E_{CORR} as defined in section 1.1.4.
- The exchange current density i_{CORR} (-current density at E_{CORR}) as defined in section 1.1.6.
- The Tafel slopes β_{α} , β_{c} as defined in section 1.1.6.1.

The aim was to estimate the Tafel slopes firstly, since the point at which the theoretical Tafel curves (section 1.1.6 equations 1.16) intersect, provides the values for $(i_{\text{CORR}}, E_{\text{CORR}})$ according to [1].

The method applied was the mathematical determination of the most appropriate part (and then the best fitting line) of the experimental Tafel curves (figures 3.1c and 3.2c) that could be approximated with the theoretical Tafel equations (section 1.1.6 equations 1.16). The implementation of the method required the development of matlab codes (see annex 2 – codes 1-3).

More specifically, the experimental data of figures 3.1c and 3.2c were imported on matlab as:

$$(x_i, y_i) = (i_i, E_i).$$

Then for a varying number “N” representing the range of points, the best fitting line was calculated for a varying position “m” of the range “N”. For instance, when choosing to study N=250 out of 500 points of experimental data, the data for which the best line was calculated were:

- Point 1 to point 251 for position m=1
- Point 2 to point 252 for position m=2
- Point 3 to point 253 for position m=3
-
- Point 250 to point 500 for position m=250=N

For every selection of the values N and m (range and position of range among all data), the best fitting line was calculated by the following method:

$$\left\{ \begin{array}{l} \frac{\partial S}{\partial a} = 0 \\ \frac{\partial S}{\partial b} = 0 \end{array} \right\} \Rightarrow a, b \text{ gives the least } S = \sum_i^N (y_i - a x_i + b)^2 / N \text{ among all other possible } a, b$$

Where:

- a is the slope
- b is the intersection of the line with the x'x axis
- S is the dispersion between the line $y = a x + b$ and the experimental data of range N and position m.

For the determination of the range N, and position m whose best fitting line could represent all the experimental data (of the anodic or the cathodic part) the dispersions would then be compared among all best fitting lines' dispersions.

Apart from the above dispersion S, for every $y = a x + b$ calculated before and corresponding to a certain N, m couple, the dispersion from all the experimental data was also calculated with the following formula:

$$S_{\text{all data}} = \sum_j^{N_a} (y_j - a x_j + b)^2 / N_a$$

Where:

- N_a is the range (-number) of all the experimental data (anodic or cathodic)

Up to this point several best fitting lines had been calculated, each one corresponding to a certain

$N, m, S, S_{\text{all data}}$

For both the anodic and the cathodic polarization data, it was assumed that the Tafel curve in each part would be the one with the smallest dispersion from them, as defined from the following formula:

$$S_{\text{final}}(N,m) = S + S_{\text{all data}} = 0.5 \cdot \sum_i^N (y_i - a x_i + b)^2 / N + 0.5 \cdot \sum_j^{N_a} (y_j - a x_j + b)^2 / N_a \quad (3.1)$$

Equation 3.1 implies that for the determination of the part of the experimental data that would be better represented with a linear approximation of Tafel curve (anodic or cathodic), apart from the deviation from the data belonging to the part itself, the Tafel line would have to present small deviation from all the experimental data as well. The two dispersions (as seen in equation 3.1) were selected to be equally taken into consideration, and thus their weight coefficients were set to 0.5 (as seen in equation 3.1).

After obtaining the a, b and $S_{\text{final}}(N,m)$ for each of the studied range (N,m) , these would be compared regarding to the value of dispersion $S_{\text{final}}(N,m)$. The selected range (N,m) was the one giving the least value of S_{final} . According to the above analysis, the optimization made, was the selection of two parameters (N, m) , the position m and the number of the data N , for which the best fitting line would minimize the dispersion (S_{final}).

The final optimization was made, through the matlab codes (see annex 2 – codes 1-3) for the ferrite, pearlite, and AH36 experimental data of figures 3.6, 3.7 and 3.8 respectively.

It should be noted that this optimization provides values for $(i_{\text{corr}}, E_{\text{corr}})$ as the intersection point of the extrapolated Tafel curves. Therefore, it does not take into consideration the open circuit potential E_{ocp} (measured from the potentiostat). However, the method presupposes that when applied to potential – current data, the resulting value of E_{corr} will not deviate more than 10 mV from the respective E_{ocp} , as also stated at [5].

a) Ferrite (α – phase pure iron specimen) in 3.5% NaCl solution : Tafel curves

The most appropriate extrapolation of the anodic and the cathodic experimental data, for the Tafel curves, according to the procedure explained above (annex 2 – codes 1-3), is shown in the following figure 3.9 for the system of Ferrite (α –phase pure iron specimen) – Aqueous Solution of 3.5% NaCl.

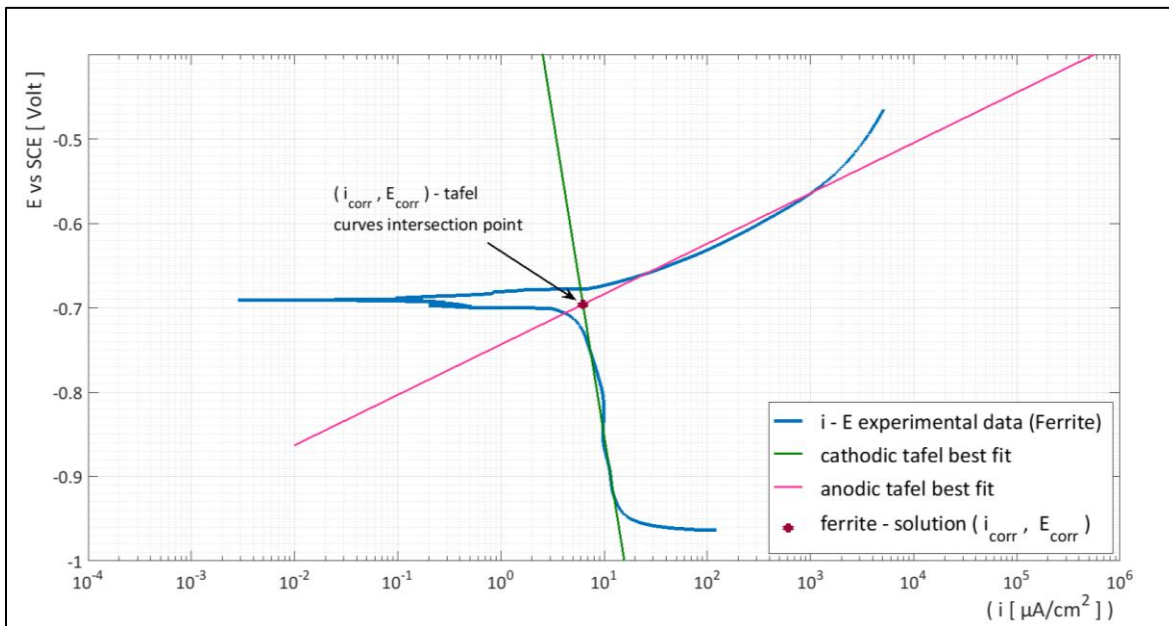


Figure 3.9: Matlab codes results for the best fit of Tafel curves on the experimental potential - current data of Ferrite – Solution

The values for the electrochemical parameters obtained, corresponding to figure 3.9, are shown in the following table 3.2a.

Table 3.2a: Electrochemical results for the system of Ferrite – (H ₂ O+3.5% NaCl)		
Electrochemical term	Obtained Value	Units
Anodic Tafel slope (Ferrite oxidation) β_{α}	0.0597	Volts
Cathodic Tafel slope (Solution reduction) β_c	-0.7589	Volts
Anodic Tafel fit line Dispersion S_{final}	$5.1286 \cdot 10^{-4}$	Volts
Cathodic Tafel fit line Dispersion S_{final}	$2.9314 \cdot 10^{-4}$	Volts
i_{corr}	6.243	$\mu\text{A}/\text{cm}^2$
E_{corr}	-0.6960	Volts

b) Pearlite in 3.5% NaCl solution : Tafel curves

The most appropriate extrapolation of the anodic and the cathodic experimental data, for the Tafel curves, according to the procedure explained above (annex 2 – codes 1-3), is shown in the following figure 3.10 for the system of Pearlite – Aqueous Solution of 3.5% NaCl.

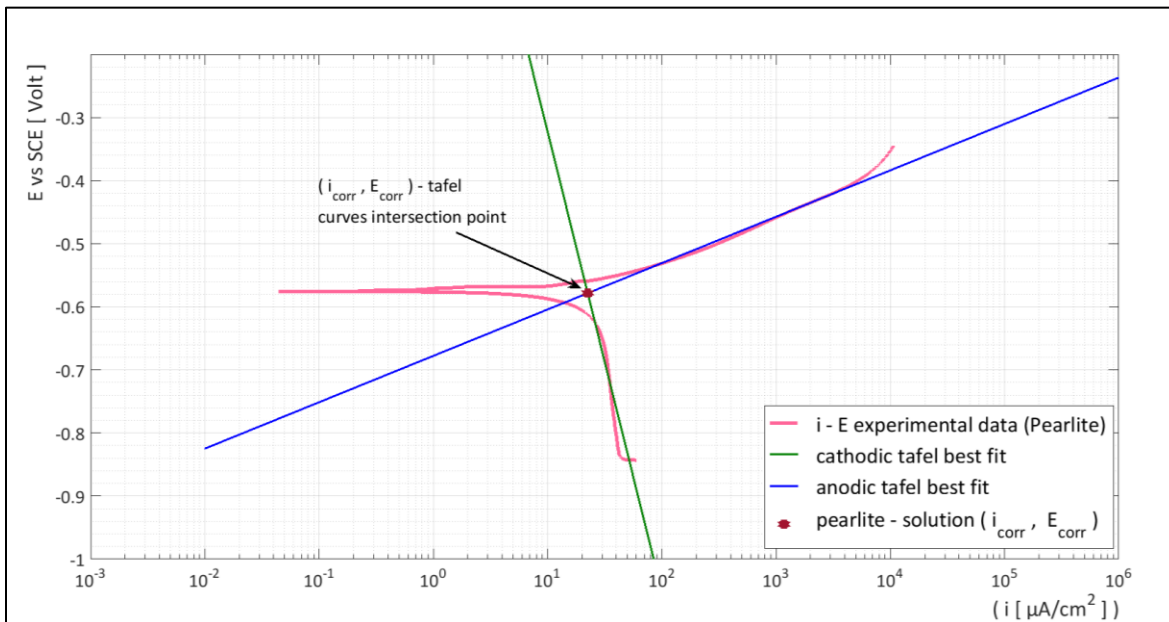


Figure 3.10: Matlab codes results for the best fit of Tafel curves on the experimental potential - current data of Pearlite – Solution

The values for the electrochemical parameters obtained, corresponding to figure 3.10, are shown in the following table 3.2b.

Electrochemical term	Obtained Value	Units
Anodic Tafel slope (Pearlite oxidation) β_{α}	0.07351	Volts
Cathodic Tafel slope (Solution reduction) β_c	-0.7295	Volts
Anodic Tafel fit line Dispersion S_{final}	$1.3861 \cdot 10^{-4}$	Volts
Cathodic Tafel fit line Dispersion S_{final}	$7.5235 \cdot 10^{-4}$	Volts
i_{corr}	22.462	$\mu\text{A}/\text{cm}^2$
E_{corr}	-0.5785	Volts

c) AH36 in 3.5% NaCl solution : Tafel curves

The extrapolation method, according to the procedure explained above (annex 2 – codes 1-3), was applied for the system of AH36 - Aqueous Solution of 3.5% NaCl.

The study of AH36 curves shows that the anodic branch exhibits Tafel behavior, adequate linearity, while the cathodic part shows that the cathodic reaction is controlled by the slower reaction: the oxygen diffusion, exhibiting clear limiting diffusion current $i_L = 21\mu\text{A}/\text{cm}^2$.

The extrapolation of the cathodic branch (oxygen diffusion) and the extrapolation of the anodic part back to E_{corr} , result to considerable (for the present study) difference for the value of i_{corr} : $5\mu\text{A}/\text{cm}^2$ (anodic branch extrapolation), $12\mu\text{A}/\text{cm}^2$ for the cathodic branch.

Thus, in order for the best extrapolation of the polarization curves, the value of R_p (polarization resistance), from EIS measurements in AH36 in the same solution was taken into account [5]. Consequently this value was applied in the following Stern Geary equation in order to determine the appropriate value for i_{corr} [5]:

$$i_{corr} = \frac{1}{2.303 \cdot R_p \cdot \left(\frac{1}{\beta_{\alpha}} + \frac{1}{|\beta_c|} \right)} \quad (3.2)$$

Where:

- R_p : the resistance measures through impedance, here set to be 1000Ω
- β_α, β_c : from table 3.2c in mV

The value for i_{corr} was calculated at $13,56 \mu\text{A}/\text{cm}^2$.

It should also be noted that in order for the cathodic Tafel curve to fit the part representing the oxygen reaction's (only) potential – current data, another modification was made, concerning the dispersion of it. In specific, the dispersion $S_{\text{final}}(N,m)$ for all N,m (as they were defined previously) was taken equal to the dispersion between the best fit line and the data it derived from (dispersion S as defined previously).

The most appropriate extrapolation of the anodic and the cathodic experimental data, for the Tafel curves, and the $(i_{\text{corr}}, E_{\text{corr}})$ are shown in the following figure 3.11 and table 3.2c for the system of AH36 – Aqueous Solution of 3.5% NaCl.

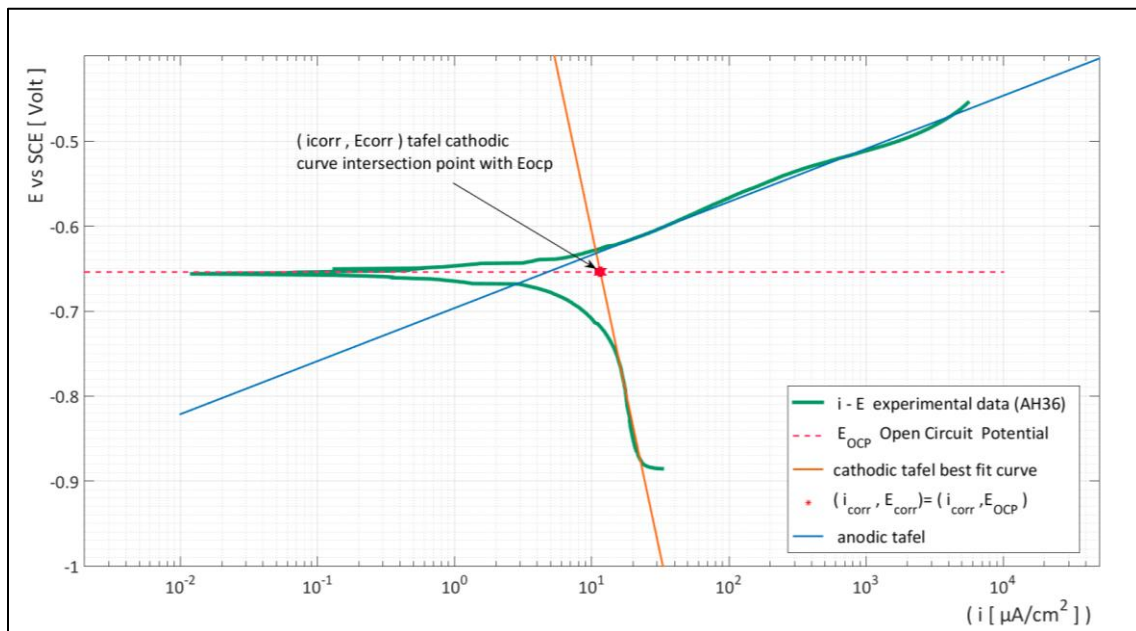


Figure 3.11: Matlab codes results for the best fit of Tafel curves on the experimental potential - current Data of AH36 – solution

The values for the electrochemical parameters obtained, corresponding to figure 3.11, are shown in the following table 3.2c.

Electrochemical term	Obtained Value	Units
Anodic Tafel slope (Pearlite oxidation), β_{α}	0.06466	Volts
Cathodic Tafel slope (Solution reduction), β_{c}	-0.7590	Volts
Anodic Tafel fit line Dispersion S_{final}	$7.86727 \cdot 10^{-6}$	Volts
Cathodic Tafel fit line Dispersion S_{final}	$8.482434 \cdot 10^{-8}$	Volts
i_{corr}	11.5275	$\mu\text{A}/\text{cm}^2$
E_{corr}	-0.6541	Volts

3.5: Results and Discussion

From figures 3.9 and 3.10 it is noticeable how Ferrite and Pearlite behave differently within the same corrosive environment (Aqueous Solution of 3.5% NaCl). This difference in electrochemical behavior can be observed with clarity in the following figure (figure 3.12).

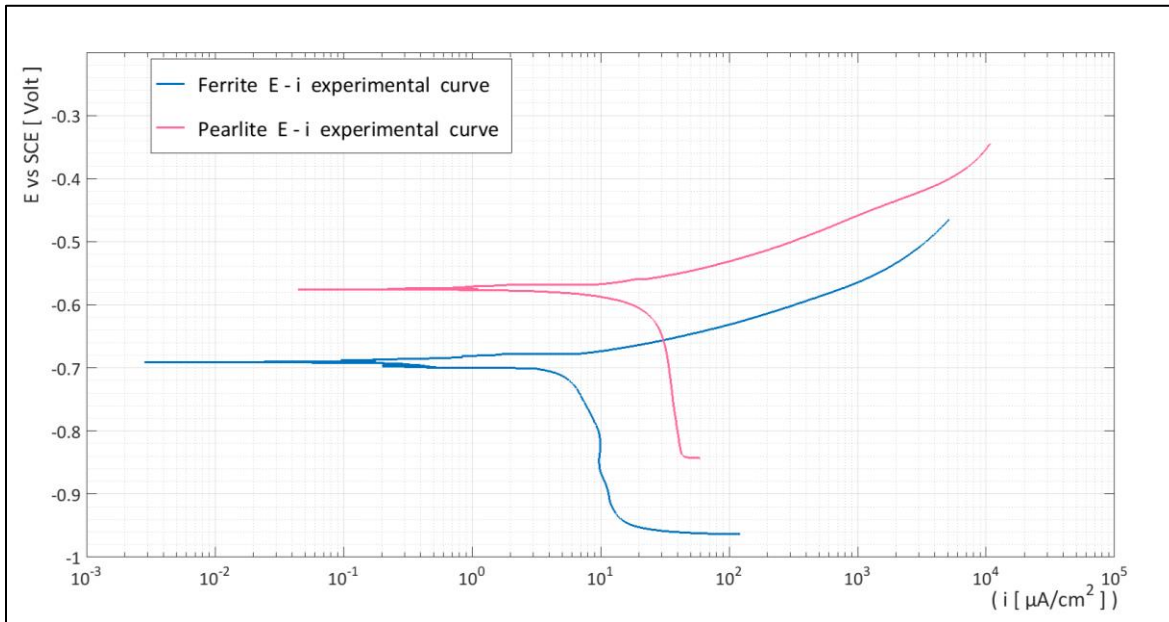


Figure 3.12: Comparison of Current – potential experimental results (Tafel method) for Ferrite and Pearlite

Electrochemical term	Ferrite (table 3.2a)	Pearlite (table 3.2b)
i_{corr} [$\mu\text{A}/\text{cm}^2$]	6.243	22.462
E_{corr} Volts	-0.6960	-0.5785

Figure 3.12 and Table 3.3 show that E_{corr} for Ferrite presents lower values than Pearlite indicating that ferrite exhibits higher tendency for corrosion. Concerning the i_{corr} values, which represent the corrosion rate, Pearlite is noticed to have higher values compared to ferrite, thus indicating higher corrosion rates. Moreover, the cathodic part of both curves shows that the reduction of oxygen is prevailing in the cathodic reactions, thus the cathodic process is controlled by concentration polarization rather than activation polarization.

The difference between the electrochemical kinetics of ferrite and pearlite (figure 3.12) within the same solution implies that it would be possible for a galvanic couple to be formed at the microstructural level. More specifically, in ferrite – pearlite steel alloys exposed to corrosion, the ferrite grains could act as the anodic counterpart, providing electrons towards the pearlitic regions (acting as the cathodes). Thus, despite pearlites higher corrosion rate (i_{corr}), a potential formation of galvanic couple between the pearlite and ferrite, would cause a level of protection on Pearlite and a higher level of corrosion on Ferrite, compared to their respective behaviors if they were uncoupled.

Such phenomena could eventually alter the type of corrosion to a more selective degradation (pitting corrosion, selective attack etc.)

In the following figure 3.13, the three specimens' Current – Potential experimental data are presented in the same plot.

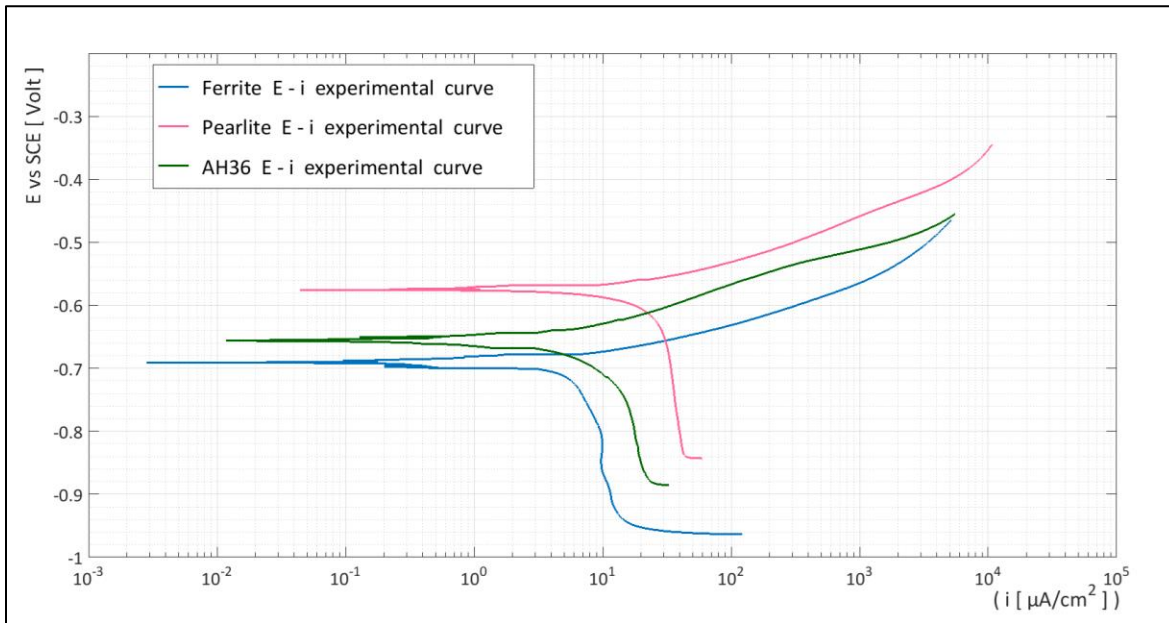


Figure 3.13: Current – potential experimental results (Tafel method) for Ferrite, Pearlite and AH36

Table 3.3b: Comparison of Electrochemical parameters for the specimens			
Electrochemical term	Ferrite (table 3.2a)	Pearlite (table 3.2b)	AH36 (table 3.2c)
i_{corr} [$\mu\text{A}/\text{cm}^2$]	6.243	22.462	11.5275
E_{corr} Volts	-0.6960	-0.5785	-0.6541

Concerning the AH36 specimen's electrochemical results, it is noticed that the developing behavior throughout all the applied potential values, remains in-between the values of its consisting metallurgical phases (Ferrite and Pearlite). In specific, the values of the polarization curves (of figure 3.13) show that AH36 steel is between Ferrite's and Pearlite's respective curves, but favored (closer to) of the Ferrite's behavior. The same applies for the values of corrosion potential E_{corr} . Approximating AH36 steel's E_{corr} in regard to the E_{corr} of Ferrite and Pearlite (values from table 3.3b) the obtained results show that AH36 steel E_{corr} is calculated as the summation of 64.5 % of Ferrite's E_{corr} and 35.5% of Pearlite's E_{corr} .

The above results lead to the assumption that the electrochemical behavior of steel seems to depend on its separate metallurgical phase (e.g. ferrite or pearlite) and their respective amount (percentages). Thus, the amount of each phase and its electrochemical behavior could be useful for the prediction of the alloy's corrosion kinetics.

BIBLIOGRAPHY - CHAPTER 3

- [1] Παντελής Δ.Ι., Τσιούρβα Θ., “Διάβρωση Και Προστασία Ναυπηγικών Κατασκευών”, Πανεπιστημιακές Εκδόσεις ΕΜΠ, Αθήνα 2012.
- [2] Traka K., “Numerical simulation of electrochemical behavior for naval steel microstructure via Tafel curves extrapolation method”, Diploma Thesis for the degree of Naval Architecture and Marine Engineering, National Technical University of Athens, 2016.
- [3] Παντελής Δ.Ι , Χρυσουλάκης Γ.Δ , “Επιστήμη Και Τεχνολογία των Μεταλλικών Υλικών”, Εκδόσεις Παπασωτηρίου 2^η έκδοση , Αθήνα, 2008.
- [4] “Basics of Corrosion Measurements”, Application Note Corr- 1, EG&G Princeton applied research, Princeton University, NJ, 1985.
(http://www.ameteki.com/media/ameteki/download_links/documentations/library/princetonapp liedresearch/application_note_corr-1.pdf?la=en)
- [5] E. McCafferty, "Validation of corrosion rates measured by the Tafel extrapolation method", Corrosion Science Journal, Volume 47, Issue 12, Pages 3202-3215, December 2005

CHAPTER 4 – SIMULATION OF FERRITIC AND PEARLITIC GRAIN MICROSTRUCTURES

4.1: Introduction

Since the modeling of the electrochemical behavior of ferritic - pearlitic AH36 steel will take into account the microstructure, the simulation of the microstructure was prerequisite. Thus, in order to develop a generic model, the effects of the rolling procedure were neglected, though the amount of ferrite phase and perlite micro-constituent in the ferritic-pearlitic AH36 steel was taken into account.

In specific, the model was applied on a G11 low carbon steel, consisting of ferritic phase and pearlitic micro-constituents, with the same amounts of ferrite phase and perlite micro-constituent and the similar grain size in its metallic matrix as AH36 steel.

The application of numerical simulations on certain processes requires the representation of the geometry on which the studied phenomena are developed. The geometry can be of any scale depending on the level of approach. In the present work the desired geometry that will be developed regards to the microscale approach of carbon steel. The aim is to accurately simulate the grain structure of such alloys.

Similar applications can be done, on microstructures which consist of ferrite and pearlite. Such microstructures can be found in a variety of steels. As denoted from the iron – carbon equilibrium phase diagram (consider adequately slow cooling) both ferrite and pearlite occur when the carbon percentage is less than 0.8% in environmental conditions, abbreviated as hypo-eutectoid steels [1].

Because polycrystalline material structure is composed of an enormous number of grains, its properties and performance are determined not only by characteristics of individual grains but also by the connectivity and interaction between them [8]. Therefore, the distribution of the grains in the alloy, was chosen to be simulated by a mathematical discretization pattern [11].

During the past decades the Voronoi diagram has been extensively used, as a tool to represent polycrystalline material's structures [3]. This technique was proposed and introduced by Meijering [7], and will accordingly be implemented within the present thesis similar to [11] simulation.

4.2: Voronoi Tessellation

4.2.1: Voronoi Diagram Definition

The Voronoi Tessellation (Dirichlet tessellation): Given a finite set of points, $P \subset \mathbb{R}^2$, it is the partitioning of the 2-D plane into convex polygons such that each polygon contains exactly one generating point (of the set of P) and every point inside a polygon is closer to its generating point than to any other. Every Voronoi diagram contains the following [2], [5]:

- Sites: The initial set of points P for which the Voronoi diagram is generated (black points in figure 4.1)
- Voronoi Cells: The generated polygons discretizing space into territories (every differently colored region in figure 4.1 is a voronoi cell).
- Voronoi edges: The edges of the generated polygons. Every voronoi edge is perpendicularly bisecting the lines connecting each two sites.
- Voronoi vertices: The vertices of the generated polygons. Every voronoi vertex is the center of the circumscribed circle of a triangle that connects three sites (see figure 4.3 where the green circle is centered at a voronoi vertex).

The voronoi tessellation is constituted of polygons whose edges are perpendicularly bisecting the lines connecting each two sites (initial points) in vicinity. As it can be seen in figure 4.1, every two adjacent sites (black dots) are equidistant from the voronoi edge between them (black lines in figure 4.1).

Figure 4.1 below shows the voronoi diagram generated for a randomly selected set of points, on 2D space (the Cartesian coordinate system). The diagram was produced with the use a matlab code (see annex 1 – code 3) for points randomly generated and stored in the software's workspace.

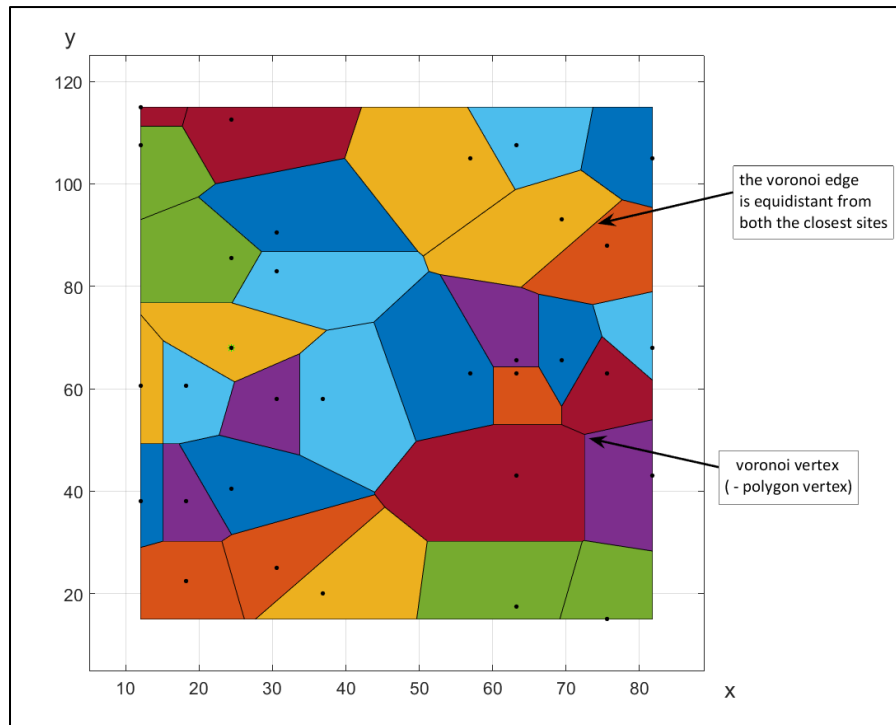


Figure 4.1: The Voronoi diagram on the Cartesian coordinate system generated with a matlab code for an initial set of points (black dots)

4.2.2: Delaunay triangulation

2-D Delaunay triangulation: Given a finite set of points, $S \subset \mathbb{R}^2$, in the 2-D plane, it is the triangulation such that the circumcircle associated with each triangle connecting three adjacent points of the initial set, contains no other point of the initial set of points S [2], [6], [10].

As it is shown in figure 4.2, the Delaunay triangulation is a unique division of the 2-D space, for a unique set of points. In particular, each triangle (red lined triangles connecting three blue dots in figure 4.2) has its circumcircle containing no other initial points (blue dots) inside.

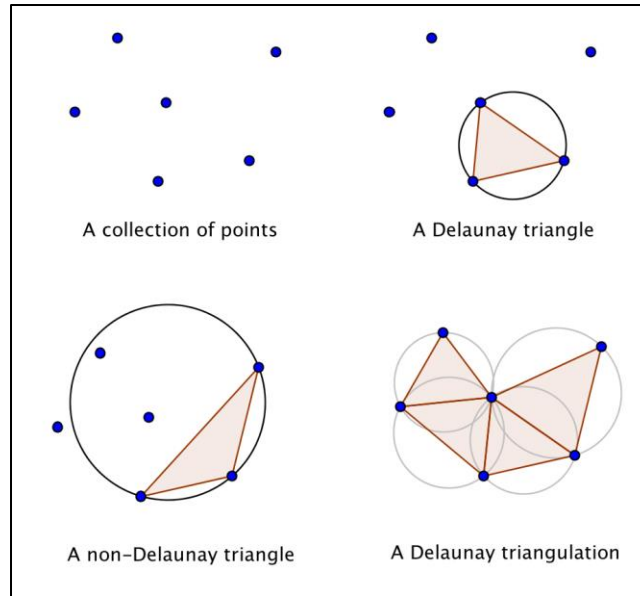


Figure 4.2: The Delaunay triangulation for a collection of points (blue dots) [10]

4.2.3: Voronoi Tessellation - Delaunay triangulation dependence

The Delaunay triangulation and Voronoi diagram in R^2 are dual to each other [2], [9]. The Delaunay triangulation and the Voronoi tessellation of a set of points have bijective correspondence. Every Voronoi edge (black lines in figure 4.3), is the perpendicular bisector line for a Delaunay's triangle edge (grey lines in figure 4.3). The duality of Delaunay triangulation and Voronoi diagram in R^2 for the same set of points is shown in figure 4.3 below.

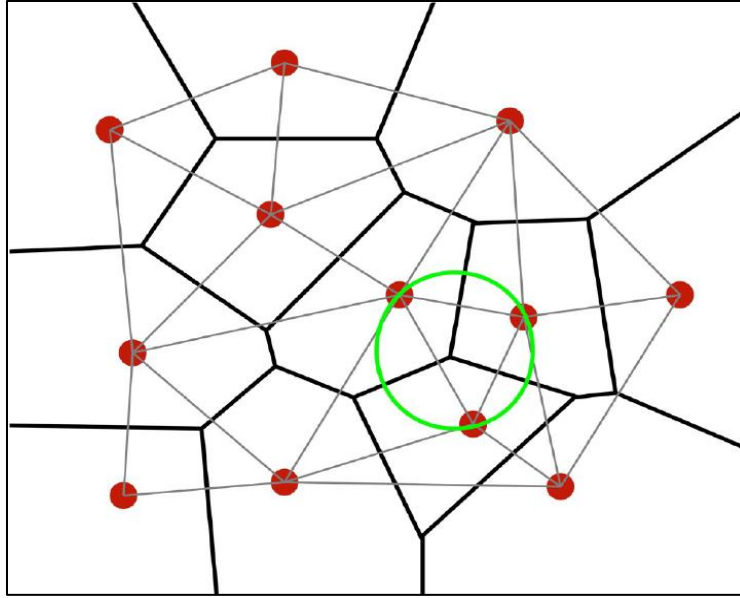


Figure 4.3: The duality of the Delaunay triangulation (grey lines) and the voronoi diagram (black lines) of a set of points (red dots). The green circle marks the circumscribed circle of a triangle in the Delaunay triangulation centered at a vertex of the Voronoi diagram [2]

4.3 – Microstructure Simulation – Application on G11 Steel

4.3.1: Model Description

This section regards to the simulation of grain distribution of low carbon steel alloys (ferritic-pearlitic). The model developed (annex 1 – codes 1-4) can represent any grain distribution with the use of Voronoi Tessellation (see section 4.2).

The model constitutes of four matlab codes (annex 1- codes 1-4), from which the main code is code number one, while the others are functions called upon the execution of the first code. These codes can be used for the production of any two phased microstructure simulation, where grains can be represented as voronoi cells. The input parameters for any application of the aforementioned codes, are the spatial coordinates of voronoi sites. These should be predetermined from the user of the model, preferably with the use of iterative or trial and error methods.

4.3.2 – Model Application

The model was applied to ferritic – pearlitic microstructure as explained above. For the particular application, a G11 low carbon steel was used [4]. The aim was to adequately model, simulate and finally represent the grain distribution of the alloy according to the microstructure that was captured from optical microscopy (figure 4.4a below), [4].

The sites coordinates were determined with the use of the Rhinoceros CAD program. The procedure was firstly to determine the coordinates of several points (sites) in Rhinoceros, as recommended in [11]. Then with the use of the program Grasshopper (Rhinoceros add-in) their Voronoi diagram was created iteratively, until ferrite and pearlite percentages of the Voronoi diagram had small deviation from the specimen’s microstructure’s amounts respectively.

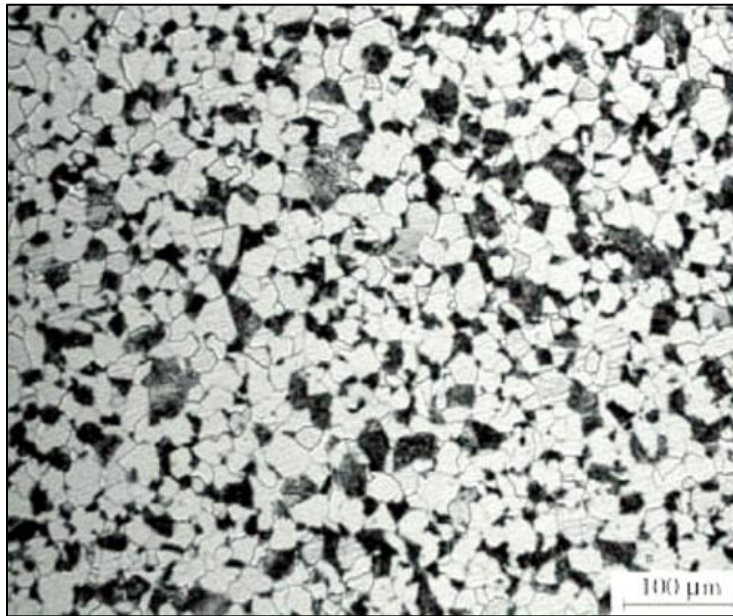


Figure 4.4a: Micrography (optical microscopy) of the G11 steel (ferritic - pearlitic micro-structure)
Etching: Nital 2% [4].

The amounts of ferrite phase and pearlitic micro-constituent in the microstructure of G11 were obtained employing image processing software MIPAR (see figure 4.4b), as recommended in [11].

After the determination of the spatial coordinates of the Voronoi sites on Rhinoceros they were exported from it and imported in the matlab code (annex 1 - code 4). Then the model (annex 1 - codes 1-4) were executed and produced the geometry shown in figure 4.5a below.

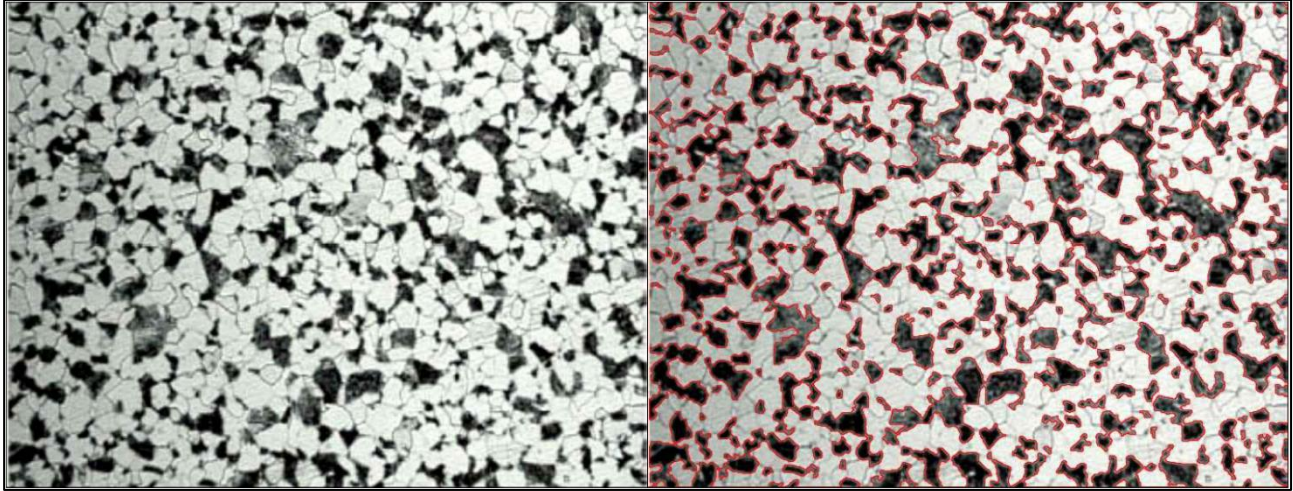


Figure 4.4b: The process used on the G11 steel specimen's microstructure (left picture) for the pearlite and ferrite portion measurements (right picture). All pearlitic micro-constituents (black regions) are circumscribed (red outline) so that the area inside will be measured (MIPAR software)

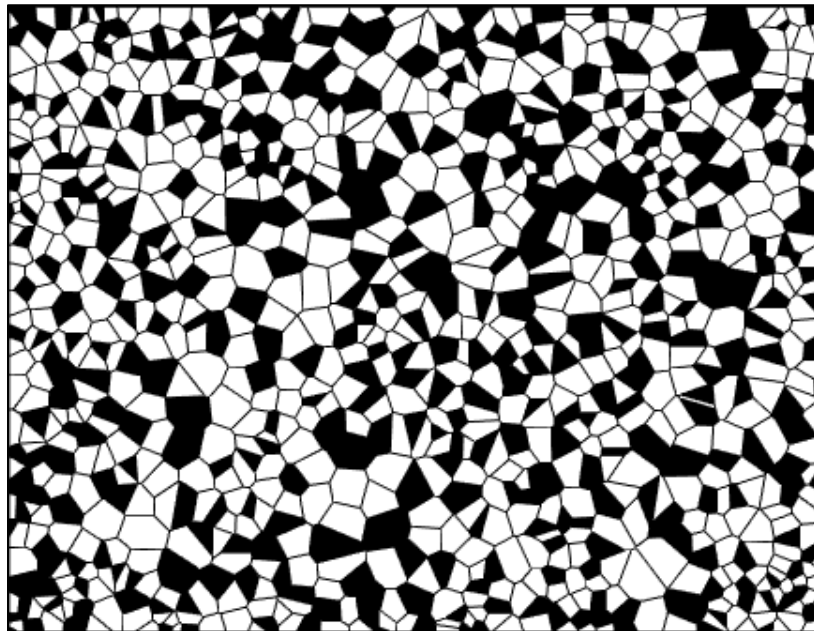


Figure 4.5a: The modelled (annex 1 – codes 1-4) ferrite and pearlitic micro- structure of G11 steel. The white regions stand for the ferritic phase and the black regions are the pearlitic micro-constituents.

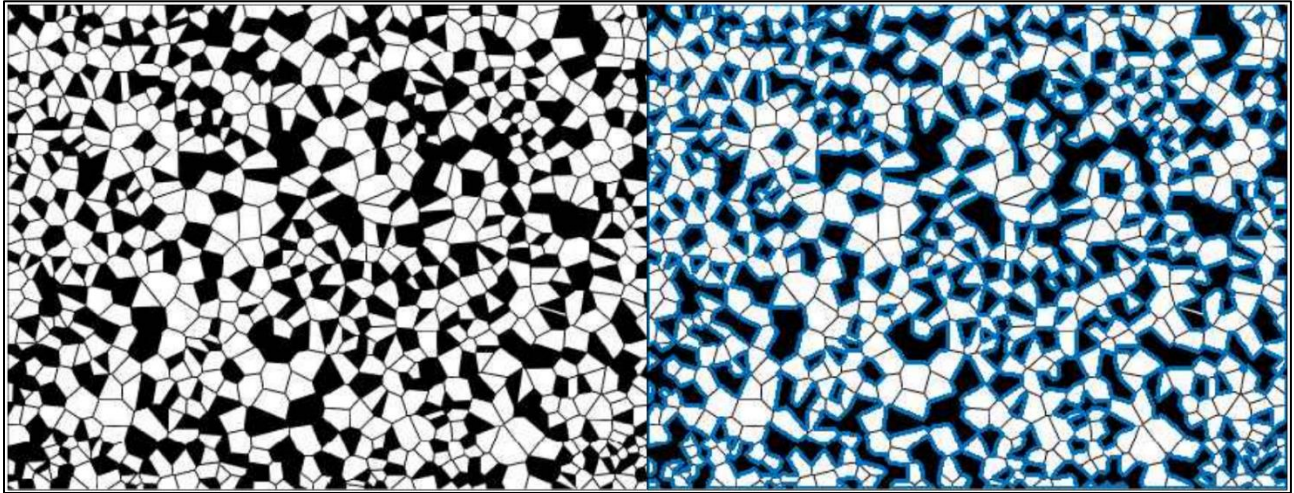


Figure 4.5b: The process applied on the modelled G11 steel microstructure (left picture) for the calculation of ferrite phase and pearlitic micro-constituents (right picture). All pearlitic phases (black regions) are circumscribed (red outline) so that the area inside will be measured (MIPAR software)

The amount of ferrite phase and pearlitic micro-constituent in the microstructure of modeled G11 microstructure were obtained with the MIPAR (see figure 4.5b) as well. The results obtained for the percentages are shown in table 4.1 below. According to table 4.1, the determined Voronoi site positions produce a geometry simulation whose deviation in phase percentages is very small in comparison to specimen's real ones. Figure 4.5a is therefore the final simulation.

In the same microstructure with minor adjustments, a similar image was created (see figure 4.6), this time with grain boundaries spatially enhanced – thickened in this case.

	Ferrite Percentage (%)	Pearlite Percentage (%)
Specimen 's Microstructure	69.58	30.42
Modelled Microstructure	69.22	30.78

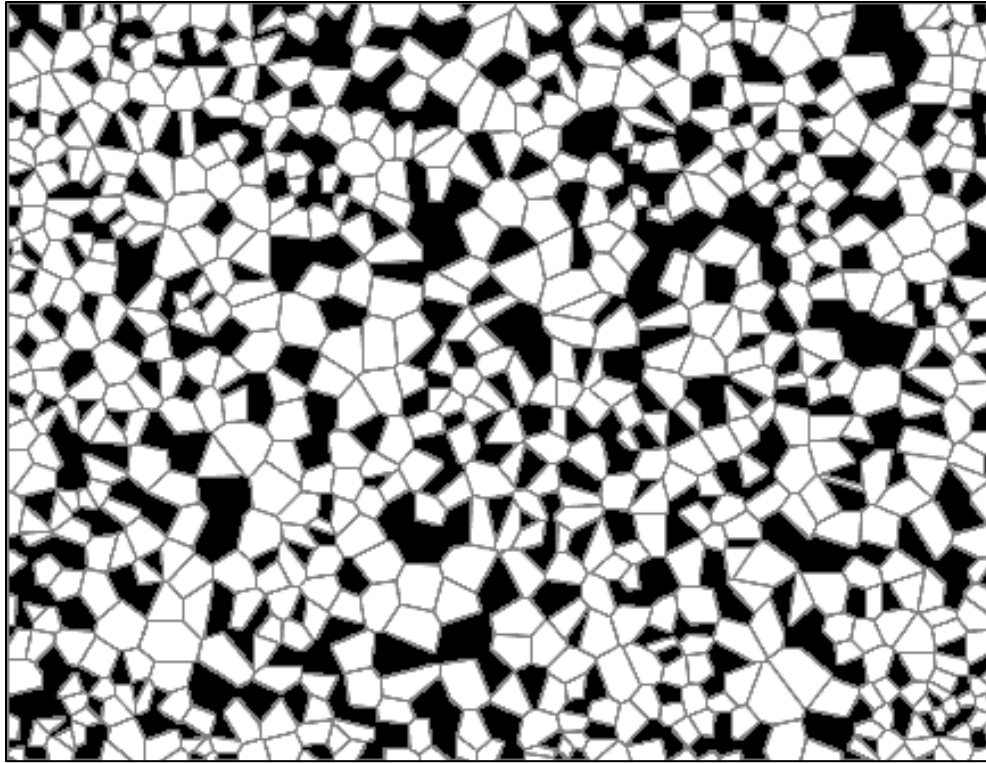


Figure 4.6: The modelled (annex 1 – codes 1-4) ferrite and pearlite grain structure of G11 steel, after further process so that ferrite grain boundaries are thickened. The white regions stand for the ferritic grains and the black regions are the pearlitic micro-constituents, while gray regions are the grain boundaries.

For the visual comparison between the specimen's actual and the modelled microstructure, figures 4.7 and 4.8 are presented. Figure 4.7, refers to the normal simulation and figure 4.8 to the image of the thickened grain boundaries.

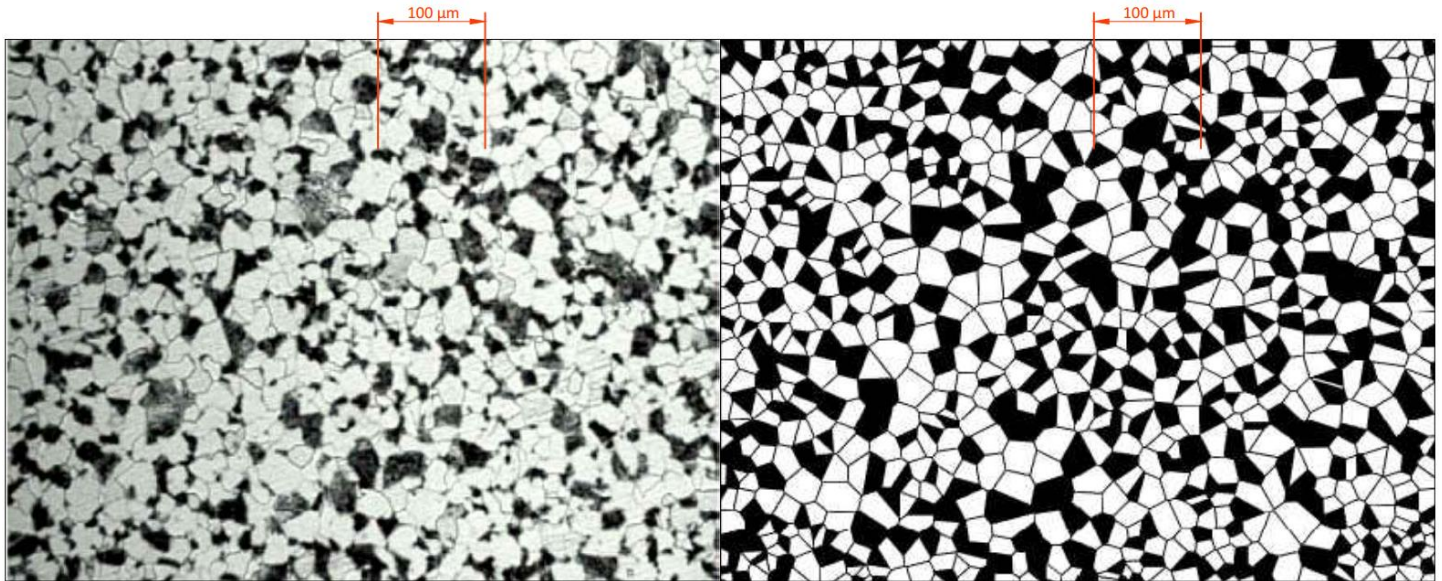


Figure 4.7: Comparison between the specimen's (left picture) and the modelled (right picture) of G11 steel microstructure

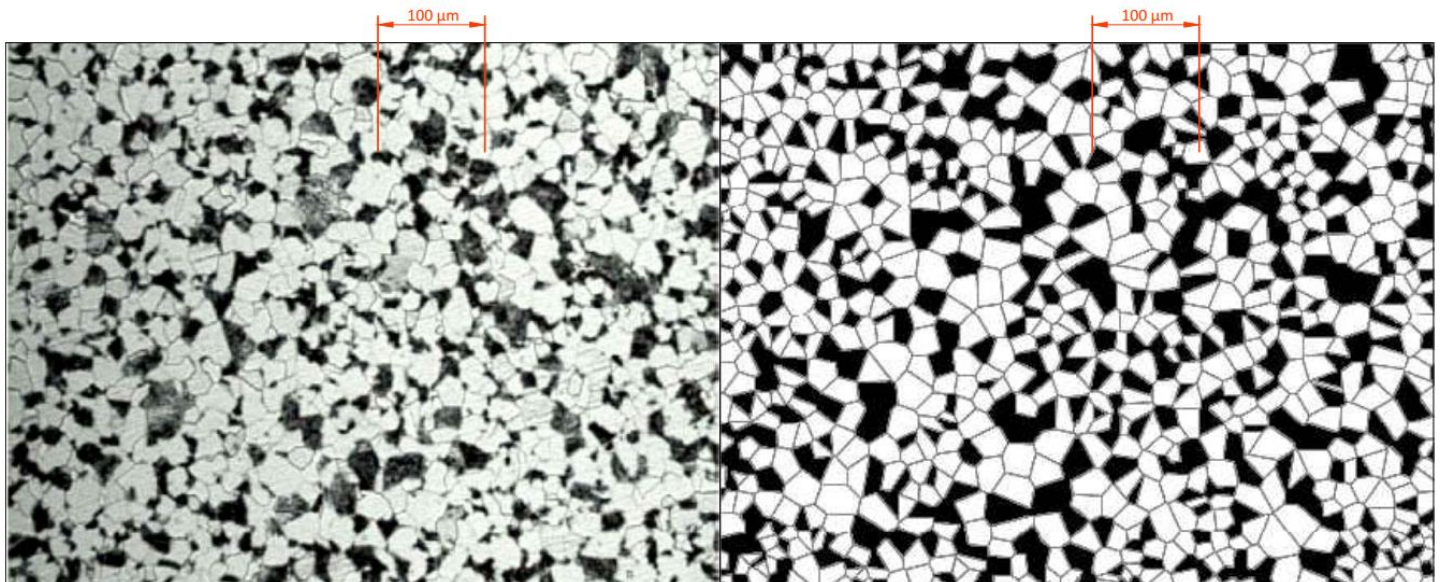


Figure 4.8: Comparison between the specimen's (left picture) and the modelled with enlarged grain boundaries (right picture) of G11 steel microstructure

4.4 – Results and Discussion for Microstructure Simulation

Considering the above analysis, the following conclusions are made:

- Voronoi tessellation approach can adequately simulate the micro-structure of polycrystalline material structure, since it is composed of an enormous number of grains and its properties and performance are determined not only by characteristics of individual grains, but also by the connectivity and interaction between them. The only prerequisite is that it contains fine grain distribution, not affected by external heat treatments or manufacturing processes e.g. rolling.
- The similarity between the modelled and the actual specimen's microstructure can be also explained by the mathematical principles of the Voronoi tessellation. Such discretization is based on the division of space into regions that include all the area closer to the generation point compared to all other generation points. By applying this partitioning into a metal's grain structure, one can correlate the site of a Voronoi cell to the solidification nucleus of the grain represented by the cell. This physically implies that the grain is supposedly solidificated around its generating nucleus, enclosing the material closer to this nucleus than to any other solidification nucleus.
- Any geometries that the model creates can be exported to other finite element packages for the analysis of certain physics governing the microscale geometry of a polycrystalline material.
- The ferrite and pearlite percentages on the model application's microstructure deviates by 0.36% from the actual microstructure. This amount of deviation is considered acceptable and therefore negligible for most cases (e.g. stress-strain analysis) on which this model could be applied.

BIBLIOGRAPHY – CHAPTER 4

- [1] Παντελής Δ.Ι , Χρυσουλάκης Γ.Δ , “Επιστήμη Και Τεχνολογία των Μεταλλικών Υλικών”, Εκδόσεις Παπασωτηρίου 2^η έκδοση , 2008.
- [2] Gunther Lukat, Jens Krüger and Björn Sommer, “A Voronoi-based Membrane Analysis Tool for Gromacs Trajectories”, American Chemical Society Journal of Chemical Information and Modeling, 2013.
- [3] O. Oluwole and A. Akinkunmi, “Modeling Grain Structures of Some Carbon Steels using Voronoi Tessellation”, Journal of Minerals and Materials Characterization and Engineering, Vol. 10 No. 3, pages 309-314, 2011.
- [4] Ieda Caminhaa, Chaoliu Zengb, Marcelo Piza Paesc, Maurício Jesus Monteiro d , Fernando Rizzod, “Corrosion Resistance of a Steel Under an Oxidizing Atmosphere in a Fluid Catalytic Cracking Regenerator”, Materials Research Journal, Vol. 7, No. 1, pages 183-188, 2004. (<http://dx.doi.org/10.1590/S1516-14392004000100024>)
- [5] Weisstein, Eric W. "Voronoi Diagram." From MathWorld - A Wolfram Web Resource. (<http://mathworld.wolfram.com/VoronoiDiagram.html>)
- [6] Samuel Peterson, “Computing Constrained Delaunay Triangulations, University of Minnesota”, Minnesota Center for Industrial Mathematics Undergraduate Industrial Mathematics Project, 1997-1998. (http://www.geom.uiuc.edu/~samuelp/del_project.html)
- [7] J.L. Meijering, Phillips Research Reports, Volume 8 page 270, 1953.
- [8] Zhigang Fan, Yugong Wu, Xuanhe Zhao, Yuzhu Lu, “Simulation of polycrystalline structure with Voronoi diagram in Laguerre geometry based on random closed packing of spheres” , Computational Materials Science Journal ,Volume 29, Issue 3, Pages 301–308 , 2004.
- [9] Liebling, Thomas M, Lionel Pournin, “Voronoi Diagrams and Delaunay Triangulations: Ubiquitous Siamese Twins.”, Journal of the Deutsche Mathematiker-Vereinigung, Extra volume, pages 419 - 431, 2012.

[10] “Circling, squaring, and triangulating”, Blog notes at Mathmunch.org, 2013.

(<https://mathmunch.org/2013/05/08/circling-squaring-and-triangulating/>)

[11] Traka K., “Numerical simulation of electrochemical behavior for naval steel microstructure via Tafel curves extrapolation method”, Diploma Thesis for the degree of Naval Architecture and Marine Engineering, National Technical University of Athens, 2016.

CHAPTER 5 – NUMERICAL MODELLING OF THE ELECTROCHEMICAL BEHAVIOUR OF AH36

5.1: Introduction

Steels are commonly a matter of academic research, due to their wide usage in a vast variety of applications. Contemporary industry is very often using steels, which are required to meet each construction's demands. The properties of an alloy can differ amongst others, depending on the alloying elements and all preceded processes it has been submitted.

Corrosion behavior is directly affected and thus commonly studied, especially for the carbon steels, since they are considered to be vulnerable to such deterioration, according to [5],[4]. The casualties are magnified considering the corrosive environment marine structures are exposed to (as explained in chapter 1). However, it is very difficult to develop a deterministic rule, able to calculate an alloy's behavior under corrosion, as an outcome of the procedures it has undergone. Therefore, naval steel alloys have always been under experimental examination for the evaluation of their electrochemical behavior. Of course, these experiments are both time and cost consuming. Consequently, attempts for the development of new methods, rather than experiments, for the prediction of such behavior, could be useful both for the industrial and the scientific community.

In this study, a numerical model for the prediction of the ferritic – pearlitic low carbon steels, corrosion behavior, is developed. Instead of collecting new data (via experiments) for the steel, the electrochemical processes could be studied as a combination of its composing phases, according to [4]. In particular, a model is proposed, estimating the corrosion variables of ferritic– pearlitic microstructure, depending on the portions and the distribution of each phase.

The scientific foundation of the model derives from two assumptions:

- Firstly, it is assumed that the corrosion kinetics of the alloy will be a function of the ones describing the ferrite phases and pearlite micro - constituents, thus resulting to an intermediate behavior.

- Secondly, since ferrite has been found (according to chapter 3) to be more drastic (of a more negative electrochemical potential) than pearlite, it could be reasonably stated that a galvanic couple forms between adjacent (so that electrical conductivity between them is ensured) grains.

Ferrite could be acting as an anode (providing electrons both to the electrolyte and the pearlitic regions), whilst pearlite could act as a cathode (providing electrons to the electrolyte but gaining some from ferrite). This mechanism would not disturb the total charge's equilibrium, because of current conservation, and therefore the total current measured in the alloy would still lie in-between ferrite and pearlite experimental data. However, the corroding processes would not be developed uniformly throughout the steel's surface, but more selectively resulting to differently dissolved regions [3]. With further analysis, the dissolution and the macroscopical pattern of corrosion (whether it is pitting, selective, pericrystalline etc.) could be determined.

The aim of the thesis is to simulate the behavior of AH36 naval steel. However, as mentioned before the rolling of AH36 steel specimen, could not be simulated employing Voronoi tessellation approach. For this reason the microstructure simulated, and the model developed consequently was based on the microstructure of a similar steel, which contains the same amounts of ferritic phase and pearlitic microconstituents, as well as similar grain size, to the AH36 experimental specimen. After the determination of the percentages of each phase, the model's geometry is created in accordance to the experimental microstructure (with respect to chapter 4 simulation). In addition to the geometrical properties, the electrochemical parameters behavior of both phases (as defined in chapter 3), was also needed as an input for the model. For the accomplishment of the aforementioned goals several software programs were employed. The simulation of the microstructure was performed as following:

Concerning the microstructure simulation, with the Rhino software the Voronoi sites were defined; consequently they were imported in Matlab for the creation of the microstructure and the comparison with the experimental one. Next, after the final comparison, the Matlab code was used to create a scatter of points corresponding to each cell, which will represent the microstructure as explained in the following paragraphs. Finally, the simulated microstructure was imported to Comsol Multiphysics for the simulation of the electrochemical behavior.

5.2: Model Development

5.2.1: Geometry

An AH36 naval steel was simulated with respect to the metallurgical phase portions (percentages) measured from the images obtained by optical microscopy, as they are presented in Chapter 3. The particular AH36 steel specimen had been affected from rolling (figures 3.4a, 3.4b) as it was previously described. However, in order for a generic model to be produced, the effects of the rolling procedure had to be neglected. The main reason is the variation found on an industrial steel's grain orientation according to the manufacturing procedures (whether it is rolling, wire drawing etc.). A potential solution to the affected microstructure could have been to submit the specimen to recrystallization annealing process. Since such a procedure would have caused magnification of the grains, it was chosen not to be applied. Therefore, the microstructure of the AH36 metal was decided to be simulated as non-affected from manufacturing procedures. The choice of this microstructure was done with respect to phase portions (percentages) of the experimental microstructure. Thus, a microstructure of an AH36 steel without rolling [9] was chosen as reference and was simulated instead (see figure 5.1).

The model applied for the representation of the grains was the one described in chapter 4, here applied for AH36 instead of G11 steel (see annex 1 – codes 1-4). In specific, the simulation of the AH36 steel's geometry, followed the exact procedure performed for the G11 steel in chapter 4. Of course, in this case, in order for the microstructure to correspond to the AH36, the Voronoi sites had to be different, as they are input parameters for the model (see annex 1 – code 4). Figure 5.1 below, shows the microstructure selected, and the simulated image [9]. The dimensions of the matlab's Voronoi diagram were created in respect to the ones of the AH36 steel's microstructure as the red dimension line denotes in figure 5.1.

The percentages were also measured for the modelled microstructure of the electrochemical model (figure 5.1 right picture), for the comparison with both the microstructures of the AH36 steel used in the experiments (chapter 3 figures 3.4a, 3.4b) and with the AH36 steel chosen for the simulation (from [9]). The percentages of the different metallographic phases are all presented in the following table 5.1.

Table 5.1: Comparison of each metallic phase 's percentages between experimental and modelled AH36

	Ferrite Percentage (%)	Pearlite Percentage (%)
Experimental Microstructure (figure 3.5)	67.8	32.2
Microstructure used for simulation	65.6	34.4
Modelled Microstructure	66.3	33.7

As seen in the above table, there is adequate consistency between the simulated geometry (figure 5.1 right picture), and both the chosen as respective microstructure (figure 5.1 left picture), and the geometry of the specimen for which the electrochemical behavior is modelled (chapter 3 figure 3.5).

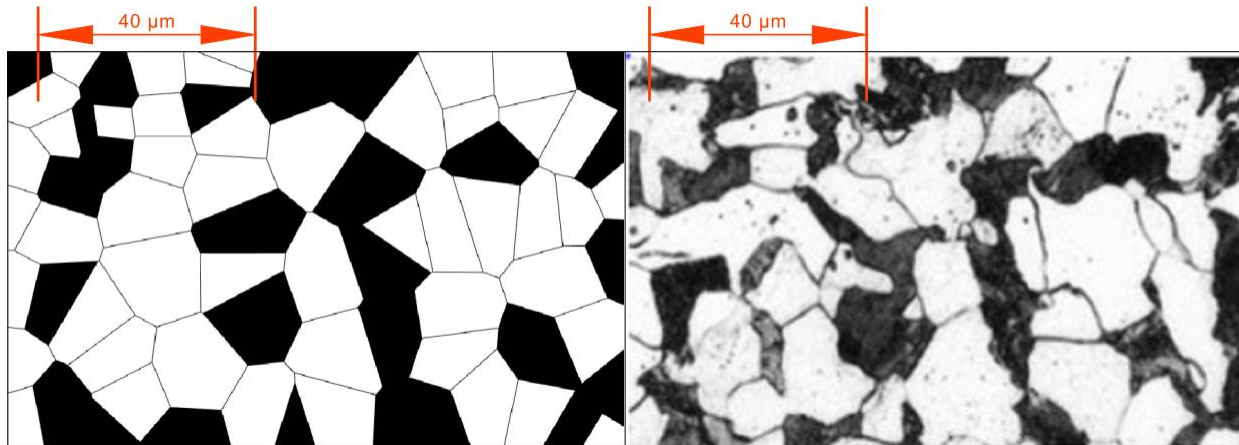


Figure 5.1: The AH36 microstructure simulation that was made with respect to the model of chapter 4 for the geometry definition on the model

With the use of the matlab model (annex 1 – codes 1-4) a scatter of xy points was created. Every point of the scatter within the Cartesian coordinate system, was examined whether it belongs to a Ferrite or Pearlite voronoi cell (see figure 5.2a and figure 5.2b). More specifically, the function $f = \text{micro}(x,y)$ was created, and defined for arguments within a distinct domain (finite set of values x,y). This function receives the values 0 or 1 depending on the position (x,y) as it is shown below.

$$\text{micro}(x,y) = \begin{cases} 1, & \text{if } (x,y) \text{ is inside a Pearlite voronoi cell} \\ 0, & \text{if } (x,y) \text{ is inside a Ferrite voronoi cell} \end{cases} \quad (5.1)$$

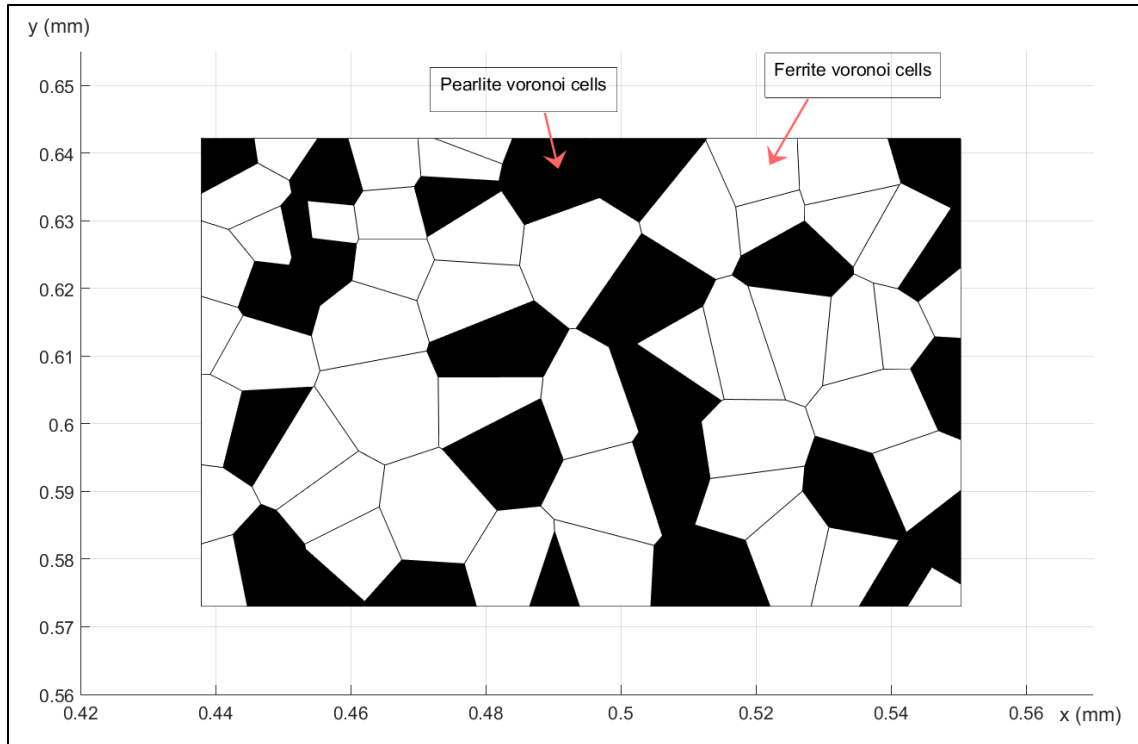


Figure 5.2a: The 2D voronoi geometry as it was created in the xy Cartesian coordinate system in Matlab

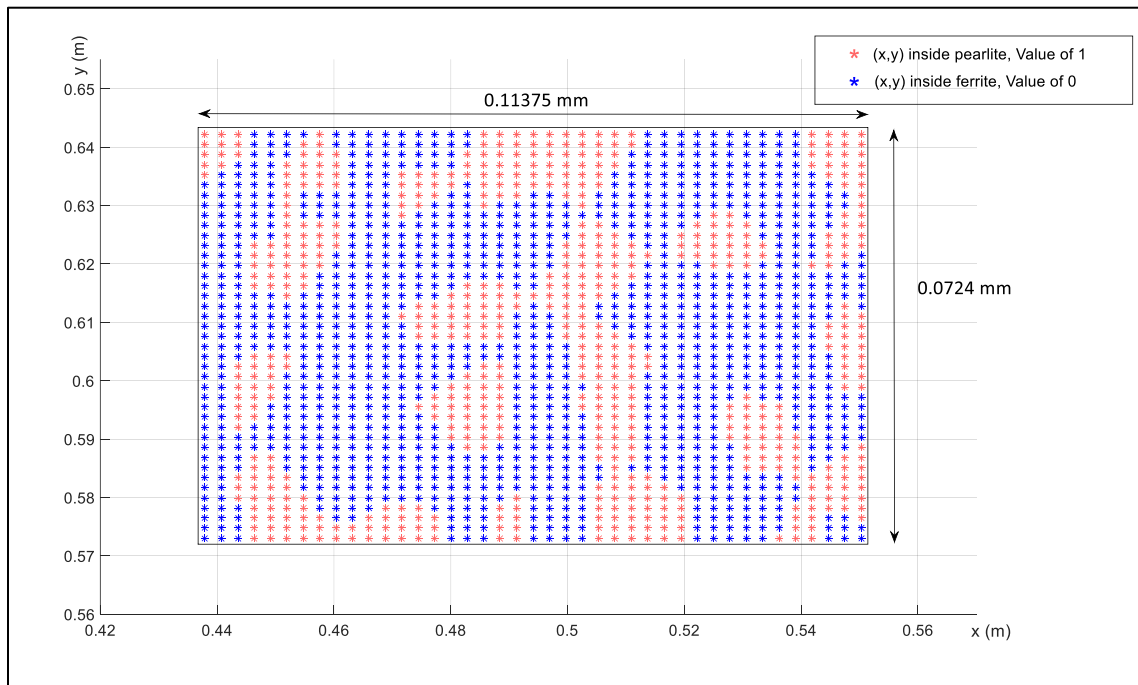


Figure 5.2b: The scatter of points xy colored in accordance to the micro(x,y) function in matlab (red points received the value of 1, blue points received the value of 0)

The discrete function $\text{micro}(x,y)$ was afterwards imported into the finite element software Comsol Multiphysics, and then interpolated. After the interpolation the function $\text{micro}(x,y)$ became continuous, and received values within a range of (x,y) coordinates, as shown in the following figure 5.3.

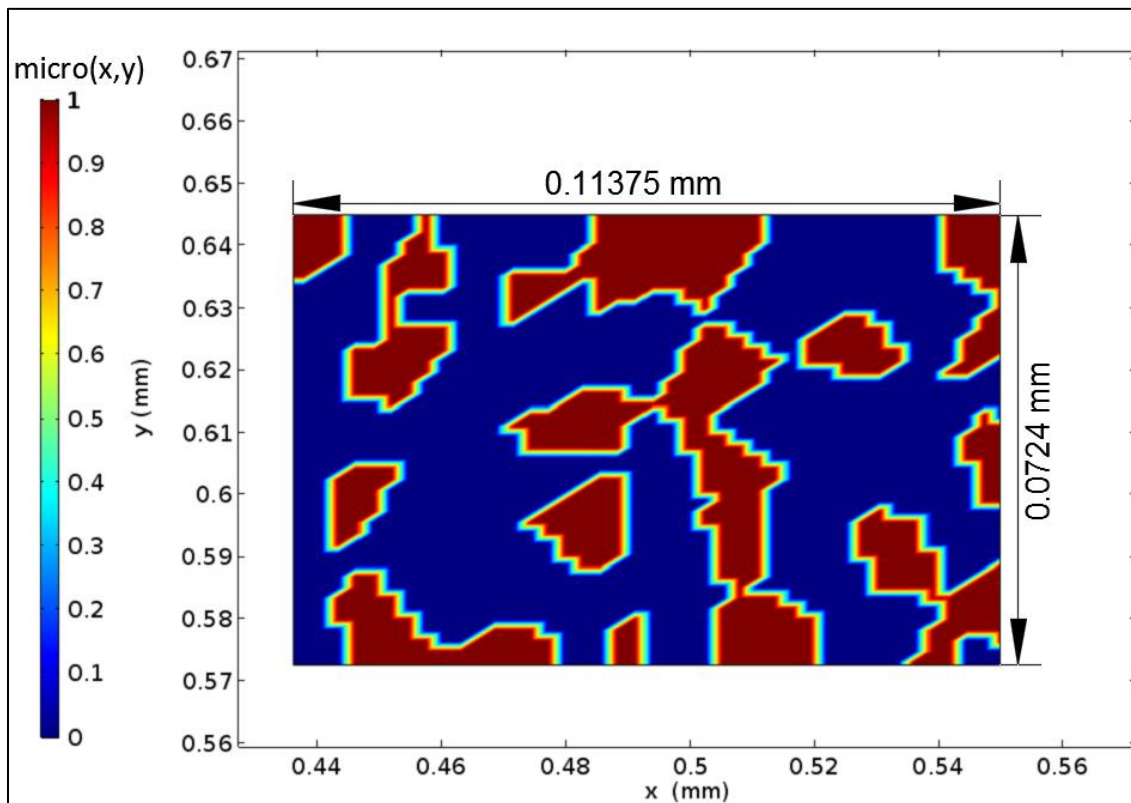


Figure 5.3: Values of the $\text{micro}(x,y)$ function, as they were imported and then interpolated in Comsol Multiphysics (red – $\text{micro}(x,y)=1$ are pearlitic regions, blue – $\text{micro}(x,y)=0$ are ferritic regions)

In the 3D space, a box of $0.11375\text{mm} \times 0.0724\text{mm} \times 0.05\text{mm}$ dimensions represents the aqueous solution of 3.5 % NaCl (figure 5.4). Its interface with the metal was defined as the boundary AH36 – electrolyte as shown in the following figure 5.4.

It is noted that the electrolyte's dimensions and position were defined so that each xy plane of the box would take all the values (xy) within the range of definition of $\text{micro}(x,y)$. This means that the $\text{micro}(x,y)$ domain of definition, shares the same range of values of xy with the electrolyte domain (see figure 5.5).

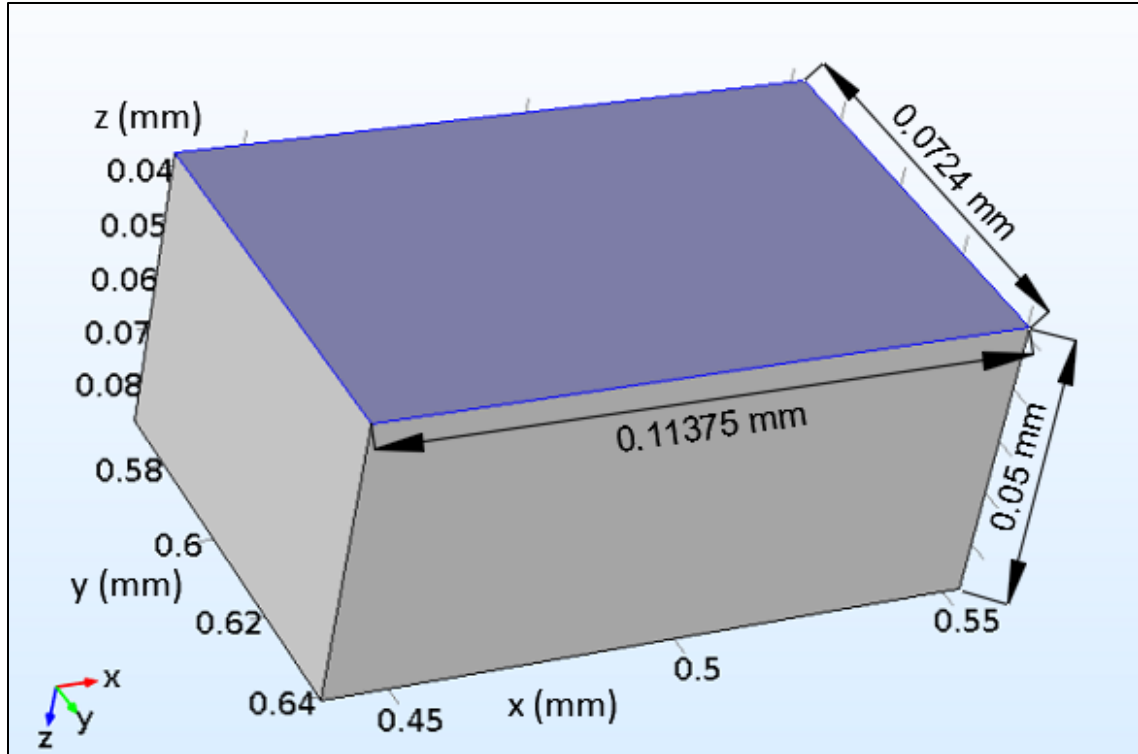


Figure 5.4: AH36 - Electrolyte boundary defined in Comsol Multiphysics (highlighted region)

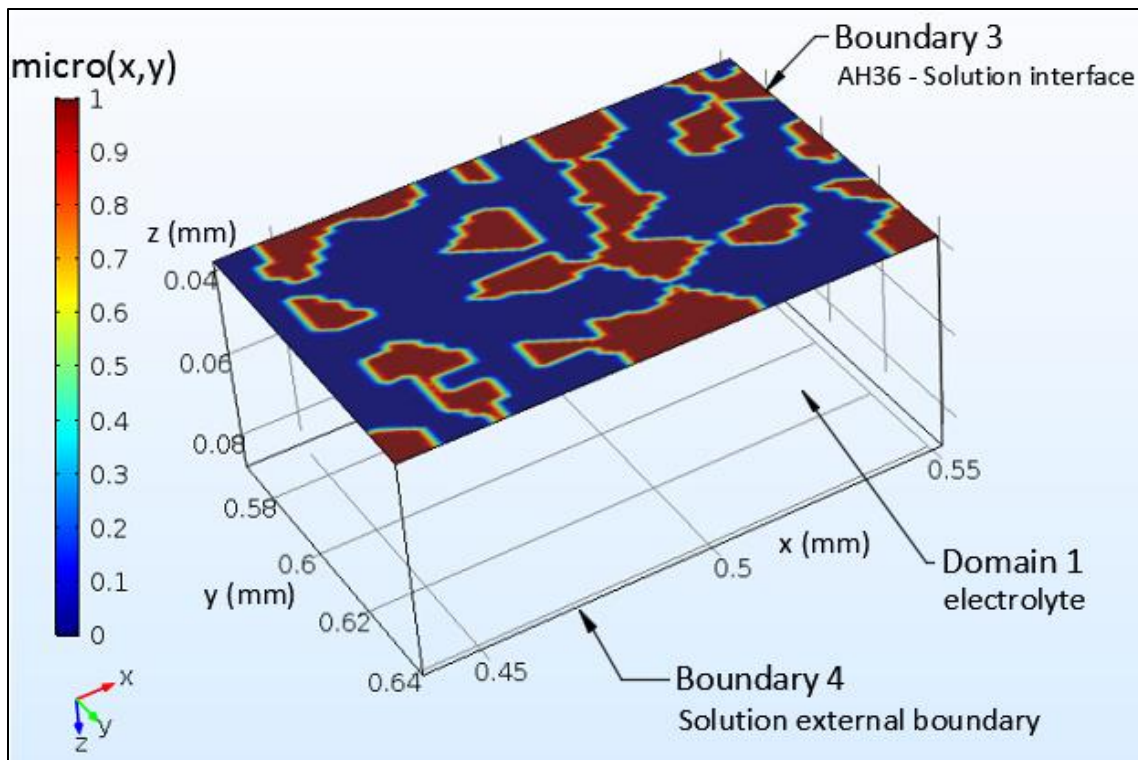


Figure 5.5: Values of the $micro(x,y)$ function, as they were imported and then interpolated in Comsol Multiphysics (red – $micro(x,y)=1$ are pearlitic regions, blue – $micro(x,y)=0$ are ferritic regions)

The above geometry, constitutes of one domain on which (3-D features) boundaries (2-D features) were defined (Fig.5.5). One boundary is defined to express a constant electrolyte potential, while the definition of the metal's domains in this case is set at the opposite boundary mathematically. Thus the subdivision criterion was based upon the function $\text{micro}(x, y)$. In order for the aforementioned model's assumptions (chapter 5.1) to take place, the boundary conditions on both the ferritic and pearlitic regions had to be defined. Their definition spatially will be explained in the following chapter (chapter 5.2.2), since the $\text{micro}(x, y)$ -mathematical function will account for the spatial division. As for the electrolyte it assembles a single domain by itself, due to uniform properties assumed for the solution (as it is also assumed during an actual experiment). The electrolyte's boundary regarded to the assignment of a constant potential value (reference - ground for the electrochemical system) at the furthest face from the corroding surface boundaries. This would act as the electrolyte's boundary of constant potential and thus, it had to be assigned far from its interface with the metal.

The following table 5.2 shows the abbreviation of the domain and the two boundaries, which assemble the complete electrochemical system that will be simulated.

Table 5.2: Definition of Geometry Features in Comsol Multiphysics		
Representing feature	Corresponding domain/boundary	Defined as
H ₂ O with 3.5 % NaCl (3D)	Domain 1	Electrolyte
AH36 – Solution interface (2D)	Boundary 3	AH36 - electrolyte
Solution external boundary (2D)	Boundary 4	Electrolyte Potential

5.2.2: Physics analysis

In the following paragraphs the equations which describe the phenomenon are presented (section 5.2.2.1), as well as the differential equations in the electrolyte domain (par. 5.2.2.2) and finally the definition of the Boundary Conditions (par.5.2.2.3).

5.2.2.1 – System's Physics and Definitions

In order to simulate the actual corrosion process, we must first describe the physics that takes place and in advance the mathematical equations that apply to such phenomena.

Developing the analysis in a certain closed volume V , where:

$$\left\{ \begin{array}{l} V = \iiint_V dV \quad \text{the volume} \\ S = \theta V = \oiint_S dS \quad \text{the boundary (surface) of the volume "V"} \\ L = \theta S = \oint_L dL \quad \text{the "closed" line that encloses "S"} \end{array} \right\} \quad (5.2)$$

At first we call upon the Maxwell's equations. In their differential form they are expressed according to [1] as follows:

Table 5.3: Maxwell equations expressed in differential form	
Equation	Meaning
$\vec{\nabla} \cdot \vec{E} = \frac{\rho}{\epsilon_0} \quad (5.3a)$	The electric field leaving a volume is proportional to the charge inside
$\vec{\nabla} \cdot \vec{B} = 0 \quad (5.3b)$	There are no magnetic monopoles so the total magnetic flux through a closed surface is zero
$\vec{\nabla} \times \vec{E} = - \frac{\theta \vec{B}}{\theta t} \quad (5.3c)$	The voltage accumulated around a closed circuit is proportional to the time rate of change of the magnetic flux it encloses
$\vec{\nabla} \times \vec{B} = \mu_0 \cdot \vec{J} + \frac{1}{c^2} \cdot \frac{\theta \vec{E}}{\theta t} \quad (5.3d)$	Electric currents and changes in electric fields are proportional to magnetic fields circulating about the areas where they accumulate

Where:

- \vec{E} : is the electric field inside the “V” volume
- \vec{B} : is the magnetic field inside the “V” volume
- ρ : the charge density inside the “V” volume
- ϵ_0 : the permittivity

The simulation of the corrosion environment regards to a domain which corresponds to the volume “V”
This domain (volume “V”) represents the bulk of the electrolyte, whose boundary (boundary 3 in table 5.2) is assumed to be in contact with the AH36 corroding metal.

The physics taking place inside the domain is assumed:

$$\left\{ \begin{array}{l} \text{to involve an electric field } \vec{E} \\ \text{absent of magnetic forces so: } \vec{B}=0 \end{array} \right\} \quad (5.4)$$

We also define Q the total electric charge within the contained electric field as follows [1]:

$$Q = \iiint_V dQ = \iiint_V \rho(x,y,z) \cdot dV \quad (5.5)$$

Where:

- $\rho(x,y,z)$: the charge density (used in Maxwell eq. 5.3a) inside the “V” volume (defined in eq. 5.2)

5.2.2.2 – Defining the Differential Equations

First Differential equation

From the assumption (5.4) Maxwell's equation (5.3c) becomes:

$$\vec{\nabla} \times \vec{E} = 0$$

Since the electric field within the domain is irrotational, it will derive from potential and thus:

$\vec{\nabla} \times \vec{E} = 0 \Rightarrow$ There is a $\varphi(x,y,z)$ function (from [1],[2]) so that:

$$\vec{\nabla} \cdot \varphi(x,y,z) = \vec{E} \quad (5.6)$$

Where:

- where $\varphi(x,y,z)$ refers to the electric potential of the electrolyte on spatial coordinates (x,y,z)

The irrotational electromagnetic field indicates an electrostatic field.

The gradient of equation (5.6):

$$\vec{\nabla} \cdot \vec{\nabla} \cdot \varphi(x,y,z) = \vec{\nabla} \cdot \vec{E} \Rightarrow \Delta \cdot \varphi(x,y,z) = \vec{\nabla} \cdot \vec{E} \quad (5.7)$$

From equations (5.2a),(5.7):

$$\Delta \cdot \varphi(x,y,z) = \frac{\rho(x,y,z)}{\epsilon_0} \quad (5.8)$$

Equation 5.8 calculates the potential in any (x,y,z) position within the domain where the Coulombic forces summation induce the electrical charge density of $\rho(x,y,z)$ as defined in equation (5.5). Thus, calculating its value inside the electrolyte's domain where ion concentrations c_i are actually computed [6], the density ρ at any random point (x,y,z) is:

$$\rho = \sum_i z_i \cdot e \cdot c_i \quad (5.9a)$$

Due to the electrolytes characteristics further analysis is made. The electrolytes can be treated as a quasi-neutral in “bulk” regions away from charged boundaries, in the sense that charge fluctuations are much smaller than the total number of charges in a given location [4],[6]. Leading to the following assumption:

$$\left| \sum_i z_i \cdot e \cdot c_i \right| \ll \sum_i |z_i| \cdot e \cdot c_i \quad (5.9b)$$

Where:

- e : absolute of the Coulomb charge
- c_i : the concentration of species i
- z_i : any integer value corresponding to the positive or negative charge of an ion (“+” for cations and “-” for anions)

According to the aforementioned assumptions, it is deduced:

$$\left\{ \begin{array}{l} (5.9a) : \rho(x,y,z) = \sum_i z_i \cdot e \cdot c_i \\ (5.9b) : \left| \sum_i z_i \cdot e \cdot c_i \right| \ll \sum_i |z_i| \cdot e \cdot c_i \end{array} \right\} \Rightarrow \rho(x,y,z) \approx 0 \quad (5.10)$$

As a result, we can set the bulk charge density to zero when computing ion concentrations.

Setting $\rho(x,y,z) = 0$ in equation (5.9b) for the electrolyte domain the governing differential equation will be:

$$\Delta \cdot \varphi (x,y,z) = 0 \quad (5.11)$$

Equation (5.11) denotes satisfaction of the Laplace equation inside the domain of the electrolyte.

Second Differential equation

For the current density – potential relation Ohm’s Law is applied.

The current density \vec{j} within the electric field contained in the electrolyte’s regions is [1]:

$$\vec{j} = \sigma \cdot \vec{E} \quad \stackrel{(5.6)}{\implies} \quad \vec{j} = \sigma \cdot \vec{\nabla} \cdot \varphi(x,y,z) \quad (5.12)$$

Where:

- σ : The electrical conductivity of the electrolyte.
- $\varphi(x,y,z)$: the electrolyte ‘s potential that produces the electrostatic field \vec{E}

5.2.2.3 – Defining the Boundary Conditions

The boundary conditions refer to the 2D Features of table 5.2.

a) For the boundary referring to AH36 – electrolyte (boundary 3) the conditions were set as follows:

- The relationship between the current density and the current as follows:

$$I = - \oiint_S \vec{j} \cdot d\vec{S} \quad (5.13) \quad \text{at } S \text{ the aforementioned boundaries}$$

Where:

- I : the total electric current passing through “S” surface
 - \vec{j} : the current density (the electric current per unit of “S” area)
- With the use of the Faraday Law as explained in chapter 1 (equation 1.21), the volume dissolution through time will be:

$$\left\{ \begin{array}{l} dm = \frac{\int_0^t I \cdot dt}{F \cdot n} \cdot MW \\ dm = dV \cdot \gamma \quad , \quad \gamma = \text{density} \end{array} \right\} \Rightarrow$$

$$\dot{V} = \frac{dV}{dt} = \frac{d(m/\gamma)}{dt} = \frac{MW}{\gamma} \cdot \frac{\int_0^t I \cdot dt}{F \cdot n \cdot dt} \quad (5.14)$$

Where:

- V : the volume of material 's density γ so that $V = m/\gamma$
- \dot{V} : the rate of volume change dV within the time range dt

➤ Kirchhoff 's First Law [1] for currents:

$$\sum_i^N j_{\text{local}} = j_{\text{total}} \quad (5.15) \text{ at } S \text{ the aforementioned boundary}$$

➤ The current density j_{local} related to alterations of the potential (overpotential η) due to anodic – cathodic reactions occurring on the interface:

$$\left\{ \begin{array}{l} j_{\text{local}} = i_{\text{ferrite}} \cdot (1 - \text{micro}(x,y)) \quad (5.16a) \\ j_{\text{local}} = i_{\text{pearlite}} \cdot \text{micro}(x,y) \quad (5.16b) \end{array} \right\}$$

In equations 5.16a and 5.16b, i_{ferrite} and i_{pearlite} are functions of the potential on the interface, (the overpotential η) which is obtained through experimental data (see chapter 3). In order to transform the current density into a function $j_{\text{local}}(x,y,\eta)$ so that it would receive different values for ferrite and pearlite regions (depending on x,y), the factors $(1 - \text{micro}(x,y))$ and $\text{micro}(x,y)$ were used respectively. The use of these factors also represents the geometrical distinction between the two constituents of the alloy (the ferritic and pearlitic regions). The two

equations will be solved on the same boundary, but will only receive values for their respective phase. For instance in a spatial position where a ferrite micro-constituent is found, no current will be calculated from equation (5.16b), instead only equation (5.16a) will produce a result.

The overpotential is defined as:

$$\left\{ \begin{array}{l} \eta_{\alpha} = E - E_{eq}, \text{ anodic polarization} \\ \eta_c = E_{eq} - E, \text{ cathodic polarization} \end{array} \right\} \quad (5.16c)$$

- Kirchhoff 's Second Law [1] for voltages:

$$E = \varphi_{\text{external}} - \varphi_{\text{electrolyte}} \quad (5.17)$$

- Interfacial current conservation [3]:

$$\vec{n} \cdot \vec{j}_{\text{electrolyte}} = j_{\text{total}} \quad (5.18) \quad \text{at the } S \text{ boundary of normal vector } \vec{n}$$

- Boundary Deformation due to metal dissolution:

The velocity \vec{u} of S boundary's (of normal vector \vec{n}) deformation $d\vec{x}$ is:

$$\left\{ \begin{array}{l} \vec{u} = \vec{n} \cdot \frac{d\vec{x}}{dt} \\ \dot{V} = \oiint_S \vec{u} \cdot d\vec{S} \quad \text{with } \dot{V} \text{ from equation (5.14)} \end{array} \right\} \quad (5.19)$$

- b) For the boundary referring to the furthest side from the metallic surface, found within the electrolyte domain (electrolyte potential - see table 5.2), the condition set is:

$$\varphi = \varphi_0 = \text{constant} \quad (5.20)$$

5.2.3: Numerical method and Mesh

The mesh created for the calculation of the aforementioned equations was divided into two parts, each one corresponding to the potential complexities of the respective geometry and physics. The electrolyte's domain (domain 1- see table 5.2) equations were solved at the nodes [11] of mesh 1, whilst the AH36-electrolyte boundary (boundary 3 - see table 5.2) equations were solved at the nodes [11] of mesh 2. For both meshes, the elements constituting them were tetrahedral. The difference between the two meshes lies on the range of the dimensions defining the tetrahedral within the mesh. At the boundary of the electrolyte that mesh 1 faces mesh 2 (AH36 - electrolyte interface of domain 1 with boundary 3) the nodes will be shared by the tetrahedral of both meshes (one tetrahedron from mesh 1 and one tetrahedron from mesh 2 will share a side with three nodes) [4] [11]. This requires that the elements' size must be included in both meshes' dimension range, for them to share a tetrahedron's side.

Altering parameter properties on the interface, in addition to highly differing values of dependent variables within mesh 1, create the necessity of a finer mesh [10] in order to achieve convergence of values of dependent variables timewise and spatially. More specifically, the AH36 – electrolyte interface had a variety of equations assigned (tables 5.5), in comparison with the rest of the electrolyte domain. Moreover, the micro(x,y) function, which affects the equations along the xy plane, alters in value even in very close areas, thus, needing high geometrical detail. Therefore, when solving the system numerically, values of big deviation may be calculated for the same variable, even at adjacent nodes, resulting to divergence of the iterative method used.

According to the above requirements, the mesh refinement procedure [10] (figure 5.7) led to the determination of the two meshes (figure 5.6), with their properties shown in table 5.4.

Element Property	Mesh 1 – Domain 1	Mesh 2 – Boundary 3
Maximum element size	0.00398 mm	0.00227 m
Minimum element size	0.00017 mm	0.0000227 mm
Maximum element growth rate	1.35	1.3
Curvature factor	0.3	0.2
Resolution of narrow regions	0.85	1

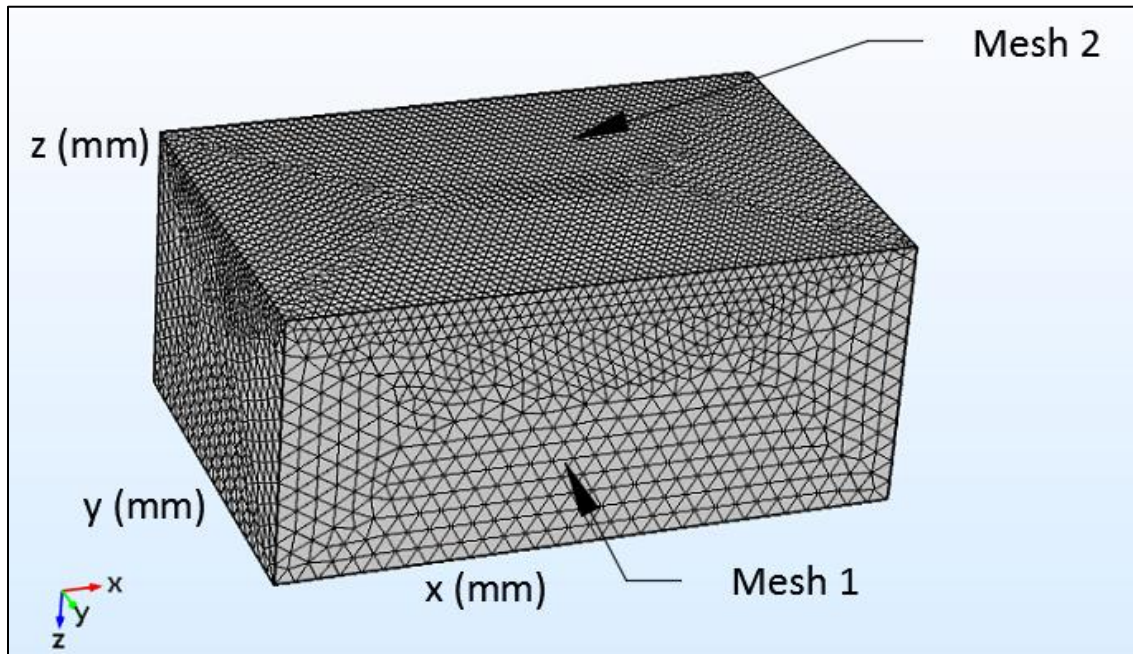


Figure 5.6: The two meshes created for the model

The numerical method chosen was Backwards Euler (one step backward differentiation formula) [7] with an absolute tolerance of 0.001 for every depending variable solved. Here, absolute tolerance is defined as the maximum value of acceptable error (depending on the numerical method used) of any calculated variable, for it to be considered convergent.

The number of elements within the meshes of table 5.4, is 126521 tetrahedral. Since the degrees of freedom are ascending functions of the number of elements (and their corresponding nodes), the convergence was studied in accordance to their number. After producing 6 different couples of meshes, the affection on convergence from the increase in the number of elements was clarified, as shown in figure 5.7.

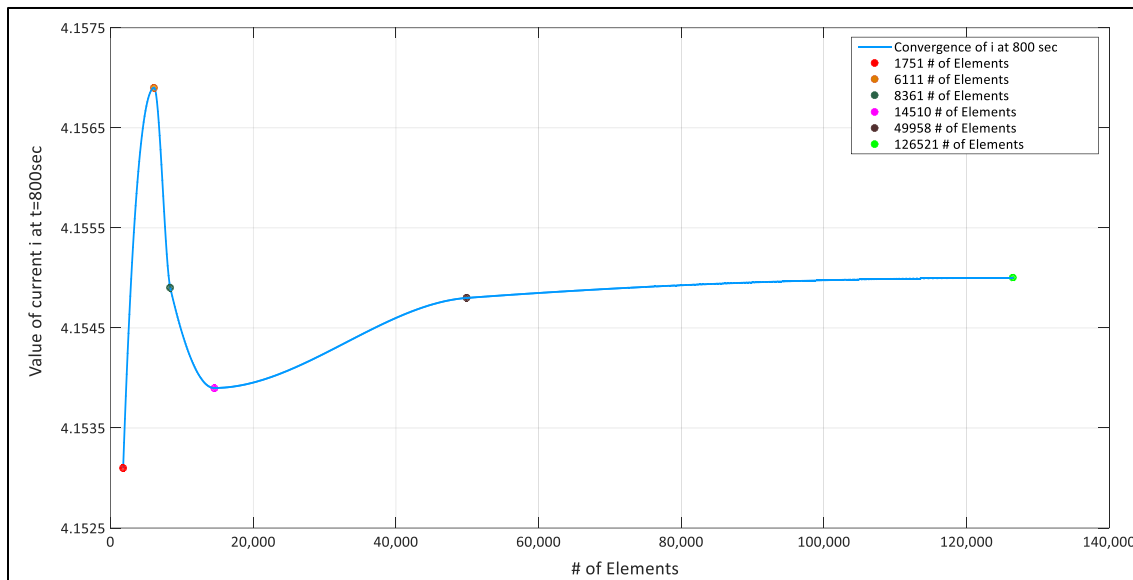


Figure 5.7: Convergence plot for the average (on AH36 corroding surface) current density at $t = 800$ sec
The procedure involved 6 different mesh creations.

From the above figure 5.7, the convergence concerning the values of the current density on the interface of AH36 and the electrolyte is shown. The examined current density was at the time of 800 seconds, since at these time steps, higher divergence among the different meshes was observed (compared to other time steps). This was a reasonable outcome, since convergence regarding to current density values can be deduced from the physics and the parameters of the model's application.

- Spatial convergence: Equation (5.11) is solved at the nodes of mesh 1 and mesh 2, denoting the uniform distribution of currents within the domain. This, in combination with the rise in density near the corroding surface (mesh 2) deduce a smooth transition in current density values from a pearlitic to a ferritic region. Moreover, the differences concerning the current density, between the ferritic and pearlitic regions are not of big magnitude and thus even for adjacent nodes they would not present significant errors especially since the interpolation of the micro (x, y) function led to a non-distinctive transition from the one to the other. According to the above, spatial divergence towards the current density variable is avoided for a mesh of an adequate number of elements.
- Convergence through time: The changes in external potential of the simulation were applied in small steps (see table 5.6b), in order to accurately represent the electrochemical experiment. Hence, between successive time steps, the electrochemical potential and so the current

densities (from equations 5.16) calculated on a certain node, will have a developing value with insignificant error. Therefore, convergence towards the particular dependent variable was ensured for the particular time steps.

5.3 – Modelling Procedure

5.3.1: Model Presentation

According to chapter 5.2.2, where physics was determined and analyzed for both domain and boundaries, the final equations which will be solved in the pre-described meshes (section 5.2.3), are presented in the following tables 5.5a and 5.5b. These tables contain all equations composing the non-linear system. Of course, after assigning them to the appropriate geometrical feature in Comsol Multiphysics (domain or boundary) their including parameters must be defined in respect to the properties of the under simulation system.

Table 5.5a: Model 's Differential equations in Comsol Multiphysics	
Feature as defined in table 5.2	Equation Solved
Electrolyte	$\Delta \cdot \varphi(x,y,z) = 0 \quad (5.11)$
	$\vec{j} = \sigma \cdot \vec{\nabla} \cdot \varphi(x,y,z) \quad (5.12)$

In order for the numerical method of Backward 's Euler [7] to provide solutions regarding the differential equations of table 5.5a, the boundary conditions were chosen (from chapter 5.2.2). These conditions are shown in table 5.5b.

Table 5.5b: Model 's Boundary Conditions in Comsol Multiphysics	
Feature as defined in table 5.2	Boundary Condition
AH36 – electrolyte	$I = - \oiint_S \vec{j} \cdot d\vec{s} \quad (5.13)$
	$\dot{V} = \frac{dV}{dt} = \frac{d(m/\gamma)}{dt} = \frac{MW}{\gamma} \cdot \frac{\int_0^t I \cdot dt}{F \cdot n \cdot dt} \quad (5.14)$
	$\sum_i^N j_{local} = j_{total} \quad (5.15)$
	$\left\{ \begin{array}{l} j_{local} = i_{ferrite} \cdot (1 - \text{micro}(x,y)) \quad (5.16a) \\ j_{local} = i_{pearlite} \cdot \text{micro}(x,y) \quad (5.16b) \end{array} \right\}$
	$\left\{ \begin{array}{l} \eta_\alpha = E - E_{eq}, \text{ anodic polarization} \\ \eta_c = E_{eq} - E, \text{ cathodic polarization} \end{array} \right\} \quad (5.16c)$
	$E = \varphi_{external} - \varphi_{electrolyte} \quad (5.17)$
	$\vec{n} \cdot \vec{j}_{electrolyte} = j_{total} \quad (5.18)$
	$\left\{ \begin{array}{l} \vec{u} = \vec{n} \cdot \frac{d\vec{x}}{dt} \\ \dot{V} = \oiint_S \vec{u} \cdot d\vec{s} \quad \text{with } \dot{V} \text{ from equation (5.18)} \end{array} \right\} \quad (5.19)$
Electrolyte Potential	$\varphi = \varphi_0 = \text{constant} \quad (5.20)$

With the use of the model of tables 5.5, and their corresponding geometry, the final step is to determine the parameters of a specific application. It is important to state, that the described model can be used for any set of parameters, experimentally or otherwise obtained, as long as the corresponding geometry is valid for this application.

5.3.2: Model Application

5.3.2.1: Input values

Here, the application regards the simulation of the electrochemical behavior of AH36 steel and in particular the polarization curves obtained by the potentiostatic experiment as it was conducted and presented in chapter 3. Hence, the following, corresponding to the obtained through process of experimental data values (as explained in chapter 3), parameters are defined on Comsol Multiphysics:

Parameter	Value	Unit	Description	Representing
E _{eq}	0	[V]	Ferrite - Electrolyte Corrosion potential	E _{eq} in (5.16a,b)
rho_fer	7.874	[g/cm ³]	Ferrite micro-constituents density	γ in (5.14)
rho_perl	7.4254	[g/cm ³]	Pearlite phase density	γ in (5.14)
MM_fer	55.845	[g/mol]	Ferrite micro-constituents molar mass	MW in (5.14)
MM_perl	52.338	[g/mol]	Pearlite phase molar mass	MW in (5.14)
sigma	5	[S/m]	Electrolyte conductivity	σ in (5.13)
Phil_0	0	[V]	Electrolyte constant potential (equation 5.23)	φ ₀ in (5.20)

In table 5.6a the pearlite phase's density and molar mass were calculated in accordance to the pearlite's composition with the following formulas:

$$\left\{ \begin{array}{l} \text{molar mass: } MM_{perl} = (0.92 \cdot 55.845 + 0.08 \cdot 12.0107) = 52.338 \text{ g/mol} \\ \text{density: } rho_{perl} = (0.92 \cdot 7.874 + 0.08 \cdot 2.267) = 7.4254 \text{ g/cm}^3 \end{array} \right\}$$

Where:

- 55.845 g/mol and 12.0107 g/mol is the molar mass of iron and carbon respectively
- 7.874 g/cm³ and 2.267 g/cm³ is the density of iron and carbon respectively

The variables, corresponding to the obtained through process of experimental data values (as explained in chapter 3), that were defined in the model on Comsol Multiphysics are shown in the following table 5.6b:

Table 5.6b : The variables used in the model 's application

Variable	Variating Values	Unit	Description	Representing
t	Range (0,1,1000)	sec	Time	t in (5.14)
Phis_ext	$-0.9+0.4*10^{(-3)*t}$	[V]	Applied potential	$\varphi_{\text{external}}$ in (5.17)
$i_{\text{ferrite}}(\eta)$	Experimental results of ferrite (fig.3.2c)	[A/m ²]	Ferrite current density	i_{ferrite} in (5.16a)
$i_{\text{pearlite}}(\eta)$	Experimental results of pearlite (fig.3.3c)	[A/m ²]	Pearlite current density	i_{pearlite} in (5.16b)

5.3.2.2: Results

First Execution Results – Polarization curves

The results of the application's execution on Comsol Multiphysics, regarding the current - potential relation are shown in the following figure, compared to the respective of the experimental data (of figure 3.14c on chapter 3). The numerical results present very good agreement to the experimental ones. Figure 5.7 shows that the simulation model predicts with sufficient accuracy the experimental results.

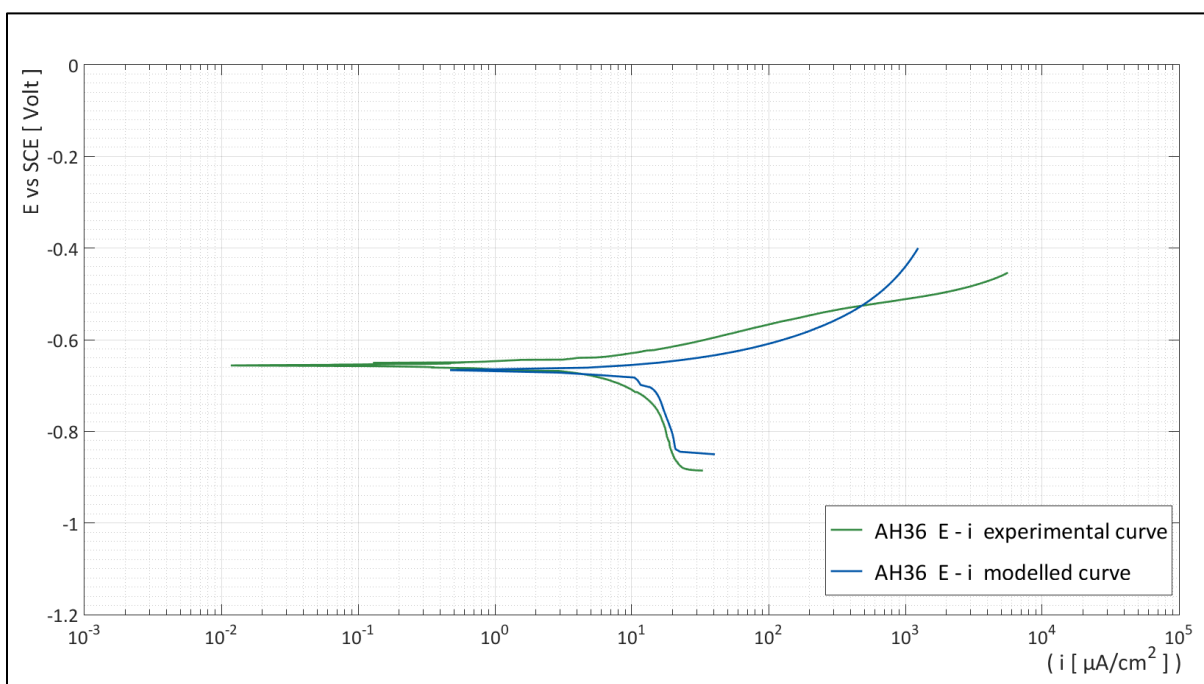


Figure 5.7: Comparison of the modelled AH36 current – potential curve with the respective experimental

For the evaluation of the exchange current density and corrosion potential values (i_{corr} , E_{corr}) of the model's results, regarding to the system of AH36 – electrolyte, the same methodology developed (see annex 2: codes 1-3) in chapter 3 was applied. The following figure 5.8 and table 5.7 show the obtained electrochemical Tafel curves and parameters respectively.

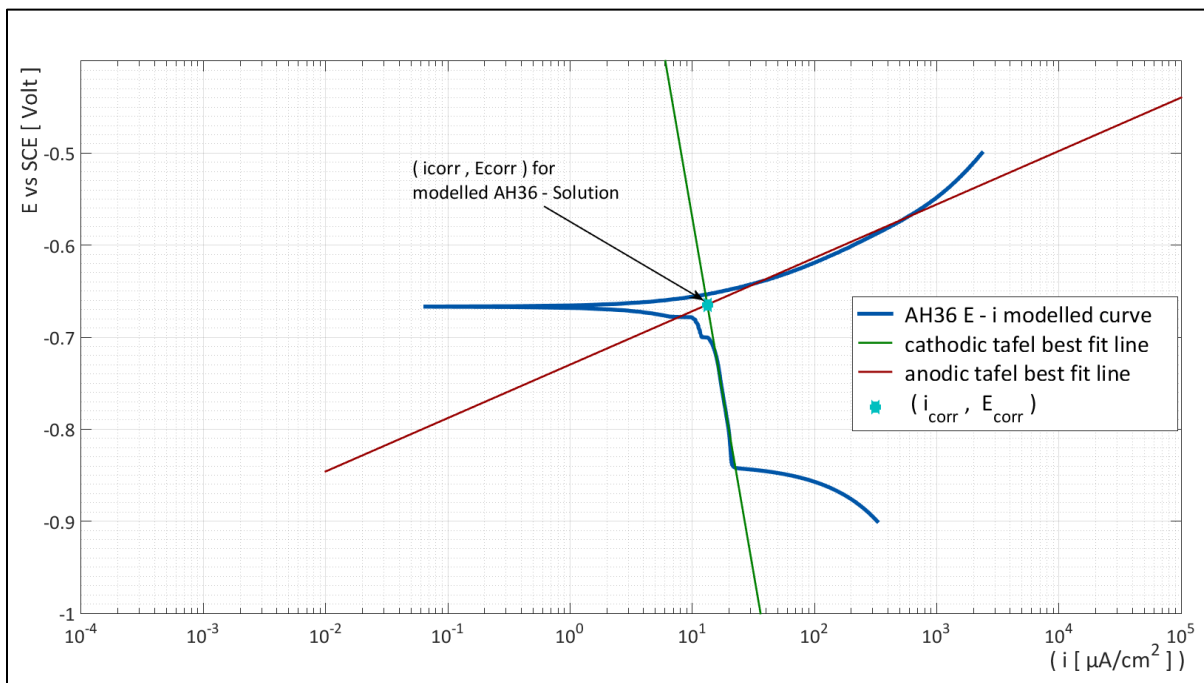


Figure 5.8: Tafel extrapolation on Current – Potential AH36 modelled results

Table 5.7: Electrochemical results for the modelled AH36 – (H ₂ O+3.5% NaCl)		
Electrochemical term	Obtained Value	Units
Anodic Tafel slope (Pearlite oxidation) β_{α}	0.058033	Volts
Cathodic Tafel slope (Solution reduction) β_c	-0.7699	Volts
Anodic Tafel fit line Dispersion S_{final}	$2.0255 \cdot 10^{-4}$	Volts
Cathodic Tafel fit line Dispersion S_{final}	$4.0581 \cdot 10^{-5}$	Volts
i_{corr}	13.2892	$\mu\text{A}/\text{cm}^2$
E_{corr}	-0.6647	Volts

In figure 5.9 the polarization curves of the modelling developed in the present thesis (exploiting experimental polarization data) and the modeled developed via Tafel curves extrapolation, in Thesis by K. Traka [4] are presented in the same graph, with the experimental curve as well.

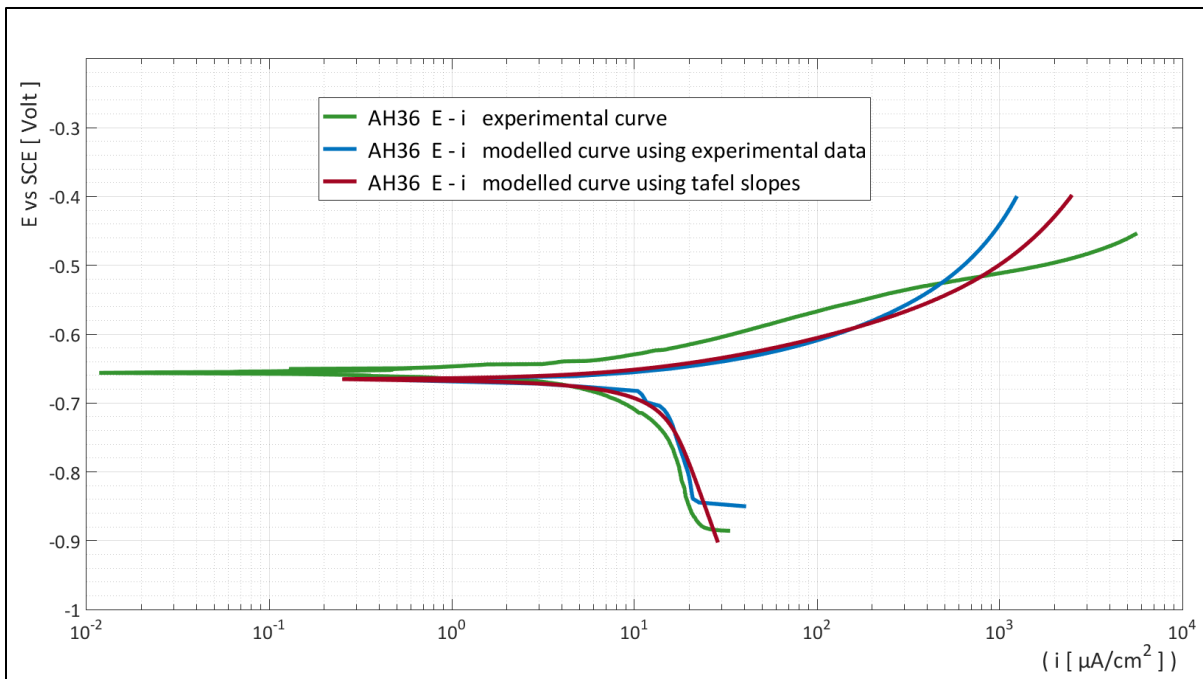


Figure 5.9: Comparison of the modelled AH36 current – potential curve with the respective experimental and the respective modelled curve of [4]

Electrochemical term	Experimental Value	Modelled Value	Modelled from [4]
i_{corr} [$\mu\text{A}/\text{cm}^2$]	11.5275	13.2892	12.3115
E_{corr} Volts	-0.6541	-0.6647	-0.6657

It is obvious that both the models developed are in very good agreement with the experimental curves. This is also supported by the data presented in Table 5.8 where the comparison of E_{corr} and i_{corr} parameters, proves that these values are similar. However, there is a potential range where the current densities seem to deviate between the curves in figure 5.9. In specific, at the anodic parts, around -0.54 Volts the model seems to start being incapable of predicting the anodic polarization. Therefore, the model is considered validated for the range of external potentials of -0.9 Volts to -0.54 Volts.

Second Execution Results– Metal dissolution

The application was executed again on Comsol Multiphysics, with the aforementioned parameters (table 5.6a) as they were defined but for different (instead of table 5.6b) external potential and time values, as shown in the following table (table 5.9). In the particular execution, the time range varied from time 0 to 3600 seconds, so that the external potential would vary from -0.9 Volts to -0.54 Volts, since this is the range at which the model is assumed to be valid.

Table 5.9: The variables used in the model 's second application

Variable	Varying Values	Unit	Description	Representing
t	Range (0,4,3600)	sec	Time	t in (5.14)
Phis_ext	$-0.9+(0.4/4000) *t$	[V]	Applied potential	$\varphi_{\text{external}}$ in (5.17)

The purpose of the second execution is to give a clear image of the dissolution that the metal experiences during the model application. The final image generated at the time step of 3600 seconds (-0.54 Volts external potential) is given in the following figure (figure 5.8).

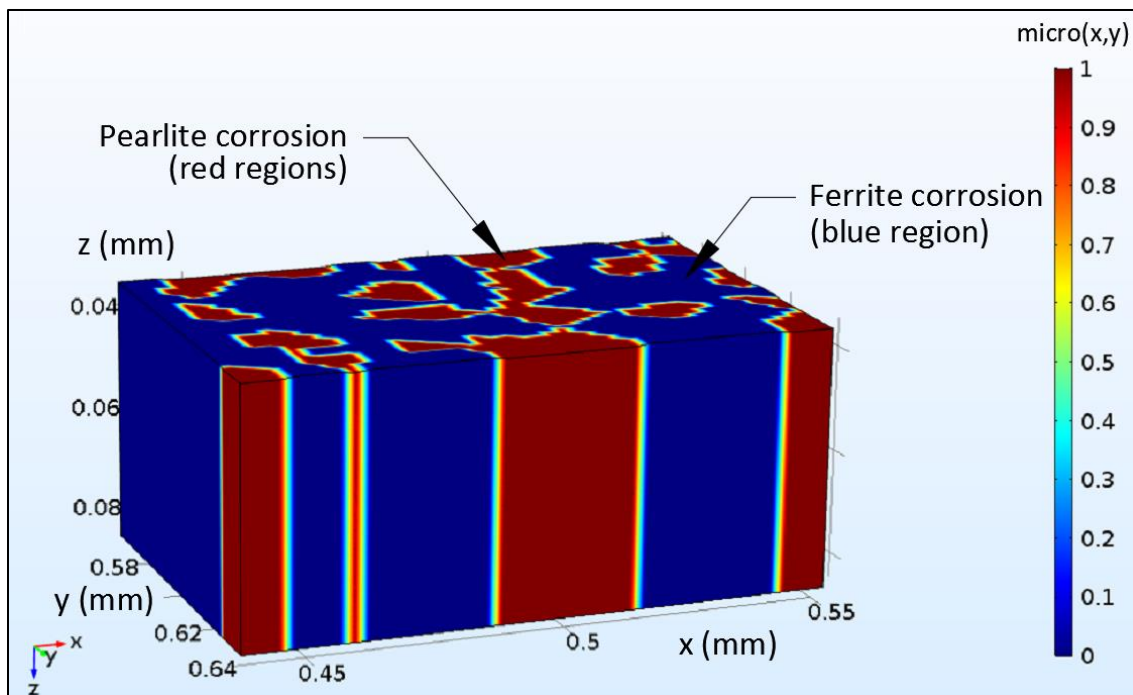


Figure 5.10: Results of the simulation in Comsol Multiphysics regarding the electrolyte's potential at t=3600 sec

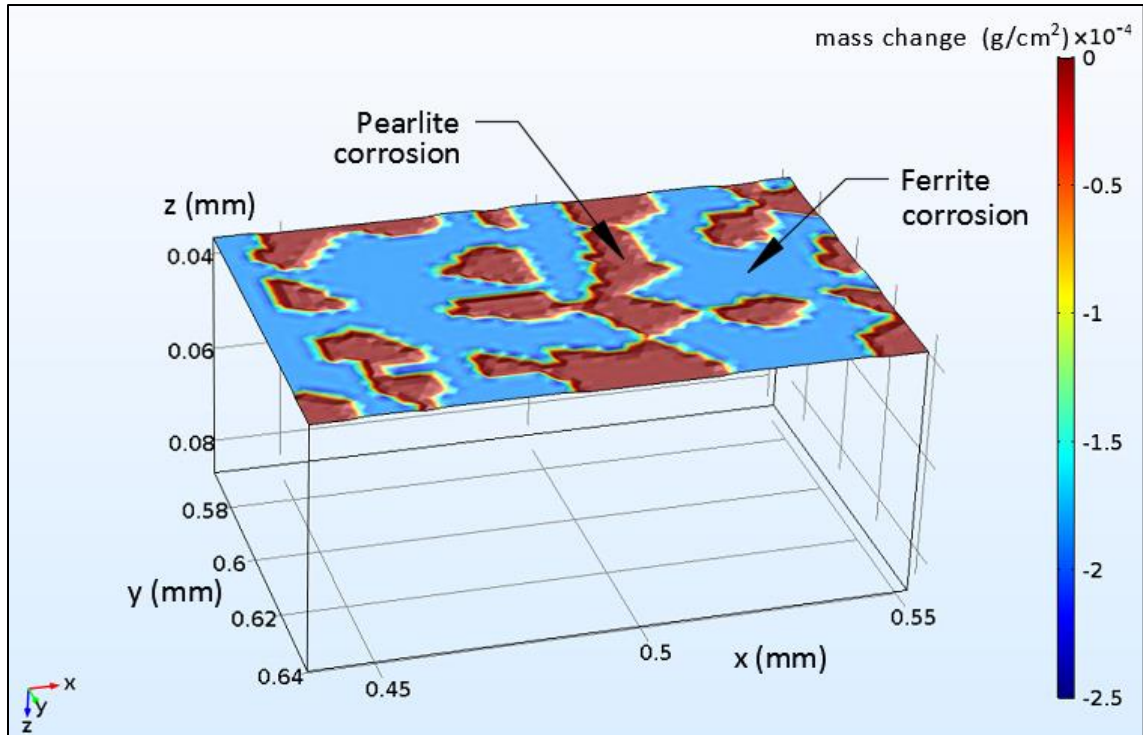


Figure 5.11: Results of the simulation in Comsol Multiphysics regarding the mass change (dissolution) at $t=3600\text{sec}$

Here (figures 5.10 & 5.11), the electrolytes domain is observed to have been expanded. This expansion represents the shrinking of the metal (whose geometry is not represented in this model as a 3D entity). The metal has corroded more on the anodic areas (ferrite micro-constituents) in comparison to the cathodic (pearlite phases). The ferritic regions (value of 0 - blue regions in figure 5.10) have been more intensely corroded in contrast to the pearlitic (value of 1 – red regions in figure 5.10), as it can be seen at figure 5.10 where the function $\text{micro}(x, y)$ has been additionally plotted in the electrolyte domain. The dissolution results are additionally seen in figure 5.11 where the ferrite mass change is calculated as $-1.860218 \cdot 10^{-3} \text{ g/cm}^2$, whilst the pearlite mass change is close to zero. In particular, the pearlite mass change was calculated with a positive (but negligible) value, denoting that the hydrogen evolution would result to depositing of the reacting species. Thus, the aggregation was of positive value even at the anodic part.

In the following figures 5.12, and 5.13 the anodic current densities and the dissolution rates are presented respectively, as calculated in Comsol Multiphysics for $t=3600$ seconds (-0.54 Volts external potential).

In specific, figure 5.12 shows the anodic currents on ferrite ($1810 \mu\text{A}/\text{cm}^2$ in particular) being two orders of magnitude more than on pearlite ($71 \mu\text{A}/\text{cm}^2$ in particular) at 3600 sec, implying a much higher corrosion rate. Therefore, there a galvanic couple formation can be assumed between ferritic and pearlitic regions, and so pearlite presents minor dissolution.

Finally, the dissolving velocity was calculated through the corroding interfaces in mpy, where as seen in figure 5.13, the ferritic regions present much higher rates compared to the pearlitic, and thus are in good agreement with all previous plots.

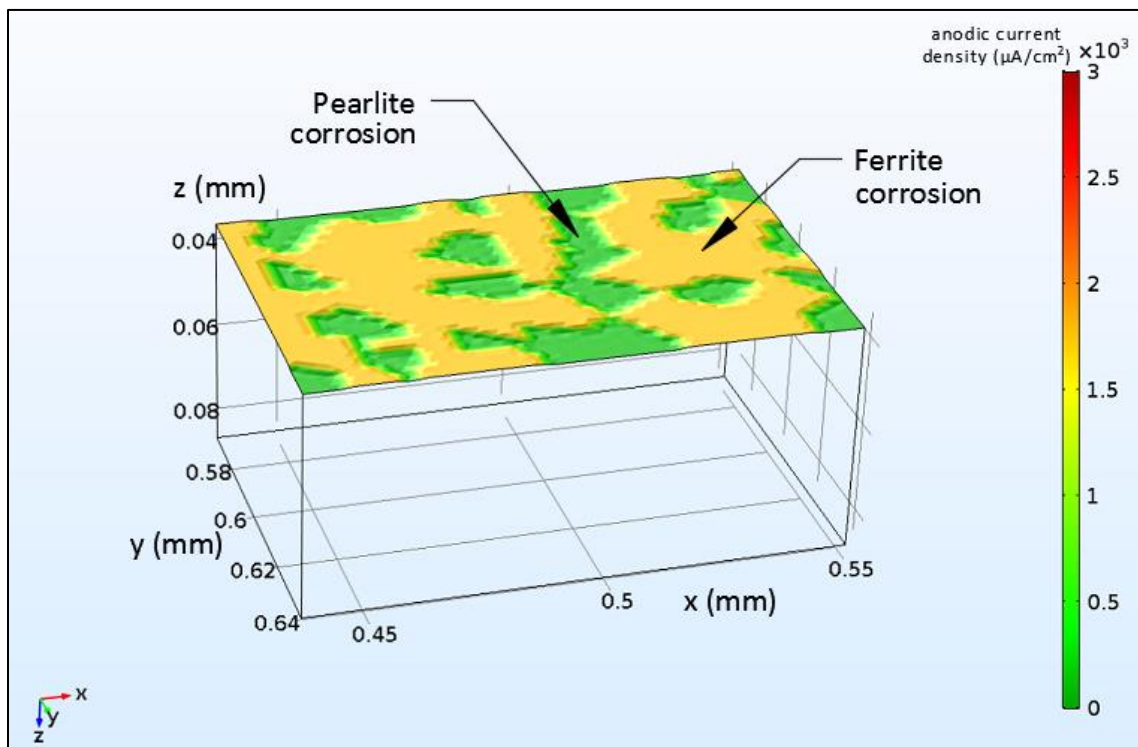


Figure 5.12: Results of the simulation in Comsol Multiphysics regarding the anodic current density at $t=3600\text{sec}$

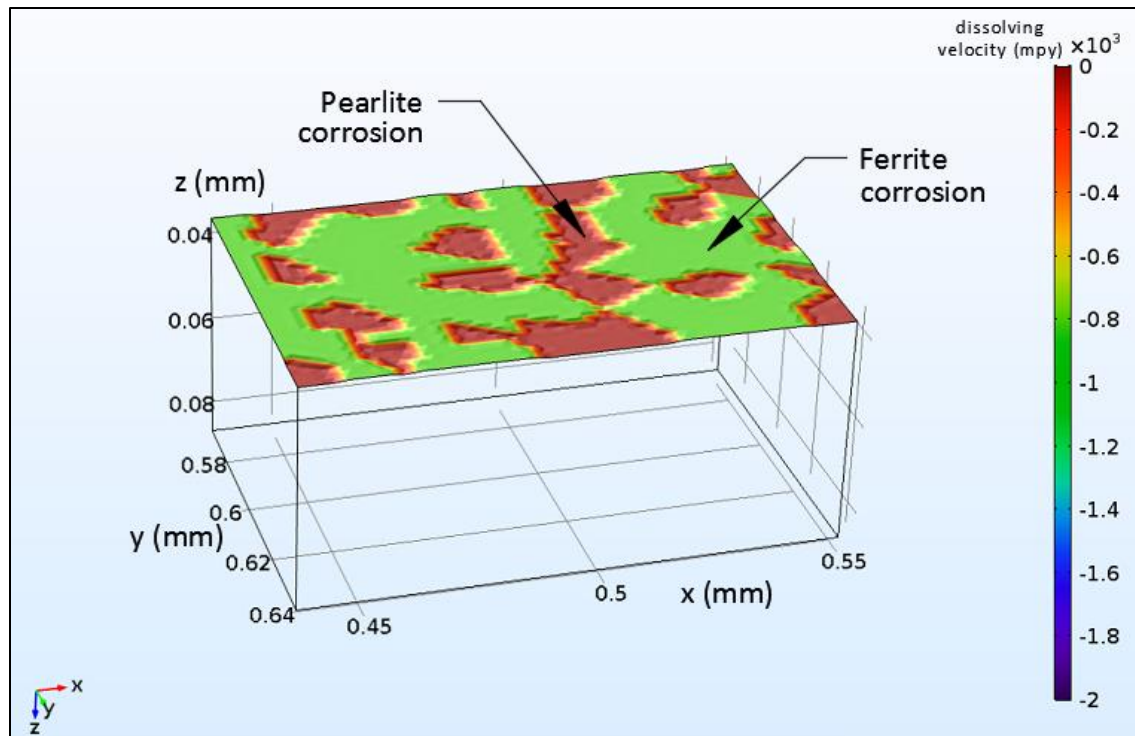


Figure 5.13: Results of the simulation in Comsol Multiphysics regarding the dissolving velocity (corrosion rate) at $t=3600\text{sec}$

BIBLIOGRAPHY – CHAPTER 5

- [1] Hugh D. Young, Roger A. Freedman, “University Physics with Modern Physics”, Pearson Publications-13th edition, 2011.
- [2] Ρασσιάς Θ.Μ., Μαθηματική Ανάλυση ΙΙ, Τεύχος Α’, “Συναρτήσεις Πολλών Μεταβλητών”, Εκδόσεις Συμείων, 2010.
- [3] Melanie Noessler, “Which Current Distribution Interface Do I Use”, Comsol Blog, 2014 (<https://www.comsol.com/blogs/current-distribution-interface-use/>)
- [4] Traka K., “Numerical simulation of electrochemical behavior for naval steel microstructure via Tafel curves extrapolation method”, Diploma Thesis for the degree of Naval Architecture and Marine Engineering, National Technical University of Athens, 2016.
- [5] Παντελής Δ. Ι., Τσιούρβα Θ., “Διάβρωση Και Προστασία Ναυπηγικών Κατασκευών”, πανεπιστημιακές εκδόσεις ΕΜΠ, Αθήνα 2012.
- [6] MIT OpenCourseWare Notes, Student Notes, 4th Transport Phenomena Lecture 22: “Transport in Bulk Electrolytes”, 2011.
(https://ocw.mit.edu/courses/chemical-engineering/10-626-electrochemical-energy-systems-spring-2014/lecture-notes/MIT10_626S14_S11lec22.pdf)
- [7] Χρυσοβέργης Ι., Μπακόπουλος Α., “Εισαγωγή στην Αριθμητική Ανάλυση”, Εκδόσεις Συμείων, 1996.
- [8] Ρασσιάς Θ.Μ., Μαθηματική Ανάλυση ΙΙ, Τεύχος Β’, “Ολοκληρωτικός Λογισμός Συναρτήσεων Πολλών Μεταβλητών”, Εκδόσεις Συμείων, 2009.
- [9] M.A. Javed, W.C. Neil, P.R. Stoddart, and S.A. Wade, “Influence of carbon steel grade on the initial attachment of bacteria and microbiologically influenced corrosion”, Biofouling Journal Vol. 32, Issue 1, Pages 109-122, 2016.

CHAPTER 6 – CONCLUSIONS

The aim of the present Diploma Thesis is the simulation of the electrochemical behavior for naval steel microstructure with the exploitation of experimental polarization data. For the model development the simulation of the microstructure was also required as an input parameter.

In particular the electrochemical behavior of AH36 steel, which consists of a-phase ferrite and pearlitic micro – constituents, was simulated in NaCl 3.5% environment, concerning the polarization curves obtained by the potentiostatic method. The electrochemical behavior of this alloy was simulated, taking into account the electrochemical behavior of its different microstructure components: ferrite a-phase and pearlite micro-constituents. For this reason, electrochemical experiments (potentiostatic polarization) were conducted on the following specimens:

- AH36 ferritic-pearlitic steel
- Ferrite specimen
- Pearlite specimen

Where ferrite and pearlite are the constituting metallographic phases of AH36.

The Tafel curves obtained from the electrochemical experiments performed showed that, Ferrite presents lower values for E_{corr} than Pearlite, indicating that Ferrite exhibits higher tendency for corrosion. Concerning the i_{corr} values, the corrosion rate for Pearlite is higher, presenting faster dissolution rates. Moreover, regarding the cathodic branch of both curves, it is clear that the reduction of oxygen is prevailing in the cathodic reactions (diffusion controlled). The corrosion behavior of AH36, concerning both E_{corr} and i_{corr} , lies in between the corrosion behavior of its consisting phases.

The study of the obtained Tafel curves lead to the following conclusions:

- The electrochemical behavior of ferritic-pearlitic AH36 steel seems to depend on its constituting metallurgical phases (a-phase ferrite and pearlitic micro-constituents). Additionally, this behavior could be simulated according to the amount of each phase within the alloy's microstructure.
- The difference between the electrochemical kinetics of Ferrite and Pearlite within the same solution, implies that it would be possible for a galvanic couple to be formed at the microstructural level. More specifically, in ferrite – pearlite alloys exposed to corrosion, the ferrite grains could act as anodes providing electrons towards the pearlitic regions (acting as

cathodes). Such phenomena could eventually lead to more selective corrosion patterns (e.g. pitting corrosion, selective attack etc.)

Consequently, in order to simulate the microstructure of the ferritic-pearlitic steel, Voronoi tessellation approach resulted to a very sufficient simulation, leading to the following conclusions:

- Voronoi tessellation approach can adequately simulate the micro-structure of polycrystalline material structure, since it is composed of an enormous number of grains and its properties and performance are determined not only by the characteristics of individual grains, but also by the connectivity and interaction between them. The only prerequisite is that it contains fine grain distribution, not affected by external heat treatments or manufacturing processes e.g. rolling.
- The similarity between the modelled and the actual specimen's microstructure can be also explained by the mathematical principles of the Voronoi tessellation. Such discretization is based on the division of space into regions that include all the area closer to the generation point compared to all other generation points. By applying this partitioning into a metal's grain structure, one can correlate the site of a Voronoi cell to the solidification nucleus of the grain represented by the cell. This physically implies that the grain is supposedly solidificated around its generating nucleus, enclosing the material closer to this nucleus than to any other solidification nucleus.
- Any geometries that the model creates can be exported to other finite element packages for the analysis of certain physics governing the microscale geometry of a polycrystalline material.
- The ferrite and pearlite amounts on the model's application microstructure deviates by 0.36% from the actual microstructure. This amount of deviation is considered acceptable and therefore negligible for most cases (e.g. stress-strain analysis) on which this model could be applied.

The experimental Tafel curves, for the separate a-phase ferritic specimen and the pearlitic specimen, along with the simulation of the microstructure of the AH36 ferritic – pearlitic steel were imported in Comsol Multiphysics in order to obtain the polarization curve of AH36 ferritic – pearlitic steel.

The modeled and the experimental polarization curves for AH36 ferritic-pearlitic steel appear to be similar. The same conclusion is deduced regarding the E_{corr} , i_{corr} electrochemical parameters for the modeled and the experimental curves.

Moreover, the metal dissolution predicted from the model, shows that the electrolyte has penetrated against the metal. This denotes that the metallic regions have dissolved thus permitting the solution to invade. Moreover, near ferritic regions the electrolyte's current density presents higher values compared to the regions near pearlite. Hence, it is clarified how this implies a higher anodic current on ferrite than on pearlite, leading to a respective behavior regarding the dissolution rates. The metal dissolution prediction proves that the ferritic regions are highly dissolved, whilst the pearlitic show very little dissolution.

The agreement between the model's polarization curves and the experimental ones, along with the agreement in the obtained parameters E_{corr} , i_{corr} prove that the assumption of electrochemical behavior of AH36 ferritic-pearlitic steel being defined by the electrochemical behavior of its constituting microstructures is fairly stated, as long as it is supported by a concrete simulation of the micro-structure.

ANNEX 1**CODE-1**

```

close all
clear all
digits(10)
[ferritis,perlitis,sites_all]=sites ;
x_vor=sites_all(:,1);
y_vor=sites_all(:,2);
z_vor=sites_all(:,3);
[XY,V,C]=Voronoi_sinartisi(x_vor, y_vor);
for i = 1:size(C,1)
    patch(V(C{i},1),V(C{i},2),i);
    k=C{i};
    arithmoskorufwn(i)=size(k,1);
end
max_arithmoskorufwn=max(arithmoskorufwn);
for ii = 1:1:length(C)
    for jj=1:1:max_arithmoskorufwn
        k=C{ii};
        if jj<=size(k,1)
            korufes(ii,jj)=k(jj);
        else
            korufes(ii,jj)=-1;
        end
    end
end
test1=0;
for ii =1:1:length(C) ;
    test1=0;
    if (korufes(ii,1)~= -1)
        test1=1;
        for jj=1:1:max_arithmoskorufwn
            if (korufes(ii,jj)~= -1)
                x_pol(ii,jj)=V(korufes(ii,jj),1);
                y_pol(ii,jj)=V(korufes(ii,jj),2);
            else
                x_pol(ii,jj)=NaN;
                y_pol(ii,jj)=NaN;
            end
        end
    end
end
end
kokkoi_x=x_pol;
kokkoi_y=y_pol;
for i=1:1:size(XY,1);
    for jj = 1:1:size(sites_all,1);
        if XY(i,1)==sites_all(jj,1);
            if XY(i,2)==sites_all(jj,2);
                XY(i,3)=sites_all(jj,3);
            end
        end
    end
end

```

```

    end
end
figure
axis on
axis equal
grid on
ylim([0.55 0.7]);
xlim([0.4 0.6]);
kokkoi_sites=XY;
for i = 1:1:size(sites_all,1)
    if kokkoi_sites(i,3)==0;
[a,b]=korifes_kokkou(kokkoi_x(i,:),kokkoi_y(i,:));
    patch( a(:),b(:), 'w')
        hold on
    else
        [a,b]=korifes_kokkou(kokkoi_x(i,:),kokkoi_y(i,:));
        patch( a(:),b(:), 'k')
            hold on
    end
end
end

min_shmeio_x = min(min( kokkoi_x));
min_shmeio_y = min(min( kokkoi_y));
max_shmeio_x = max(max( kokkoi_x));
max_shmeio_y = max(max( kokkoi_y));
diasthma_x= max_shmeio_x- min_shmeio_x;
diasthma_y = max_shmeio_y- min_shmeio_y;
k=1;
for jj= min_shmeio_x : diasthma_x / 40: max_shmeio_x;
    for kk=min_shmeio_y : diasthma_y / 40 : max_shmeio_y;
        shmeia(k,1)=jj;
        shmeia(k,2)=kk;
        for ii =1:1:size(kokkoi_sites,1);
            type=kokkoi_sites(ii,3);

            in=inpolygon(jj, kk, kokkoi_x(ii,:),kokkoi_y(ii,:));
            if in ==1
                shmeia(k,3)=ii;
                shmeia(k,4)=type;
                k=k+1;
            end
        end
    end
end

end
end

figure
axis on
axis equal
grid on
ylim([0.55 0.7]);
xlim([0.4 0.6]);
hold on
for k=1:1:size(shmeia,1)
    if shmeia(k,4)==0
        plot(shmeia(k,1), shmeia(k,2), 'b*')
    end
end

```

```

        hold on
    else
        plot(shmeia(k,1),shmeia(k,2),'*','Color',[1 0.4 0.4])
        hold on
    end
end
end

```

CODE-2

```

function [kor_x,kor_y]= korifes_kokkou(a1,b1)
k=1;
for jj=1:1:size(a1,2)
deiktis= isnan(a1(jj))
if deiktis==0
    kor_x(k)=a1(jj);
    kor_y(k)=b1(jj);
    k=k+1;
end
end
end

```

CODE-3

```

function [XY,V,C]=Voronoi_sinartisi(varargin)
warning('off','map:polygon:noExternalContours');
if nargin==0
    val=600;
    x=rand(val,1);
    y=rand(val,1);
    XY=unique([x,y],'rows');
    x=XY(:,1);
    y=XY(:,2);
    ButtonName = questdlg('Choose external boundary example:','','Irregular
pentagon', 'Triangle', 'Irregular pentagon');
    switch ButtonName,
        case 'Irregular pentagon',
            bs_ext=[min(x)-std(x)/2 min(x)-std(x)/2 0.65 max(x)+std(x)/2
max(x)+std(x)/2 min(x)-std(x)/2;min(y)-std(y)/2 max(y)+std(y)/2
max(y)+std(y)/2 .65 min(y)-std(y)/2 min(y)-std(y)/2]';
            case 'Triangle',
                bs_ext=[-.8 .5 1.80 -.8;-.05 1.7 -.05 -.05]';
    end
    bs_int=cell(3,1);
    rat=1.5;
    bs_int{1}=[min(x)+(std(x)*rat) min(x)+(std(x)*rat) max(x)-std(x) max(x)-
std(x) min(x)+(std(x)*rat);min(y)+std(y) max(y)-std(y) max(y)-std(y)
min(y)+std(y) min(y)+std(y)]';
    t = linspace(0,2*pi)';
    xc=.25;
    yc=.7;
    rad=.10;
    bs_int{2}=[(cos(t)*rad)+xc (sin(t)*rad)+yc];
    xc=.4;

```

```

yc=.3;
rad=.16;
bs_int{3}=[(cos(t)*rad)+xc (sin(t)*rad)+yc];
fig='on';
else
x=varargin{1}(:);
y=varargin{2}(:);
XY=unique([x,y], 'rows');
x=XY(:,1);
y=XY(:,2);
for ii=3:2:nargin
    if strcmp(varargin{ii}, 'bs_ext')
        bs_ext=varargin{ii+1};
    elseif strcmp(varargin{ii}, 'bs_int')
        bs_int=varargin{ii+1};
    elseif strcmp(varargin{ii}, 'figure')
        fig=varargin{ii+1};
    end
end
if exist('fig', 'var')==0
    fig='on';
end
end
x=x(:);
y=y(:);
rx=[min(x) max(x)];
ry=[min(y) max(y)];
bnd=[rx ry];
crs=double([bnd(1) bnd(4);bnd(2) bnd(4);bnd(2) bnd(3);bnd(1) bnd(3);bnd(1)
bnd(4)]);
if exist('bs_ext', 'var')
    crs=bs_ext;
end
if ~any(size(x)==1) || ~any(size(y)==1) || numel(x)==1 || numel(y)==1
    disp('Input vectors should be single rows or columns')
    return
end
dt=delaunayTriangulation(x(:),y(:));
[V,C]=voronoiDiagram(dt);
[vx,vy]=voronoi(x,y);
vxyl=[vx(:) vy(:)];
xix=ones(size(vx));
vals=unique(vxyl(:));
for ik=1:length(vals)
    ix=find(V(:)==vals(ik));
    if ~isempty(ix)
        V(ix)=vals(ik);
    end
end
lV0=length(V);
for ii=1:length(vxyl)
    fix=find(V(:,1)==vxyl(ii,1));
    if ~isempty(fix)
        if any(V(fix,2)==vxyl(ii,2))
            xix(ii)=0;
        end
    end
end
end

```

```

end
mix=find(xix==1)./2;
lmix=length(mix);
mvx=vx(2,mix);
mvy=vy(2,mix); %missing vy
mv=[mvx',mvy'];
cpv=vx(1,mix);
cpy=vy(1,mix);
ctr=0;
mv2=[];
cpVixt=cell(lmix,1);
for ii=1:lmix
    if any(V(:,1)==cpv(ii) & V(:,2)==cpy(ii))
        cpVixt{ii}=find(V(:,1)==cpv(ii) & V(:,2)==cpy(ii));
        lval=length(cpVixt{ii});
        if lval==1
            ctr=ctr+1;
            mv2(ctr,:)=mv(ii,:);
        elseif lval>1
            ctr=ctr+1;
            mv2(ctr:ctr+lval-1,:)=ones(lval,1).*mv(ii,1)
            ones(lval,1).*mv(ii,2)];
            ctr=ctr+lval-1;
        end
    end
end
cpVixt=cell2mat(cpVixt);
V=[V;mv2];
for ij=1:length(C)
    if any(C{ij}==1)
        ixa=find(cpVixt==C{ij}(2));
        ixb=find(cpVixt==C{ij}(end));
        if length(C{ij})<3
            C{ij}(1)=LV0+ixa(1);
            C{ij}=[C{ij},LV0+ixa(2)];
        else
            if length(ixa)==1 && length(ixb)==1
                C{ij}(1)=LV0+ixa;
                C{ij}=[C{ij},LV0+ixb];
            elseif length(ixa)==2 && length(ixb)==1
                C{ij}=[C{ij},LV0+ixb];
                [~,minix]=min(sqrt((V(C{ij}(end),1)-
V(LV0+ixa,1)).^2+(V(C{ij}(end),2)-V(LV0+ixa,2)).^2)));
                C{ij}(1)=LV0+ixa(minix);
            elseif length(ixa)==1 && length(ixb)==2
                C{ij}(1)=LV0+ixa;
                [~,minix]=min(sqrt((V(C{ij}(1),1)-
V(LV0+ixb,1)).^2+(V(C{ij}(1),2)-V(LV0+ixb,2)).^2)));
                C{ij}=[C{ij},LV0+ixb(minix)];
            elseif length(ixa)==2 && length(ixb)==2
                dist1=sqrt((x(ij)-V(LV0+ixa,1)).^2+(y(ij)-V(LV0+ixa,2)).^2);
                dist2=sqrt((x(ij)-V(LV0+ixb,1)).^2+(y(ij)-V(LV0+ixb,2)).^2);
                if diff(dist1)==0 && diff(dist2)==0
                    minix1=1;
                    minix2=2;
                else
                    [~,minix1]=min(dist1);

```

```

                [~,minix2]=min(dist2);
            end
            C{ij}(1)=lV0+ixa(minix1);
            C{ij}=[C{ij},lV0+ixb(minix2)];
        end
    end
end
C1=C;
allVixinp=inpolygon(V(:,1),V(:,2),crs(:,1),crs(:,2));
isemp=false(length(C),1);
for ij=1:length(C)
    if sum(allVixinp(C{ij}))~=length(C{ij})
        [xb, yb] =
polybool('intersection', crs(:,1), crs(:,2), V(C1{ij},1), V(C1{ij},2));
        ix=nan(1,length(xb));
        for il=1:length(xb)
            if any(V(:,1)==xb(il)) && any(V(:,2)==yb(il))
                ix1=find(V(:,1)==xb(il));
                ix2=find(V(:,2)==yb(il));
                for ib=1:length(ix1)
                    if any(ix1(ib)==ix2)
                        ix(il)=ix1(ib);
                    end
                end
            end
            if isnan(ix(il))==1
                lv=length(V);
                V(lv+1,1)=xb(il);
                V(lv+1,2)=yb(il);
                allVixinp(lv+1)=1;
                ix(il)=lv+1;
            end
        else
            lv=length(V);
            V(lv+1,1)=xb(il);
            V(lv+1,2)=yb(il);
            allVixinp(lv+1)=1;
            ix(il)=lv+1;
        end
    end
    C{ij}=ix;
end
if isempty(C{ij})
    isemp(ij)=true;
end
end
if any(isemp)
    C(isemp)=[];
    XY(isemp,:)=[];
end
if exist('bs_int','var')
    isemp=false(length(C),length(bs_int));
    for ii=1:length(bs_int)
        V2=nan(length(V)*10,2);
        C2=cell(length(C),1);
        ctr=1;
        for ij=1:length(C)

```



```

[pbx, pby]=polybool('subtraction',V(C{ij},1),V(C{ij},2),bs_int{ii}(:,1),bs_int
{ii}(:,2));
    if ~isempty(pbx)
        C2{ij}=(ctr:ctr+length(pbx)-1)';
        C2{ij}=[C2{ij} ones(size(C2{ij})) *ij];
        V2(ctr:ctr+length(pbx)-1,:)= [pbx pby];
        ctr=ctr+length(pbx);
    end
end
V=V2(1:ctr-1,:);
C=C2;
for ij=1:length(C)
    if isempty(C{ij})
        isemp(ij,ii)=true;
    else
        C{ij}=(C{ij}(:,1))';
    end
end
end
if any(any(isemp'))
    C(any(isemp'))=[];
    XY(any(isemp'),:)=[];
end
end
epsx=eps(max(abs(V(isinf(V))==0)));
for ih=1:length(C)
    VC=V(C{ih},:);
    TMAT=true(size(VC,1));
    for ii=1:size(VC,1)
        for ij=1:size(VC,1)
            TMAT(ii,ij)=all(abs(VC(ii,:)-VC(ij,:))<=epsx);
        end
    end
    TMAT=TMAT-eye(size(TMAT));
    if any(TMAT(:)==1)
        if all(abs(V(C{ih})(1,:),:)-V(C{ih})(end,:),:)<=epsx)
            C{ih}(end)=[];
        end
        ctr=0;
        while ctr<length(C{ih})-1
            ctr=ctr+1;
            if all(abs(V(C{ih})(ctr,:),:)-V(C{ih})(ctr+1,:),:)<=epsx)
                C{ih}(ctr+1)=[];
            end
        end
    end
    C{ih}=C{ih}';
end
TMAT=cell(length(V)-1,1);
Vt=V;
idx1=(1:length(V))';
idx2=(1:length(V))';
for ii=1:length(V)-1
    Vt=[Vt(2:end,:);Vt(1,:)];
    idx2=[idx2(2:end);idx2(1)];
    TMATt=find(all(abs(V-Vt)<=epsx,2));

```

```

    TMat{ii}=[idx1(TMATt) idx2(TMATt)];
end
TMATf=unique(sort(cell2mat(TMAT),2),'rows');
if ~isempty(TMATf)
    for ii=1:size(TMATf,1)
        for ij=1:length(C)
            C{ij}(C{ij}==TMATf(ii,2))=TMATf(ii,1);
        end
    end
end
index_rem=true(size(V,1),1);
Ctot=unique(cell2mat(C));
index_rem(Ctot)=false;
index_rem=find(index_rem);
while ~isempty(index_rem)
    for ij=1:length(C)
        ixf=find(C{ij}>index_rem(1));
        if ~isempty(ixf)
            C{ij}(ixf)=C{ij}(ixf)-1;
        end
    end
    V(index_rem(1),:)=[];
    index_rem=true(size(V,1),1);
    Ctot=unique(cell2mat(C));
    index_rem(Ctot)=false;
    index_rem=find(index_rem);
end
Csplitted=cell(length(C),1);
XYsplitted=cell(length(C),1);
splitlog=false(length(C),1);
for ij=1:length(C)
    [xClosed, yClosed] = closePolygonParts(V(C{ij},1),V(C{ij},2));
    if any(isnan(xClosed))
        splitlog(ij)=true;
        ix=find(~isnan(xClosed));
        diffix=diff(ix)>1;
        NUMcell=sum(isnan(xClosed))+1;
        Csplitted{ij}=cell(NUMcell,1);
        XYsplitted{ij}=nan(NUMcell,2);
        C_temp=C{ij};
        ix_begin=1;
        for ik=1:NUMcell
            cs_diffix=cumsum(diffix);
            if ik>1
                ix_begin=2;
            end
            ix_end=find(cs_diffix>0,1,'first');
            if isempty(ix_end)
                ix_end=length(xClosed);
            end
            Csplitted{ij}{ik}=C_temp(ix_begin:ix_end);
        end
    end
    inpol=inpolygon(XY(ij,1),XY(ij,2),xClosed(ix_begin:ix_end),yClosed(ix_begin:ix_end));
    if inpol==0
        XYsplitted{ij}(ik,:)=[mean(xClosed(ix_begin:ix_end))
            mean(yClosed(ix_begin:ix_end))];
    else

```

```

        XYsplit{ij}(ik,:)=XY(ij,:);
    end
    if ik<NUMcell
        C_temp(ix_begin:ix_end)=[];
        diffix(ix_begin:ix_end)=[];
        xClosed(ix_begin:ix_end)=[];
        yClosed(ix_begin:ix_end)=[];
    end
end
end
end
if any(splitlog)
    ix_splitlog=find(splitlog);
    ix_splitlog0=ix_splitlog;
    for ij=1:length(ix_splitlog)
        if ix_splitlog(ij)==1
            C=[Csplit{ix_splitlog(ij)};C(2:end)];
            XY=[XYsplit{ix_splitlog(ij)};XY(2:end,:)];
        elseif ix_splitlog(ij)==length(C)
            C=[C(1:end-1);Csplit{ix_splitlog(ij)}];
            XY=[XY(1:end-1,:);XYsplit{ix_splitlog(ij)}];
        else
            C=[C(1:ix_splitlog(ij)-
1);Csplit{ix_splitlog0(ij)};C(ix_splitlog(ij)+1:end)];
            XY=[XY(1:ix_splitlog(ij)-
1,:);XYsplit{ix_splitlog0(ij)};XY(ix_splitlog(ij)+1:end,:)];
            if ij<length(ix_splitlog)
                ix_splitlog(ij+1:end)=ix_splitlog(ij+1:end)+(length(Csplit{ix_splitlog0(ij)})
-1);
            end
        end
    end
end
end
for ih=1:length(C)
    if ispolycw(V(C{ih},1),V(C{ih},2))
        C{ih}=flipud(C{ih});
    end
end
C2=C;
for ih=1:length(C2)
    if C2{ih}(1)~=C2{ih}(end)
        C2{ih}=[C2{ih};C2{ih}(1)];
    end
end
if exist('fig','var')
    if strcmp(fig,'on')
        figure
        set(gcf,'position',get(0,'screensize'),'color','w')
        set(gca,'box','on')
        hold on
        plot(x,y,'.k')
        if any(splitlog)
            for ij=1:length(ix_splitlog0)
                plot(XYsplit{ix_splitlog0(ij)}(:,1),XYsplit{ix_splitlog0(ij)}(:,2),'*r')
            end
        end
    end
end

```

```

plot(XYsplit{ix_splitlog0(ij)}(:,1),XYsplit{ix_splitlog0(ij)}(:,2),'or','mark
ersize',8)
    end
end
voronoi(x,y)
for id=1:length(C2)
    plot(V(C2{id},1),V(C2{id},2),'-r')
end
grid on
axis tight
axis square
if nargin==0
    axis equal
end
ax=axis;
dx=(ax(2)-ax(1))/10;
dy=(ax(4)-ax(3))/10;
axis([ax(1)-dx ax(2)+dx ax(3)-dy ax(4)+dy])
title({'Original Voronoi Decomposition ({\color{blue}blue}');'New
limited Voronoi Decomposition
({\color{red}red}'),'fontsize',16,'fontweight','bold')
    if exist('bs_int','var')
        for ii=1:length(bs_int)
            text(mean(unique(bs_int{ii}(:,1))),mean(unique(bs_int{ii}(:,2))),num2str(ii),
'fontsize',30,'fontweight','bold','horizontalalignment','center')
        end
    end
end
end
end

```

CODE-4

```

function [sites_perliti,sites_ferriti,sites_all]= sites
[sites_perliti]=textread('perlitis1.txt')
[sites_ferriti]=textread('ferritis1.txt')
for i = 1:1:size(sites_perliti,1)
    sites_perliti(i,3)=1;
end
sites_all=[sites_perliti; sites_ferriti]
end

```

CODE-5

```

function [sites_perliti,sites_ferriti,sites_all]= sites
[sites_perliti]=textread('perlitis2.txt')
[sites_ferriti]=textread('ferritis2.txt')
for i = 1:1:size(sites_perliti,1)
    sites_perliti(i,3)=1;
end
sites_all=[sites_perliti; sites_ferriti]
end

```

ANNEX 2

CODE-1

```

close all
clear all
E_I_kath(:,1)=xlsread('kk_kampiles_E_i','final','O6:O506');
E_I_kath(:,2)=xlsread('kk_kampiles_E_i','final','P6:P506');
E_I_an(:,1)=xlsread('kk_kampiles_E_i','final','O706:O1006');
E_I_an(:,2)=xlsread('kk_kampiles_E_i','final','P706:P1006');
E_I_ola(:,1)=xlsread('kk_kampiles_E_i','final','O6:O1006');
E_I_ola(:,2)=xlsread('kk_kampiles_E_i','final','P6:P1006');
n=0;
for i=50:20:size(E_I_an,1)-20;
    n=1+n;
    m=1;
    for k=1:1:size(E_I_an,1)-i;
        [a,b,Var]=eythia_an(k,i,E_I_an);
        sfalma2_an(n,m)=Var;
        klisi_an(n,m)=a;
        y0_an(n,m)=b;
        m=m+1;
    end
    [dev_an(n,:),deiktis_an(n,.)]=sort(sfalma2_an(n,:), 'ascend');
    l=1;
    stamata=0;
    while stamata==0;
        if klisi_an(n,deiktis_an(n,l))==0;
            l=l+1;
        else
            telika_an(n,1)=deiktis_an(n,l);
            telika_an(n,2)=deiktis_an(n,l+1);
            telika_an(n,3)=deiktis_an(n,l+2);
            telika_an(n,4)=deiktis_an(n,l+3);
            stamata=1;
        end
    end
end
for ii=1:1:size(telika_an,1)
    for jj=1:1:size(telika_an,2)
        finals_an(jj+(ii-
1)*size(telika_an,2),1)=sfalma2_an(ii,telika_an(ii,jj));
        finals_an(jj+(ii-
1)*size(telika_an,2),2)=klisi_an(ii,telika_an(ii,jj));
        finals_an(jj+(ii-1)*size(telika_an,2),3)=y0_an(ii,telika_an(ii,jj));
        finals_an(jj+(ii-1)*size(telika_an,2),4)=(ii-1)*20+50; %o arithmos
    end
end
simion tou evrous
end
end
[finals_asc_an,deiktis_asc]=sort(finals_an(:,1), 'ascend');
finals_asc_an(:,2)=finals_an(deiktis_asc,2);
finals_asc_an(:,3)=finals_an(deiktis_asc,3);
finals_asc_an(:,4)=finals_an(deiktis_asc,4);

```

```

n=0;
vima_kath=10;
for i=10:vima_kath:size(E_I_kath,1);
    n=1+n;
    m=1;
    for k=1:1:size(E_I_kath,1)-i;
        [a,b,Var]=eythia_kath(k,i,E_I_kath);
        sfalma2_kath(n,m)=Var;
        klisi_kath(n,m)=a;
        y0_kath(n,m)=b;
        m=m+1;
    end
    [dev_kath(n,:),deiktis_kath(n,.)]=sort(sfalma2_kath(n,),'ascend');
    l=1;
    stamata=0;
    while stamata==0;
        if klisi_kath(n,deiktis_kath(n,l))==0;
            l=l+1;
        else
            telika_kath(n,l)=deiktis_kath(n,l);
            stamata=1;
        end
    end
end
for ii=1:1:size(telika_kath,1)
    for jj=1:1:size(telika_kath,2)
        finals_kath(jj+(ii-
1)*size(telika_kath,2),1)=sfalma2_kath(ii,telika_kath(ii,jj));

        finals_kath(jj+(ii-
1)*size(telika_kath,2),2)=klisi_kath(ii,telika_kath(ii,jj));

        finals_kath(jj+(ii-
1)*size(telika_kath,2),3)=y0_kath(ii,telika_kath(ii,jj));
        finals_kath(jj+(ii-1)*size(telika_kath,2),4)=(ii-1)*vima_kath+10; %o
    end
end
[finals_asc_kath,deiktis_asc_kath]=sort(finals_kath(:,1),'ascend');
finals_asc_kath(:,2)=finals_kath(deiktis_asc_kath,2);
finals_asc_kath(:,3)=finals_kath(deiktis_asc_kath,3);
finals_asc_kath(:,4)=finals_kath(deiktis_asc_kath,4);
for ii=1:1:1
%i0_kath(ii)=(Eeq_fer- finals_asc_kath(ii,3))/(finals_asc_kath(ii,2));
%i0_an(ii)=(Eeq_fer- finals_asc_an(ii,3))/(finals_asc_an(ii,2));
i_corr_el(ii)=(finals_asc_an(ii,3)-
finals_asc_kath(ii,3))/(finals_asc_kath(ii,2)-finals_asc_an(ii,2));
E_corr_el(ii)=finals_asc_an(ii,3)+finals_asc_an(ii,2)*i_corr_el(ii);1
figure
axis on
axis equal
ylim([-1 0]);
xlim([-2 0]);
plot(E_I_ola(:,1),E_I_ola(:,2),'linewidth',2,'Color',[1 0.4 0.6]);
plot(E_I_an(:,1),E_I_an(:,2),'linewidth',2,'Color',[1 0.4 0.6]);
plot(E_I_kath(:,1),E_I_kath(:,2),'linewidth',2,'Color',[1 0 0]);
hold on

```

```

f1=refline( finals_asc_kath(ii,2), finals_asc_kath(ii,3));
set(f1(1), 'linewidth',2);
f1.Color = '[0.5 0.2 0.2]'
hold on
f2=refline( finals_asc_an(ii,2), finals_asc_an(ii,3) );
f2.Color='[0.9 0.2 0.2]'
set(f2(1), 'linewidth',2);
ylim([-1 0]);
xlim([-4 4]);
plot(i_corr_el(ii),E_corr_el, 'g*')
% Ecorr(ii)= finals_asc_per_an(ii,2)*i0(ii)+ finals_asc_per_an(ii,3);
str=sprintf('ah36 a=%d b=%d diaspora= %d evros=%d kai ah36 a=%d b=%d
diaspora = %d evros=%d kai i_corr_ah36_el=%d kai
E_corr_ah36_el=%d',finals_asc_an(ii,2),finals_asc_an(ii,3),finals_asc_an(ii,1
),finals_asc_an(ii,4),finals_asc_kath(ii,2),finals_asc_kath(ii,3),finals_asc_
kath(ii,1),finals_asc_kath(ii,4),i_corr_el(ii),E_corr_el(ii));
title(str)
legend('experimental data','anodic tafel','cathodic tafel')
xlabel('log(abs(i[A/m2]))')
ylabel('E vs SCE[Volt]')
grid on
grid minor

end
figure
axis on
plot(100*10.^E_I_ola(:,1),E_I_ola(:,2), 'linewidth',4, 'Color',[1 0.4 0.6]);
hold on
plot(100*10.^[-4:4] , log10(10.^[-4:4])* finals_asc_kath(ii,2)+
finals_asc_kath(ii,3) , 'linewidth',2, 'Color',[0.9 0.2 0.2])
plot(100*10.^[-4:4] , log10(10.^[-4:4])* finals_asc_an(ii,2)+
finals_asc_an(ii,3), 'linewidth',2, 'Color',[0.5 0.2 0.2])
plot(100*10^i_corr_el(ii),E_corr_el(ii), 'g*')
ylim([-1 -0.4]);
xlim([10^-4 10^4]);
% Ecorr(ii)= finals_asc_per_an(ii,2)*i0(ii)+ finals_asc_per_an(ii,3);
legend('experimental data','anodic tafel','cathodic tafel',' ( i_{corr} ,
E_{corr} )')
xlabel(' ( i [ ?A/cm^{2} ] )')
ylabel('E vs SCE [ Volt ]')
grid on
grid minor
figure
plot(E_I_an(:,1),E_I_an(:,2), 'linewidth',2, 'Color',[1 0.4 0.6]);
hold on
plot(E_I_kath(:,1),E_I_kath(:,2), 'linewidth',2, 'Color',[1 0 0]);
100*10^i_corr_el(ii)
E_corr_el(ii)

```

CODE-2

```
function [a,b,Var]= eythia(k,i,data1)
n=1;
for j=k:1:i-1+k
    x_Data(n,1)=data1(j,1);
    y_Data(n,1)=data1(j,2);
    n=n+1;
end
p=polyfit(x_Data(:,1),y_Data(:,1),1);
a=p(1,1);
b=p(1,2);
s1=y_Data(:,1)-a*x_Data(:,1)-b;
Var1=sum(s1.^2)/size(x_Data,1);
s2=data1(:,2)-a*data1(:,1)-b;
Var2=sum(s2.^2)/size(data1,1);
Var=0.5*Var1+0.5*Var2;
end
```

CODE-3

```
function [a,b,Var]= eythia(k,i,data)
n=1;
for j=k:1:i-1+k
    x_Data(n,1)=data(j,1);
    y_Data(n,1)=data(j,2);
    n=n+1;
end
p=polyfit(x_Data(:,1),y_Data(:,1),1);
a=p(1,1);
b=p(1,2);
s1=y_Data(:,1)-a*x_Data(:,1)-b;
Var1=sum(s1.^2)/size(x_Data,1);
s2=data(:,2)-a*data(:,1)-b;
Var2=sum(s2.^2)/size(data,1);
Var=0.5*Var1+0.5*Var2;
end
```